

DISS. ETH No. 17719

THE DRIFT CHAMBERS OF THE MEG EXPERIMENT AND  
MEASUREMENT OF THE  $\rho$ -PARAMETER IN THE MICHEL  
SPECTRUM OF THE MUON DECAY.

A dissertation submitted to  
ETH ZURICH

for the degree of  
DOCTOR OF SCIENCES

presented by  
MATTHIAS SCHNEEBELI  
Dipl. Phys. ETH  
born August 9<sup>th</sup>, 1976  
citizen of Switzerland

accepted on the recommendation of  
Prof. Dr. Ralph Eichler, examiner  
Prof. Dr. Felicitas Pauss, co-examiner  
2008



# Abstract

The Standard Model (SM) of electro-weak interactions has been successfully used to describe the fundamental processes in nature, since its introduction, more than forty years ago. Although it has some theoretical deficiencies, until now, it never failed to describe an experimentally measured process, except neutrino oscillation. However, neutrino oscillation can in principle be included into the model. In the recent years several new theories were developed, which try to paint a more fundamental picture of the universe.

Recently, experiments have proven that neutrinos are not massless and therefore can oscillate from one flavor to another flavor: The so called lepton flavor violation in the neutrino sector. An analogue process in the charged lepton sector has been proposed long ago. Therefore, the search for flavor violation in the charged lepton sector has a long tradition, but it has not yet been found.

The MEG collaboration, composed of physicists from Italy, Japan, Switzerland, Russia and the US, has recently started to operate a new detector for measuring the lepton flavor violating decay  $\mu^+ \rightarrow e^+ \gamma$ . The goal of the MEG experiment is to lower the current sensitivity limit by two orders of magnitude to  $1 \times 10^{-13}$ . For this purpose the positron track from a  $\mu^+ \rightarrow e^+ \gamma$  decay will be measured with a novel set of drift chambers, designed to have a very small material budget in the sensitive area of the detector to reduce particle scattering.

This thesis deals with various aspects of the MEG experiment, the data acquisition, the software framework and the drift chamber analysis.

To read out all of the channels of the detector a newly developed signal sampling chip was used. The testing and the calibration of this chip, being a key part of the experiment, are presented in this work.

A software framework for the data analysis of the MEG detector was developed during this thesis. The framework was designed to be as universally applicable as possible. It is used as the basis for all analysis code of the MEG experiment and also in two experiments in the Los Alamos National Laboratories.

The algorithms written to analyze the data recorded with the drift chambers is presented. The energy resolution of reconstructed Monte Carlo signal events was determined to be 0.27 MeV ( $\sigma$ ). Further, the calibrations applied to the data taken in the 2007 run are discussed. The hit position can be reconstructed to a precision of 230  $\mu\text{m}$  in radial direction and 900  $\mu\text{m}$  in z direction. The current energy resolution of the chambers was measured to be  $0.44 \pm 0.05$  MeV. In addition the Michel  $\rho$  parameter was measured. The estimation is largely dominated by systematical errors and turned out to be  $0.73 \pm 0.12$ .



# Zusammenfassung

Vor über 40 Jahren wurde das Standard Models (SM) der elektro-schwachen Wechselwirkung eingeführt. Es beschreibt die bekannten fundamentalen Prozesse der Natur erfolgreich. Trotz seiner theoretischen Unzulänglichkeiten konnten bisher alle experimentell gemessenen Prozesse mit dem SM beschrieben werden ausser Neutrino Oszillation. Diese kann jedoch in das SM eingebaut werden. In den letzten Jahren entstanden eine Vielzahl neuer Theorien, welche ein noch fundamentaleres Bild des Universums zu geben versuchen.

Die neuesten Experimente haben gezeigt, dass Neutrinos eine nicht verschwindende Masse haben und deshalb ihren Flavorzustand wechseln können. Dieser Prozess wird Lepton Flavor Violation im neutralen Lepton Sektor genannt. Die Suche nach analogen Prozessen im geladenen Lepton Sektor hat eine lange Tradition, wurde aber noch nicht gefunden.

Die MEG Kollaboration, bestehend aus Physiker aus Italien, Japan, der Schweiz, Russland und den USA, nimmt zurzeit einen neuen Detektor in Betrieb, mit welchem der  $\mu^+ \rightarrow e^+ \gamma$  Zerfall gemessen werden soll. Das Ziel ist die Sensitivität des Detektors auf den Zerfall um zwei Größenordnungen auf  $1 \times 10^{-13}$  zu senken. Für die Messung der Positron Spur des  $\mu^+ \rightarrow e^+ \gamma$  Zerfalls wurde ein spezielles Set von Driftkammern entwickelt, welche möglichst wenig Material in den sensitiven Bereichen des Detektors haben, um so die Streuung der Teilchen zu verringern.

Diese Arbeit beschreibt verschiedene Aspekte des MEG Experiments, die Data-naquisition, das Analyseframework und die Analyse der Driftkammern.

Für die Auslese des Detektors wurde ein neuer Signal Sampling Chip entwickelt. Die Tests und die Kalibrierung, welche für die Inbetriebnahme des Chips erforderlich waren, werden in dieser Arbeit erläutert.

Ein Software Framework für die Datenanalyse des MEG Detektors wurde entwickelt. Das Framework wurde so konstruiert, dass es möglichst universal eingesetzt werden kann. Es bildet die Basis für die gesamte Analysesoftware, welche im Experiment eingesetzt wird. Des Weiteren wird es auch in zwei Experimenten in den Los Alamos

National Laboratories verwendet.

Die Analyse der Drift Kammer, welche im Rahmen dieser Dissertation entwickelt wurde, wird detailliert erklärt. Sie ermöglicht, die Energie der rekonstruierten Monte Carlo Signal Ereignisse auf 0.27 MeV genau zu bestimmen. Des weiteren wird die Kalibration der Daten der 2007 Runperiode besprochen. Die kalibrierten Daten werden verwendet, um nach Positronen aus dem Muon-Zerfall zu suchen. Die Hits der Positronspuren werden mit einer Präzision von  $230\text{ }\mu\text{m}$  in radialer Richtung und  $900\text{ }\mu\text{m}$  in Z-Richtung rekonstruiert. Die Energie des Positrons konnte mit einer Genauigkeit von  $0.44 \pm 0.05\text{ MeV}$  gemessen werden. Zusätzlich wurde der Michel  $\rho$  Parameter bestimmt. Die Messung von  $0.73 \pm 0.12$  wird von systematischen Fehlern dominiert.

# Contents

Abstract	i
Zusammenfassung	iii
Introduction	1
<b>I Theory and Phenomenology</b>	<b>3</b>
<b>1 The Standard Model and beyond</b>	<b>5</b>
1.1 The Standard Model . . . . .	5
1.1.1 Quantum Electrodynamics . . . . .	6
1.1.2 Yang-Mills Theory . . . . .	7
1.1.3 Spontaneous Symmetry Breaking . . . . .	8
1.1.4 The Higgs Mechanism . . . . .	9
1.1.5 Glashow-Salam-Weinberg Theory . . . . .	10
1.2 Neutrino masses . . . . .	13
1.2.1 Seesaw Mechanism . . . . .	13
1.2.2 Neutrino Mixing . . . . .	14
1.3 Beyond the Standard Model . . . . .	16
1.3.1 Grand Unified Theories (GUT) . . . . .	16
1.3.2 Supersymmetry (SUSY) . . . . .	17
1.3.3 SUSY GUT . . . . .	18
<b>2 Search for the <math>\mu^+ \rightarrow e^+ \gamma</math> decay</b>	<b>21</b>
2.1 Phenomenology of the $\mu^+ \rightarrow e^+ \gamma$ decay . . . . .	21
2.2 Experimental status of $\mu^+ \rightarrow e^+ \gamma$ decay search . . . . .	23
2.3 Event and backgrounds signature . . . . .	24
2.4 Background rejection . . . . .	26
2.5 Future of LFV searches . . . . .	27

<b>II</b>	<b>The MEG experiment</b>	<b>29</b>
<b>3</b>	<b>Experiment Setup</b>	<b>31</b>
3.1	Introduction . . . . .	31
3.2	Beam and Target . . . . .	32
3.2.1	MEG specific beam line components . . . . .	32
3.2.2	Target . . . . .	34
3.3	Positron Detector . . . . .	35
3.3.1	Magnet . . . . .	36
3.3.2	Drift Chambers . . . . .	38
3.3.3	Timing Counters . . . . .	40
3.4	Photon Detector . . . . .	41
3.5	Trigger and DAQ . . . . .	42
3.5.1	Trigger . . . . .	42
3.5.2	DAQ . . . . .	43
<b>4</b>	<b>The Domino Ring Sampling Chip</b>	<b>45</b>
4.1	Introduction . . . . .	45
4.2	Temperature Dependence . . . . .	47
4.3	DRS2 Calibrations . . . . .	51
4.3.1	Response Calibration . . . . .	51
4.3.2	Offset Calibration . . . . .	52
4.3.3	Time Calibration . . . . .	53
4.4	Synchronization of chips . . . . .	55
4.5	DRS2 Measurements . . . . .	56
4.5.1	Cluster Points in the voltage response . . . . .	56
4.5.2	Cross Talk . . . . .	56
4.5.3	Ghost Pulses . . . . .	57
4.5.4	Band width . . . . .	58
4.5.5	Time- and Charge Resolution . . . . .	58
<b>5</b>	<b>Analysis Framework</b>	<b>65</b>
5.1	Introduction . . . . .	65
5.2	Generating Analysis Frameworks . . . . .	67
5.2.1	Benefits of a generated framework . . . . .	67
5.3	ROME . . . . .	69
5.3.1	The ROMEBuilder . . . . .	69
5.3.2	Programming inside ROME . . . . .	70
5.3.3	Features . . . . .	70

<b>III</b>	<b>The Drift Chamber Analysis</b>	<b>73</b>
<b>6</b>	<b>The First Engineering Run</b>	<b>75</b>
6.1	Hardware problems . . . . .	75
6.2	Data Analysis . . . . .	76
6.2.1	Noise . . . . .	76
6.2.2	Number of Hits per Wire . . . . .	76
6.3	Conclusion . . . . .	77
<b>7</b>	<b>Event Reconstruction</b>	<b>81</b>
7.1	Hit Reconstruction . . . . .	81
7.1.1	Noise Subtraction on Wire Signals . . . . .	81
7.1.2	Baseline Determination and Peak Finding . . . . .	82
7.1.3	Leading Edge Fit . . . . .	83
7.1.4	Charge Integration . . . . .	83
7.1.5	Z Coordinate Evaluation . . . . .	84
7.2	Track Finding . . . . .	85
7.2.1	Clustering Hits . . . . .	85
7.2.2	Finding a Track Seed . . . . .	85
7.2.3	Calculating the Drift Time of the Hits . . . . .	85
7.2.4	Extrapolating Tracks . . . . .	86
7.2.5	Solve Left-Right Ambiguity . . . . .	87
7.3	Track Fitting . . . . .	87
7.4	MC Resolution and Efficiency . . . . .	88
7.5	Conclusion . . . . .	90
<b>8</b>	<b>Calibrations</b>	<b>93</b>
8.1	Data Set . . . . .	93
8.2	Z Calibration . . . . .	94
8.2.1	Anode Gain Calibration and Anode-Cathode Normalization . . . . .	94
8.2.2	Cathode Gain Calibration . . . . .	96
8.3	Time Calibration . . . . .	97
8.4	Wire Alignment . . . . .	100
8.5	X-T Function Calibration . . . . .	101
8.6	Detector Resolution . . . . .	103
<b>9</b>	<b>Data Analysis</b>	<b>105</b>
9.1	Electron Energy Spectrum in a Muon Decay . . . . .	105
9.2	Data and Monte Carlo Samples . . . . .	107
9.3	Determination of the Energy Resolution . . . . .	108
9.4	Determination of the Michel Parameters . . . . .	110

9.4.1	Results . . . . .	111
9.4.2	Systematical Error . . . . .	112
9.4.3	Comparison with existing measurements . . . . .	113
9.5	Outlook . . . . .	114
<b>10</b>	<b>Conclusions</b>	<b>117</b>
	<b>Appendix</b>	<b>119</b>
<b>A</b>	<b>Calculation of the Z Projection during the Track Finding</b>	<b>119</b>
	<b>List of Figures</b>	<b>121</b>
	<b>List of Tables</b>	<b>124</b>
	<b>Bibliography</b>	<b>125</b>
	<b>Acknowledgements</b>	<b>129</b>
	<b>Curriculum Vitae</b>	<b>131</b>

# Introduction

In the Standard Model of electro-weak interactions discussed in chapter 1 the lepton number was added to explain the lack of observed lepton flavor violating processes. However, some more fundamental theories predict such processes with a very small cross section. In addition, recent neutrino experiments have found lepton flavor violating processes in the neutral sector. The search for lepton flavor violation in the charged sector has a long tradition and will be presented with a focus on the  $\mu^+ \rightarrow e^+ \gamma$  decay search in chapter 2.

Currently the MEG collaboration takes a new approach to measure the  $\mu^+ \rightarrow e^+ \gamma$  decay. The goal is to reach a sensitivity of  $1 \times 10^{-13}$ . The experiment setup and all of the detector elements will be introduced in chapter 3.

Furthermore, I will present my contributions to the MEG experiment. The testing and the calibration of the Domino Ring Sampling Chip are discussed in chapter 4. The chip will be used for all detector read out and is, therefore, a key part of the experiment. The analysis framework I developed during my PhD is presented in chapter 5. It is the base of all analysis software used for this experiment. The analysis of the drift chambers starting with the analysis algorithms (chapter 7) followed by the calibration of the chambers (chapter 8) and finally the results of the analysis of the first two engineering runs (chapter 6 and 9) are discussed in detail. A special focus will be given to the results of the positron energy measurement in the Michel decays ( $\mu^+ \rightarrow e^+ \nu_e \bar{\nu}_\mu$ ).





# Part I

## Theory and Phenomenology



# Chapter 1

## The Standard Model and beyond

At present, four fundamental forces are known, the electromagnetic, the weak, the strong and the gravitational force. The theories of the first three are combined into the Standard Model of particle physics (SM)<sup>1</sup>. The SM is a very successful and well tested theory. So far, it is capable to explain almost all elementary particle physics results. Nevertheless, the SM has some theoretical deficiencies, which make most physicist today believe this theory to be a low energy approximation of a more fundamental theory. The main motivations for a more fundamental theory is that one wants the fourth force, the gravitation, to be included. Furthermore, due to the vast difference between the Planck and the electroweak scale, the SM requires the stabilization of light scalar masses. This is known as the hierarchy problem or the fine tuning problem.

This chapter presents the elements of the Standard Model interesting in the context of this thesis. A special focus is given to lepton flavor conservation, which prohibits the  $\mu^+ \rightarrow e^+ \gamma$  decay within the SM. Further, the most popular theories beyond the Standard Model, which break the lepton flavor conservation are presented.

### 1.1 The Standard Model

The SM is a gauge theory based on the gauge symmetry group  $SU(3)_C \times SU(2)_L \times U(1)_Y$  of unitary gauge transformations. It consists of three parts.  $SU(3)_C$  is the non-Abelian symmetry group of the strong interaction. It introduces 8 massless gluons holding a combination of colors out of a color triplet and an anti-color triplet. The theory of strong interaction is formalized in quantum chromo dynamics (QCD). The group  $SU(2)_L \times U(1)_Y$  describes the unified electro-weak force. The  $SU(2)_L$  is the non-Abelian electroweak-isospin group, with which three gauge bosons  $W^+$ ,  $W^-$  and  $W^0$  are associated. The  $U(1)_Y$  is the Abelian hypercharge group. The hypercharge  $Y$  is connected to the electric charge  $Q$  and the isospin  $I_3$  by the relation  $Y = 2(Q - I_3)$ . One

---

<sup>1</sup>As general reference for this Chapter one may take [1], [2] and [3], besides the original papers.

neutral gauge field  $B$  is associated with the hypercharge group. The known electroweak gauge bosons are  $W^+$ ,  $W^-$ ,  $Z^0$  and  $\gamma$ , where  $Z^0$  and  $\gamma$  are obtained out of the mixing of the  $W^0$  and  $B$  boson. The theory of the electro-weak interaction is known as the Glashow-Salam-Weinberg theory.

To introduce mass terms in the Lagrangian the electroweak-isospin group must be spontaneously broken  $SU(2)_L \times U(1)_Y \rightarrow U(1)_{em}$  (spontaneous symmetry breaking SSB). This process is known as the Higgs mechanism.

### 1.1.1 Quantum Electrodynamics

We develop the  $U(1)$  gauge theory of the Quantum Electrodynamics (QED) starting with the Dirac Lagrangian

$$\mathcal{L}_D = \bar{\psi}(i\gamma \cdot \partial - m)\psi, \quad (1.1)$$

where  $\psi$  denotes a wave function,  $\gamma$  is a set of  $4 \times 4$  matrices,  $\partial$  denotes the gauge covariant derivative and  $m$  is a mass term. Out of this we would like to construct an Abelian gauge theory which is invariant under local phase transformation

$$\psi(x) \rightarrow e^{-i\alpha(x)}\psi(x). \quad (1.2)$$

$\mathcal{L}_D$  is not invariant under 1.1. It changes by

$$\delta\mathcal{L}_D = \bar{\psi}(x)\gamma^\mu\psi(x)\partial_\mu\alpha(x). \quad (1.3)$$

To obtain an invariant lagrangian we introduce the transformations

$$\partial^\mu \rightarrow \partial^\mu + ieA^\mu \equiv D^\mu \quad (1.4)$$

and

$$A_\mu \rightarrow A_\mu + \frac{1}{e}\partial_\mu\alpha(x). \quad (1.5)$$

This is analog to the replacement of the momentum variable  $p^\mu \rightarrow p^\mu - eA^\mu$  and the 3-vector  $\mathbf{A} \rightarrow \mathbf{A} + \frac{1}{e}\nabla\alpha$  in classical electrodynamics.

The transformations generate a new term in the Lagrangian

$$\mathcal{L}_{int} = -e\bar{\psi}\gamma^\mu\psi A_\mu, \quad (1.6)$$

which can be identified as the interaction between the Dirac field and a force field. This implies that we further need a term in the Lagrangian describing the force field itself. The simplest gauge invariant object built out of the  $A^\mu$  field is

$$F_{\mu\nu} = \partial_\mu A_\nu - \partial_\nu A_\mu. \quad (1.7)$$

out of which we can construct the Lagrangian

$$\mathcal{L}_A = -\frac{1}{4}F_{\mu\nu}F^{\mu\nu}. \quad (1.8)$$

This is the Lagrangian of a Maxwell field.

By putting all pieces together we obtain the QED Lagrangian

$$\mathcal{L}_{QED} = \bar{\psi}(i \not{D} - m)\psi - e\bar{\psi}\gamma^\mu\psi A_\mu - \frac{1}{4}F_{\mu\nu}F^{\mu\nu} \equiv \bar{\psi}(i \not{D} - m)\psi - \frac{1}{4}F_{\mu\nu}F^{\mu\nu}. \quad (1.9)$$

where  $\not{D}$  and  $\not{\partial}$  is Feynman notation for  $\gamma^\mu D_\mu$  and  $\gamma^\mu \partial_\mu$ .

### 1.1.2 Yang-Mills Theory

The Yang-Mills Theory is an extension of QED to a non-abelian SU(2) theory. We change the relations 1.2, 1.4 and 1.5 to 1.10, 1.12 and 1.14

$$\psi(x) \rightarrow U\psi(x), \quad (1.10)$$

$$U = e^{-ig\frac{\tau^i}{2}\theta^i(x)}, \quad (1.11)$$

$$D_\mu \rightarrow UD_\mu U^{-1}, \quad (1.12)$$

$$D_\mu = \partial_\mu - ig\vec{A}_\mu, \quad \vec{A}_\mu = \frac{\vec{\tau}}{2} \cdot \vec{A}_\mu, \quad (1.13)$$

and

$$\vec{A}_\mu \rightarrow U\vec{A}_\mu U^{-1} - \frac{i}{g}(\partial_\mu U)U^{-1}. \quad (1.14)$$

where

$$\psi(x) = \begin{pmatrix} \psi_1 \\ \psi_2 \end{pmatrix}, \quad (1.15)$$

is a doublet Dirac field,  $\theta^i (i = 1, 2, 3)$  and  $g$  are real parameters and  $\tau^i (i = 1, 2, 3)$  are  $2 \times 2$  Pauli matrices, which act as the generators of the group SU(2). The antisymmetric tensor  $F_{\mu\nu}$  has then to change to

$$\vec{F}_{\mu\nu} = \frac{\vec{\tau}}{2} \cdot \vec{F}_{\mu\nu}, \quad (1.16)$$

$$\vec{F}_{\mu\nu}^i = \partial_\mu A_\nu^i - \partial_\nu A_\mu^i + g\epsilon_{ijk}A_\mu^j A_\nu^k. \quad (1.17)$$

Finally, we can write down the gauge invariant Lagrangian with SU(2) symmetry

$$\mathcal{L} = \mathcal{L}_F + \mathcal{L}_G, \quad (1.18)$$

$$\mathcal{L}_F = \bar{\psi}(i \not{D} - m)\psi, \quad (1.19)$$

$$\mathcal{L}_G = -\frac{1}{2}\text{Tr}(\vec{F}_{\mu\nu} \cdot \vec{F}^{\mu\nu}) = -\frac{1}{4}\vec{F}_{\mu\nu}^i \vec{F}^{i\mu\nu}, \quad (1.20)$$

where  $\mathcal{L}_F$  and  $\mathcal{L}_G$  represent the Lagrangian for the fermion and the gauge field, respectively. Unfortunately, this theory can not be used for describing the weak interaction because all gauge bosons couple with the same constant  $g$  and the Lagrangian does not contain mass terms for them. To obtain a theory of electroweak interaction we need the Higgs mechanism.

### 1.1.3 Spontaneous Symmetry Breaking

To study spontaneous symmetry breaking let us consider the  $U(1)$  global invariant Lagrangian

$$\mathcal{L} = \partial_\mu \phi^* \partial^\mu \phi - V(\phi^* \phi), \quad (1.21)$$

$$V(\phi^* \phi) = m\phi^* \phi + \lambda(\phi^* \phi)^2. \quad (1.22)$$

We can also rewrite the Lagrangian using two real fields  $\varphi_1$  and  $\varphi_2$  which are related to  $\phi$  as  $\phi = (\varphi_1 + i\varphi_2)/\sqrt{2}$

$$\mathcal{L} = \frac{1}{2}\partial_\mu \varphi_1 \partial^\mu \varphi_1 + \frac{1}{2}\partial_\mu \varphi_2 \partial^\mu \varphi_2 - V(\varphi_1^2 + \varphi_2^2), \quad (1.23)$$

We can now extend the potential  $V$  in a power series around its minimum

$$\begin{aligned} V(\varphi_1, \varphi_2) &= V(\varphi_{01}, \varphi_{02}) + \sum_{a=1,2} \left( \frac{\partial V}{\partial \varphi_a} \right)_0 (\varphi_a - \varphi_{0a}) \\ &+ \frac{1}{2} \sum_{a,b=1,2} \left( \frac{\partial^2 V}{\partial \varphi_a \partial \varphi_b} \right)_0 (\varphi_a - \varphi_{0a})(\varphi_b - \varphi_{0b}) + \dots \end{aligned} \quad (1.24)$$

Since the potential has its minimum at  $\phi = \phi_0$ , the second term is zero. The factor  $\left( \frac{\partial^2 V}{\partial \varphi_a \partial \varphi_b} \right)_0 \equiv m_{ab}^2$  is called the mass matrix. When we require  $m^2 = -\mu^2$  ( $\mu^2 > 0$ ) and  $\lambda > 0$  and minimize the potential  $V$  we obtain the condition

$$\varphi_{01}^2 + \varphi_{02}^2 \equiv v^2 = \frac{\mu^2}{\lambda}. \quad (1.25)$$

If we choose  $\varphi_{01} = v$  and  $\varphi_{02} = 0$  the mass matrix becomes

$$m_{ab}^2 = \begin{pmatrix} 2\lambda v^2 & 0 \\ 0 & 0 \end{pmatrix}. \quad (1.26)$$

We can now conclude that we obtained a massive particle  $\varphi'_1 = \varphi_1 - v$  with mass  $2\lambda v^2$  and a massless "Goldstone boson"  $\varphi'_2 = \varphi_2$ . The new Lagrangian

$$\mathcal{L} = \frac{1}{2}(\partial_\mu \varphi'_1)^2 + \frac{1}{2}(\partial_\mu \varphi'_2)^2 - \frac{1}{2}(2\lambda v^2)\varphi_1'^2 + \lambda v \varphi'_1(\varphi_1'^2 + \varphi_2'^2) - \frac{\lambda}{4}(\varphi_1'^2 + \varphi_2'^2)^2 \quad (1.27)$$

has no longer U(1) symmetry. This is called a hidden symmetry or spontaneous symmetry breaking.

### 1.1.4 The Higgs Mechanism

Spontaneous symmetry breaking in a local gauge symmetry is called the Higgs mechanism. We show the mechanism for a Maxwell field with U(1) symmetry and extend it later to SU(2).

#### The U(1) Model

Let us consider the Lagrangian of a Maxwell field and add symmetry breaking terms like

$$\mathcal{L} = -\frac{1}{4}F_{\mu\nu}F^{\mu\nu} + (D_\mu \phi)^*(D^\mu \phi) - V(\phi^* \phi), \quad (1.28)$$

$$V(\phi^* \phi) = -\mu^2 \phi^* \phi + \lambda(\phi^* \phi)^2, \quad (1.29)$$

with  $\mu^2 > 0$  and  $F_{\mu\nu}$  given by 1.7 and  $D_\mu$  given by 1.4. Minimizing the potential  $V$  requires again  $|\phi_0|^2 \equiv \frac{v^2}{2} = \frac{\mu^2}{2\lambda}$ . If we parameterize  $\phi(x)$  as

$$\phi(x) = \frac{1}{\sqrt{2}}(v + \eta(x))e^{i\theta(x)/v}, \quad (1.30)$$

choose the "unitary gauge"  $\alpha(x) = \theta(x)/v$  and substitute  $B_\mu(x) = A_\mu(x) - \frac{1}{ev}\partial_\mu\theta(x)$ , the Lagrangian can be written in a new form

$$\begin{aligned} \mathcal{L} = & \frac{1}{2}\partial_\mu\eta\partial^\mu\eta - \mu^2\eta^2 - \frac{1}{4}F_{\mu\nu}(B)F^{\mu\nu}(B) + \frac{1}{2}(ev)^2B_\mu B^\mu \\ & + \frac{1}{2}e^2B_\mu B^\mu\eta(\eta + 2v) - \lambda v\eta^3 - \frac{\lambda}{4}\eta^4. \end{aligned} \quad (1.31)$$

This Lagrangian describes a massive vector boson  $B$  with mass  $ev$  and a massive scalar  $\eta$  with mass  $\sqrt{2\mu}$ .  $\eta$  is called a "Higgs boson".

### The SU(2) Model

To extend the Higgs mechanism on SU(2) we consider the Lagrangian

$$\mathcal{L} = -\frac{1}{4}F_{\mu\nu}^i F^{i\mu\nu} + (D_\mu\phi)^\dagger(D^\mu\phi) - V(\phi^\dagger\phi), \quad (1.32)$$

$$V(\phi^\dagger\phi) = -\mu^2\phi^\dagger\phi + \lambda(\phi^\dagger\phi)^2, (\mu^2 > 0) \quad (1.33)$$

with  $\mu^2 > 0$  and  $F_{\mu\nu}$  given by 1.16 and  $D_\mu$  given by 1.12. By introducing new real fields  $H(x)$  and  $\xi^i(x)$  ( $i = 1, 2, 3$ ) and parameterizing the field  $\phi(x)$  as

$$\phi(x) = \frac{1}{\sqrt{2}}e^{i\tau^i\xi^i(x)/2v} \begin{pmatrix} 0 \\ v + H(x) \end{pmatrix}, \quad (1.34)$$

we can rewrite the Lagrangian as

$$\begin{aligned} \mathcal{L} = & \frac{1}{2}\partial_\mu H\partial^\mu H - \mu^2 H^2 - \frac{1}{4}F_{\mu\nu}^i(B)F^{i\mu\nu}(B) + \frac{g^2 v^2}{8}B_\mu^i B^{i\mu} \\ & + \frac{g^2}{8}B_\mu^i B^{i\mu} H(2v + H) - \lambda v H^3 - \frac{\lambda}{4}H^4 - \frac{v^4}{4}. \end{aligned} \quad (1.35)$$

We recognize a triplet of massive vector Bosons  $B_\mu^i$  ( $i = 1, 2, 3$ ) with mass  $\frac{1}{2}gv$  and a single massive Higgs boson  $H$  with mass  $\sqrt{2}\mu^2$ .

#### 1.1.5 Glashow-Salam-Weinberg Theory

Since in weak processes only left-handed leptons and right-handed anti-leptons take part we introduce a left-handed doublet  $L$  and a right-handed singlet  $R$  of SU(2) as

$$L = \begin{pmatrix} \nu_e \\ e \end{pmatrix}_L, \quad R = e_R. \quad (1.36)$$

We construct a gauge invariant Lagrangian of  $SU(2)_L \times U(1)_Y$  for these fermions as

$$\begin{aligned} \mathcal{L}_F = & \bar{L}i\gamma^\mu(\partial_\mu - ig\frac{\vec{\tau}}{2} \cdot \vec{A}_\mu + \frac{i}{2}g'B_\mu)L \\ & + \bar{R}i\gamma^\mu(\partial_\mu + ig'B_\mu)R, \end{aligned} \quad (1.37)$$

where  $A_\mu^i$  ( $i = 1, 2, 3$ ) are gauge boson fields with coupling constant  $g$  corresponding to  $SU(2)_L$  and  $B_\mu$  is a gauge boson field with coupling constant  $g'$  corresponding to  $U(1)_Y$ . The Lagrangian of the gauge field is

$$\mathcal{L}_G = -\frac{1}{4}F_{\mu\nu}^i F^{i\mu\nu} - \frac{1}{4}B_{\mu\nu}B^{\mu\nu}, \quad (1.38)$$

the scalar field for the Higgs mechanism can be written as



$$\mathcal{L}_S = (D_\mu \phi)^\dagger (D^\mu \phi) - V(\phi^\dagger \phi), \quad (1.39)$$

$$V(\phi^\dagger \phi) = m^2 \phi^\dagger \phi + \lambda (\phi^\dagger \phi)^2, \quad (1.40)$$

and the coupling between fermion and scalars, called Yukawa interaction terms, are given by

$$\mathcal{L}_Y = -G_e (\bar{L} \phi R + \bar{R} \phi^\dagger L) + h.c. \quad (1.41)$$

The full Lagrangian of the GSW model is then

$$\mathcal{L} = \mathcal{L}_F + \mathcal{L}_G + \mathcal{L}_S + \mathcal{L}_Y. \quad (1.42)$$

After carrying out the Higgs mechanism the first term of 1.39 contains the mass terms of the gauge bosons

$$\mathcal{L}_{mass} = \frac{v^2}{8} (g^2 A_\mu'^1 A'^{1\mu} + g^2 A_\mu'^2 A'^{2\mu} + (g A_\mu'^3 - g' B_\mu')^2) \quad (1.43)$$

If we introduce the charged boson fields  $W^\pm$  which we observe in nature

$$W_\mu^\pm = \frac{A_\mu'^1 \mp i A_\mu'^2}{\sqrt{2}}, \quad (1.44)$$

the first and the second term of 1.43 become  $\frac{1}{4} g^2 v^2 W_\mu^+ W^{-\mu}$ . Therefore, we conclude that the  $W^\pm$  are massive with the mass

$$M_W = \frac{1}{2} g v. \quad (1.45)$$

The third term can be diagonalized into

$$\frac{v^2}{8} (g^2 + g'^2) Z_\mu Z^\mu + 0 \cdot A_\mu A^\mu \quad (1.46)$$

by the orthogonal transformation

$$\begin{pmatrix} Z_\mu \\ A_\mu \end{pmatrix} = \begin{pmatrix} \cos \theta_W & -\sin \theta_W \\ \sin \theta_W & \cos \theta_W \end{pmatrix} \begin{pmatrix} A_\mu'^3 \\ B_\mu' \end{pmatrix}. \quad (1.47)$$

Thus we obtain a massless photon and a massive Z boson with mass

$$M_Z = \frac{1}{2} v \sqrt{g^2 + g'^2}. \quad (1.48)$$

The mixing angle  $\theta_W$  is called the Weinberg angle and fulfills the relation

$$\tan\theta_W = \frac{g'}{g}. \quad (1.49)$$

The Higgs mechanism changes the potential  $V$  of  $\mathcal{L}_S$  to

$$V(\phi'^\dagger\phi') = -\frac{\mu^2 v^2}{4} + \frac{1}{2}(2\mu^2)H^2 + \lambda v H^3 + \frac{\lambda}{4}H^4, \quad (1.50)$$

in which we can identify a Higgs boson  $H$  with mass

$$M_H = \sqrt{2\mu^2}. \quad (1.51)$$

The fermion masses are obtained by investigating the Yukawa interaction term  $\mathcal{L}_Y$ , which becomes

$$\mathcal{L}_Y = -\frac{G_e v}{\sqrt{2}}\bar{e}'e' - \frac{G_e}{\sqrt{2}}H\bar{e}'e'. \quad (1.52)$$

Therefore the neutrino mass is zero and the electron mass is

$$m_e = \frac{G_e}{\sqrt{2}}v. \quad (1.53)$$

A mass term for the neutrino can, in principle, be generated by introducing a new Higgs doublet

$$\phi_c = -i\tau_2\phi^* = \begin{pmatrix} -\bar{\phi}^0 \\ \phi^- \end{pmatrix}. \quad (1.54)$$

In  $SU(2)$ ,  $\phi_c$  transforms identically to  $\phi$  but has opposite weak hypercharge to  $\phi$ . The Lagrangian will then transform to

$$\mathcal{L} = -m_e\bar{e}e - m_\nu\bar{\nu}\nu - \frac{m_e}{v}\bar{e}eh - \frac{m_\nu}{v}\bar{\nu}\nu h. \quad (1.55)$$

However, in this construction there is no good reason for the neutrino mass to be small.

If we extend the GSW model to more than one Lepton family new terms in the Lagrangian of the Yukawa interaction are allowed, which, after symmetry breaking, leads to possible flavor mixing terms in the Lagrangian

$$\mathcal{L}_F^{(mass)} = \begin{pmatrix} \bar{e}_L & \bar{\mu}_L \end{pmatrix} \begin{pmatrix} m_{ee} & m_{e\mu} \\ m_{\mu e} & m_{\mu\mu} \end{pmatrix} \begin{pmatrix} e_R \\ \mu_R \end{pmatrix} + h.c. \quad (1.56)$$

However, it can be shown that, in the case of massless neutrinos, the mixing angle can always be rotated away and therefore, the mass eigenstates become equal to the weak eigenstates. Hence, we can conclude that in the SM there is no flavor changing process in the charged lepton sector for massless neutrinos.

## 1.2 Neutrino masses

In the chiral representation fermions are usually represented by a Dirac spinor

$$\psi_D = \psi_R + \psi_L = \begin{pmatrix} \eta_\alpha \\ \bar{\xi}^{\dot{\alpha}} \end{pmatrix}. \quad (1.57)$$

Nevertheless, there is also the possibility to form them as Majorana fermions

$$\psi_{M_1} = \psi_R + (\psi_R)^C = \begin{pmatrix} \eta_\alpha \\ \bar{\eta}^{\dot{\alpha}} \end{pmatrix}. \quad (1.58)$$

$$\psi_{M_2} = \psi_L + (\psi_L)^C = \begin{pmatrix} \xi_\alpha \\ \bar{\xi}^{\dot{\alpha}} \end{pmatrix}. \quad (1.59)$$

Mass terms for Majorana fermions violate several U(1) global symmetries. Therefore, they are not allowed for charged particles like the electron, but for neutrinos we have to include them in the Lagrangian as

$$\mathcal{L}_m = -\frac{1}{2}m_R\overline{(\nu_R)^c}\nu_R - \frac{1}{2}m_L\overline{(\nu_L)^c}\nu_L - \frac{1}{2}m_D\bar{\nu}_R\nu_L + h.c., \quad (1.60)$$

where  $\nu_R$  and  $\nu_L$  denote right- and left-handed neutrinos. We can also rewrite the Lagrangian as a matrix equation

$$\mathcal{L}_m = -\frac{1}{2} \begin{pmatrix} \overline{(\nu_L)^c} & \bar{\nu}_R \end{pmatrix} M_\nu \begin{pmatrix} \nu_L \\ (\nu_R)^c \end{pmatrix} + h.c., \quad (1.61)$$

with the mass matrix given by

$$M_\nu = \begin{pmatrix} m_L & m_D \\ m_D & m_R \end{pmatrix}. \quad (1.62)$$

### 1.2.1 Seesaw Mechanism

There exists one theory which can describe the smallness of the neutrino mass in a natural way, the so-called seesaw mechanism. In this scenario the left-handed Majorana mass is set to zero ( $m_L = 0$ ) and the Dirac mass is required to be much smaller than the right-handed Majorana mass ( $m_D \ll m_R$ ). The eigenvalues of the mass matrix 1.62 then become

$$m_N \simeq m_R, \quad (1.63)$$

$$m_\nu \simeq \frac{m_D^2}{m_R}, \quad (1.64)$$

where  $m_N$  is the mass of a very heavy neutrino and  $m_\nu$  is the mass of the currently observed neutrino. The mass  $m_D$  is of the order of 100 GeV. If the mass  $m_R$  is set to  $10^{15}$  GeV the neutrino mass  $m_\nu$  becomes naturally 100 eV.

### 1.2.2 Neutrino Mixing

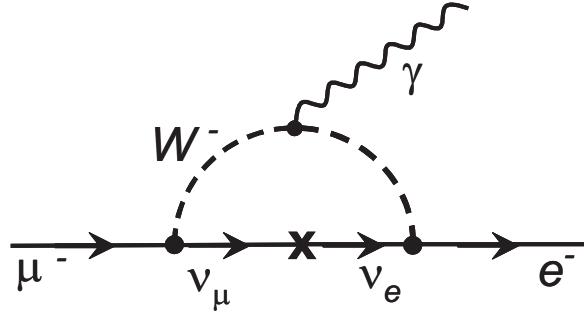


Figure 1.1: Feynman diagram for the  $\mu^+ \rightarrow e^+ \gamma$  decay with neutrino oscillation.

If the neutrino masses are non zero the neutrino can be transformed from its mass eigenstate  $\nu_i$  to its weak eigenstate  $\nu_l$  by

$$|\nu_l\rangle = \sum_i U_{li} |\nu_i\rangle \quad (1.65)$$

where  $U$  is a unitary mixing matrix. The probability of finding a  $\nu_{l'}$  in an original  $\nu_l$  beam is

$$P_{\nu_l \nu_{l'}}(x) = |\langle \nu_{l'} | \nu_l(x) \rangle|^2 = \sum_{i,j} |U_{li} U_{l'i}^* U_{lj}^* U_{l'j}| \cos \left( \frac{2\pi x}{L_{ij}} - \varphi_{l'ij} \right) \quad (1.66)$$

where

$$\varphi_{l'ij} = \text{Arg}(U_{li} U_{l'i}^* U_{lj}^* U_{l'j}) \quad (1.67)$$

and  $L_{ij}$  are called oscillation lengths. For the electron neutrino to muon neutrino transition this leads to

$$P(\nu_e \rightarrow \nu_\mu) = \sin^2 2\theta \sin^2 \frac{1.27 \Delta m^2 (eV^2) L(m)}{E(MeV)} \quad (1.68)$$

where  $\theta$  is the mixing angle,  $\Delta m^2$  is the square mass difference of the two neutrinos,  $E$  is their energy and  $L$  is the travelled distance. This leads to a transition rate of the  $\mu^+ \rightarrow e^+ \gamma$  decay of approximately

$$\Gamma(\mu \rightarrow e\gamma) \approx \frac{G_F^2 m_\mu^2}{192\pi^3} \cdot \left(\frac{\alpha}{2\pi}\right) \cdot \sin^2 2\theta \sin^2 \left(\frac{1.27\Delta m^2}{M_W^2}\right) \quad (1.69)$$

Normalized to the normal muon decay we obtain the branching ratio

$$B.R.(\mu \rightarrow e\gamma) = \frac{\Gamma(\mu \rightarrow e\gamma)}{\Gamma(\mu \rightarrow e\nu\nu)} \approx \left(\frac{\alpha}{2\pi}\right) \cdot \sin^2 2\theta \left(\frac{\Delta m^2}{M_W^2}\right)^2 \approx 10^{-55} \quad (1.70)$$

where  $\sin^2 2\theta$  and  $\Delta m^2$  were assumed to be 0.92 and  $7 \cdot 10^{-5} eV^2$ , respectively.

Therefore, we can conclude that for neutrinos with non vanishing masses lepton flavor changing processes like the one in figure 1.1 occur. However, the branching ratio of this process is way beyond the current experimental limit.

### 1.3 Beyond the Standard Model

The SM describes all experimental data except recent neutrino oscillation measurements. Nevertheless, the theory is very unsatisfying from a theoretical point of view. Many elements of the theory have to be adjusted to data or are even motivated by experimental observations like the gauge groups the fermion groups (doublets vs. singlets), the higgs mass and so on. Furthermore, one would like to have a more fundamental theory which also includes gravity. There exist various different ideas of possible extension of the SM and also complete new approaches. In this chapter we will restrict ourself on Grand Unified Theories (GUT) and Supersymmetry (SUSY) since only the combined SUSY-GUT theories are subjects of this thesis.

#### 1.3.1 Grand Unified Theories (GUT)

The idea of GUTs is to embed the groups  $SU(3)_C * SU(2)_L * U(1)_Y$  in a larger group of at least rank 4. As an example of such theories we discuss in this section the group  $SU(5)$  (see [4]). In this group the particle and antiparticle are represented by a  $\bar{5}$ -plet and a 10-plet :

$$\bar{5} = \begin{pmatrix} d_g^C \\ d_r^C \\ d_b^C \\ e^- \\ -\nu_e \end{pmatrix} \quad 10 = \frac{1}{\sqrt{2}} \begin{pmatrix} 0 & +u_b^C & -u_r^C & -u_g & -d_g \\ -u_b^C & 0 & +u_g^C & -u_r & -d_r \\ +u_r^C & -u_g^C & 0 & -u_b & -d_b \\ +u_g & +u_r & +u_b & 0 & -e^+ \\ +d_g & +d_r & +d_b & +e^+ & 0 \end{pmatrix}_L. \quad (1.71)$$

The corresponding gauge fields can be written as

$$24 = \left( \begin{array}{ccc|cc} G_{11} - \frac{2B}{\sqrt{30}} & G_{12} & G_{13} & X_1^C & Y_1^C \\ G_{21} & G_{22} - \frac{2B}{\sqrt{30}} & G_{23} & X_2^C & Y_2^C \\ G_{31} & G_{32} & G_{33} - \frac{2B}{\sqrt{30}} & X_3^C & Y_3^C \\ \hline X_1 & X_2 & X_3 & \frac{W^3}{\sqrt{2}} + \frac{3B}{\sqrt{30}} & W^+ \\ Y_1 & Y_2 & Y_3 & W^- & -\frac{W^3}{\sqrt{2}} + \frac{3B}{\sqrt{30}} \end{array} \right), \quad (1.72)$$

where G denotes the gluon fields, W and B gauge fields and X and Y are new gauge bosons, which mix the quarks with leptons. Therefore, this model allows e.g. proton decays like  $p \rightarrow e^+ \pi^0$ . The lifetime of a proton can be obtained by

$$\tau_p \approx \frac{M_X^4}{\alpha_3^2 m_p^5}. \quad (1.73)$$

The experimental limit of  $\tau_p > 5 \cdot 10^{32}$  yrs for the dominant decay mode  $p \rightarrow e^+ \pi^0$  implies

$$M_X \geq 10^{15} \text{ GeV}, \quad (1.74)$$

which contradicts with the SU(5) unification scale of the couplings. Therefore, this model is ruled out. Furthermore, the request for the unification of the coupling constants at the unification scale

$$\alpha_1(M_X) = \alpha_2(M_X) = \alpha_3(M_X) = \alpha_U, \quad (1.75)$$

requires

$$\sin^2 \theta_W(m_W) = \frac{3}{8} - \alpha(m_W) \frac{109}{48\pi} \ln \frac{M_X}{m_W}, \quad (1.76)$$

or

$$\sin^2 \theta_W(m_W) = 0.214 \pm 0.003 \pm 0.006 \ln \left[ \frac{0.16 \text{ GeV}}{\Lambda_{\overline{MS}}} \right], \quad (1.77)$$

where  $\theta_W$  denotes the Weinberg Angle and  $\Lambda_{\overline{MS}}$  is the QCD scale parameter. This, however, contradicts with the measurements on the W- and Z-masses of [5], [6], [7], [8], [9], [10], [11] and [12].

### 1.3.2 Supersymmetry (SUSY)

Supersymmetry connects fermionic  $|F\rangle$  and bosonic states  $|B\rangle$ :

$$Q|B\rangle = |F\rangle \quad \text{and} \quad Q|F\rangle = |B\rangle. \quad (1.78)$$

The supersymmetric operator  $Q$  must carry spin = 1/2. The generator  $Q$  and its hermitian conjugate  $Q^\dagger$  must satisfy the graded Lie algebra:

$$\begin{aligned} \{Q, Q^\dagger\} &= P^\mu, \\ \{Q, Q\} &= \{Q^\dagger, Q^\dagger\} = 0, \\ [P^\mu, Q^\dagger] &= 0. \end{aligned} \quad (1.79)$$

$P^\mu$  is the spacetime translation operator and transforms under Lorentz transformation as a spin-1 object. The irreducible representations of the SUSY algebra 1.79 are called supermultiplets. Equation 1.79 implies that the members of a supermultiplet have the same masses and the same quantum numbers. Since no supersymmetric partners for the observed particles have been found, supersymmetry must be broken. However, spontaneous symmetry breaking as used for the Higgs mechanism is not working in this case. Therefore, SUSY has to be broken explicitly by introducing soft SUSY-breaking terms in the Lagrangian.

### 1.3.3 SUSY GUT

As an example of how SUSY GUT scenarios can introduce LFV processes we discuss SU(5) SUSY GUT. In this case the the soft SUSY-breaking mass terms at the Planck scale are given by

$$\mathcal{L}_{soft} = -m_0^2 \{ \tilde{T}_i^\dagger \tilde{T}_i + \tilde{\bar{F}}_i^\dagger \tilde{\bar{F}}_i \} - \left[ m_0 A_0 \{ \frac{1}{8} (y_u)_{ij} \tilde{T}_i \cdot \tilde{T}_j \cdot H(5) + (y_d)_{ij} \tilde{\bar{F}}_i \cdot \tilde{T}_j \cdot \bar{H}(5) \} + H.c. \right]. \quad (1.80)$$

$\bar{F}_i$  and  $T_i$  are the  $\bar{5}$  and 10 representations of the SU(5) group, respectively.  $H(5)$  and  $\bar{H}(5)$  are two Higgs fields associated with the 5 and  $\bar{5}$  representations, respectively. The matrix  $(y_u)_{ij}$  corresponds to the Yukawa coupling matrix for the up-type quarks, and  $(y_d)_{ij}$  to that for the down-type quarks, and the leptons.  $m_0$  is the universal scalar mass, and  $A_0$  is the universal trilinear coupling.

At this stage, there is no LFV in the slepton sector. However, when taking into account the radiative corrections to the soft SUSY-breaking mass terms due to the Yukawa coupling constants, all members of  $T_i$  are obtained by

$$m_T^2 \simeq \begin{pmatrix} m^2 & & \\ & m^2 & \\ & & m^2 + \Delta m^2 \end{pmatrix} \quad (1.81)$$

and

$$\Delta m^2 \simeq -\frac{3}{8\pi^2} |(y_u)_{33}|^2 m_0^2 (3 + |A_0|^2) \ln\left(\frac{M_P}{M_G}\right), \quad (1.82)$$

where  $M_P$  and  $M_G$  denote the reduced Planck mass and the GUT scale. In the basis where the Yukawa coupling constant for leptons is diagonalized,  $V_R y_e V_L^\dagger = \text{diagonal}$ , we finally obtain

$$(m_{\tilde{e}_R}^2)_{ij} \simeq -\frac{3}{8\pi^2} (V_R)_{i3} (V_R)_{j3}^* |y_u^{33}|^2 m_0^2 (3 + |A_0|^2) \ln\left(\frac{M_P}{M_G}\right). \quad (1.83)$$

This becomes a source of a  $\mu^+ \rightarrow e^+ \gamma$  decay through the diagrams in figure 1.2. The branching ratio reaches the order of  $10^{-14}$  for a slepton mass of a few  $100 \text{ GeV}/c^2$ .



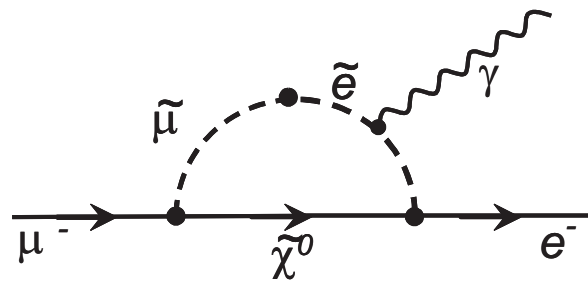


Figure 1.2: Feynman diagram for the  $\mu^+ \rightarrow e^+ \gamma$  decay in SU(5) SUSY GUT.



# Chapter 2

## Search for the $\mu^+ \rightarrow e^+ \gamma$ decay

### 2.1 Phenomenology of the $\mu^+ \rightarrow e^+ \gamma$ decay

In section 1.3.3 we discussed lepton flavor violation in the case of a SUSY-SU(5) model. We saw that in this model the  $\mu^+ \rightarrow e^+ \gamma$  decay reaches a branching ratio of up to  $10^{-14}$ , which is in the reach of possible future experiments. However, this model can be also modified to include higher dimensional terms or different SU(5) representations of Higgs fields which would allow for branching ratios of up to  $10^{-12}$ . Furthermore, the same calculations can be applied to a SUSY-SU(10) scenario which also leads to branching ratios of up to  $10^{-12}$ . The dominant processes in the SUSY-SU(10) model are shown in figure 2.1. The variation of the branching ratio as a function of the slepton mass  $m_{\tilde{e}}$  is shown in figure 2.2 for SUSY-SU(5) models.

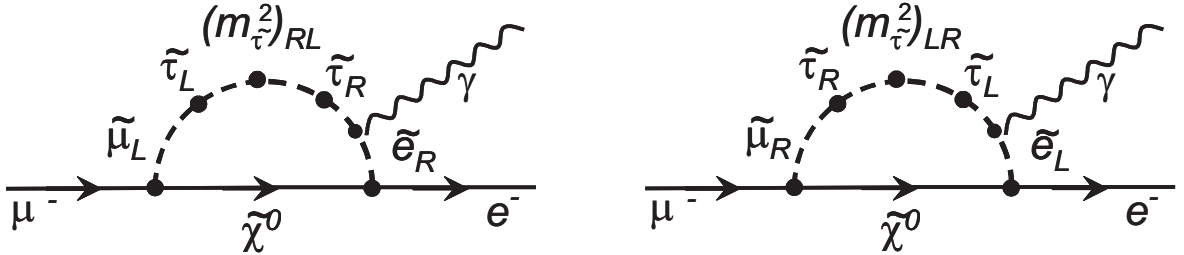


Figure 2.1: Feynman diagrams in SO(10) SUSY GUT which give dominant contributions to the  $\mu^+ \rightarrow e^+ \gamma$  process.

Including neutrino mixing in SUSY-GUT models can also enhance the branching ratio of  $\mu^+ \rightarrow e^+ \gamma$ . Furthermore, the combination of the recent SNO solar neutrino observations [13], [14] and [15] with all previous measurements constrain the mixing parameters to two allowed regions. The parameter spaces of the so-called Mikheyev-Smirnov-Wolfenstein (MSW) large mixing angle solution (LMA) and the MSW large angle-low  $\Delta m^2$  (LOW) solution are shown on the left side of figure 2.3. On the right

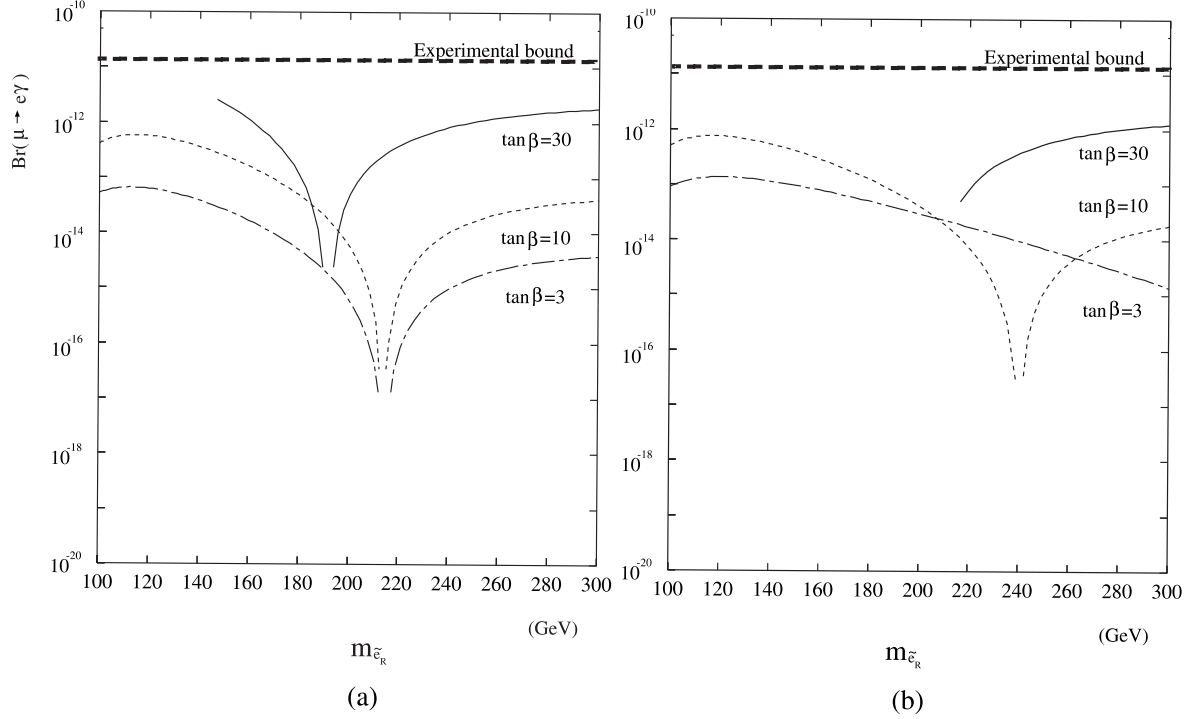


Figure 2.2: Predictions of  $\mu^+ \rightarrow e^+ \gamma$  branching ratio in SU(5) SUSY models. The branching ratio is plotted for different values of  $\tan\beta$  as a function of the right-handed selectron mass and for a) positive values of the Higgs mass expectation value and b) negative values of the Higgs mass expectation value.

side of figure 2.3 the predictions for the branching ratios of the  $\mu^+ \rightarrow e^+ \gamma$  decay corresponding to the MSW solutions are shown. The width of the bands is associated with the possible values of  $\tan\beta$ , which is the ratio of neutral Higgs field vacuum expectation values. The lowest  $\tan\beta$  values, shown in figure 2.2, corresponding to lower  $\mu^+ \rightarrow e^+ \gamma$  decay rates, are highly disfavored by the recent analysis of the LEP data [16].

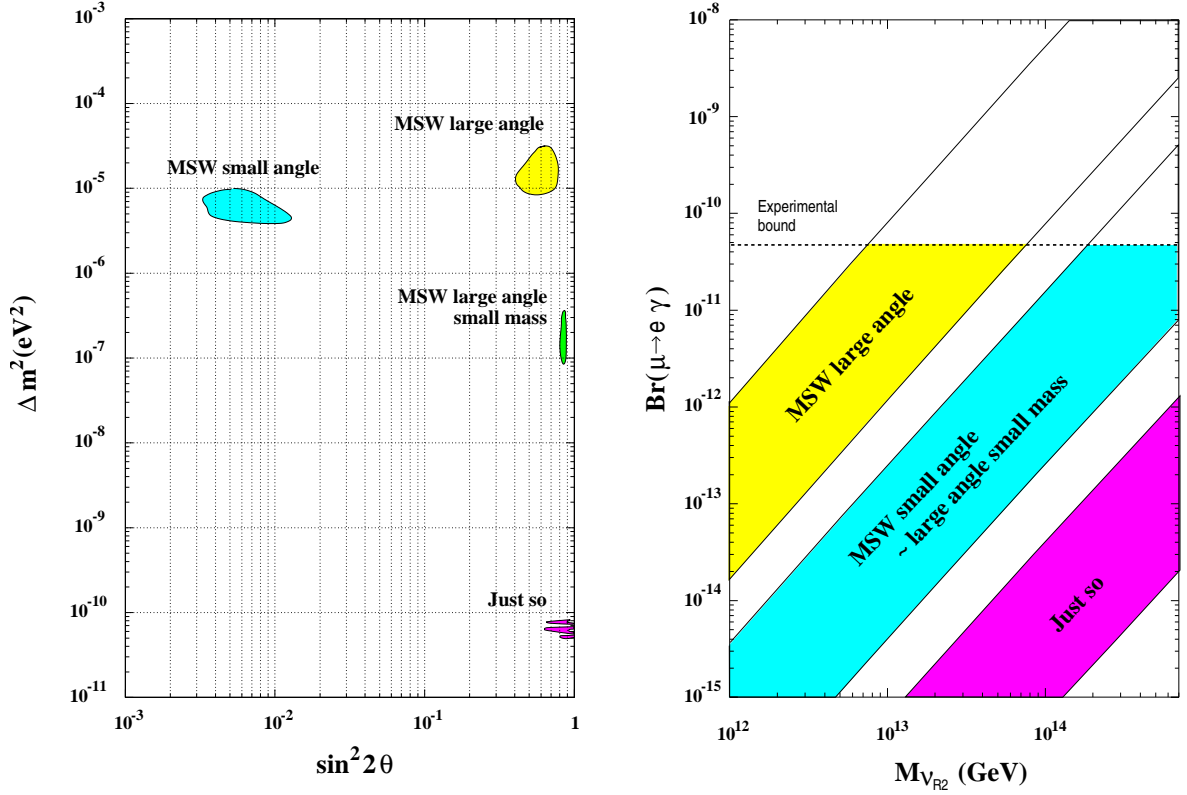


Figure 2.3: Possible solutions for neutrino oscillation (left) and corresponding  $\mu^+ \rightarrow e^+\gamma$  branching ratios (right) as a function of the mass of the right-handed Gauge singlet  $\nu_{R2}$ . The vacuum solution case (labeled as "Just so") is shown for completeness though excluded by the SNO experiment.

## 2.2 Experimental status of $\mu^+ \rightarrow e^+\gamma$ decay search

The search for a  $\mu^+ \rightarrow e^+\gamma$  decay has a long tradition [17]. The first experiment, made by Hincks and Pontecorvo [18], was carried out 14 years after the discovery of the muon in a Wilson cloud chamber by Kunze in 1933 [19]. The search was significantly improved when artificially produced muons at accelerators became available, first by using stopped pion beams, later directly with muon beams from the meson factories. The sensitivity mainly improved with the improvements on the muon sources. However, with stronger muon sources also the number of background events increased, which required the detectors to have better background rejections. This meant that to reach better sensitivity the energy resolution of the electron  $\Delta E_e$ , the energy resolution of the photon  $\Delta E_\gamma$ , the timing resolution  $\Delta t_{e\gamma}$  and the angular resolution  $\Delta \theta_{e\gamma}$  of the detector had to be improved. The history of the  $\mu^+ \rightarrow e^+\gamma$  decay search is summarized in figure 2.4 and table 2.1.

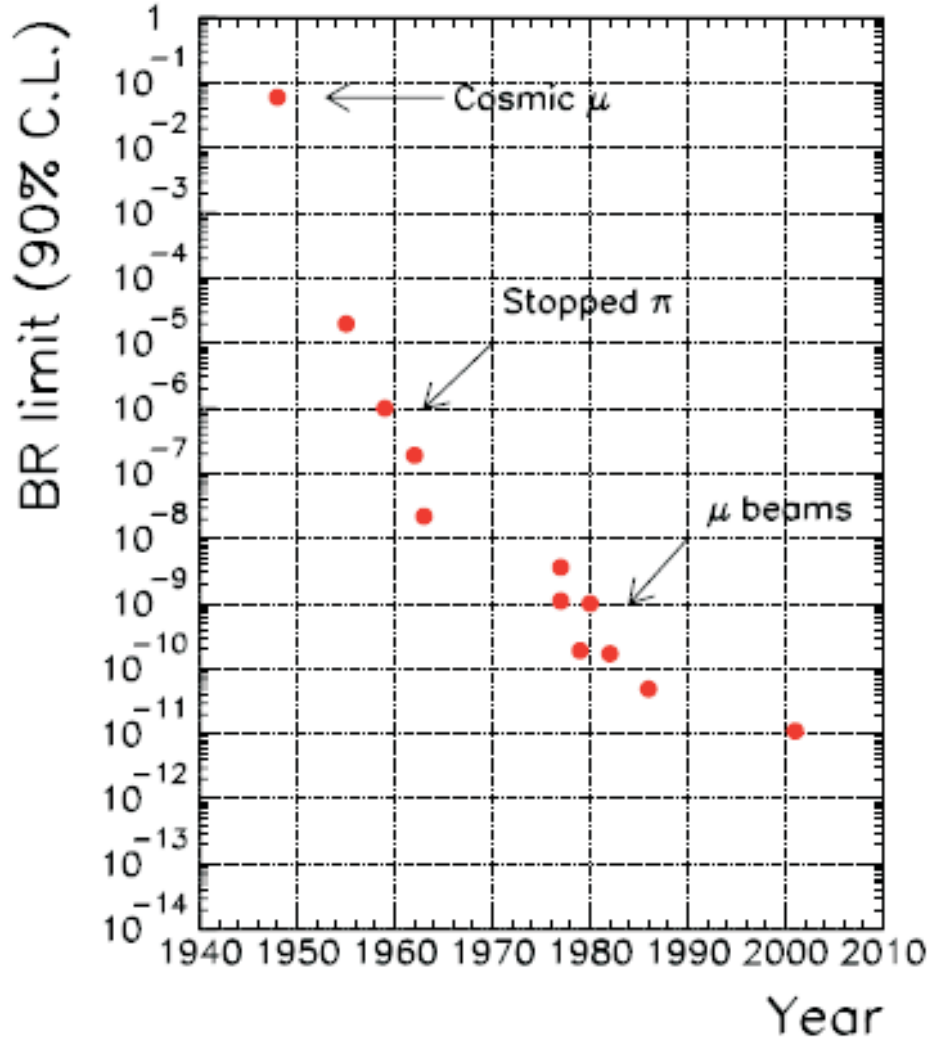


Figure 2.4: Improvement of the 90% CL upper limit on the  $\mu^+ \rightarrow e^+\gamma$  decay branching fraction over the years.

## 2.3 Event and backgrounds signature

$\mu^+ \rightarrow e^+\gamma$  decays are typically measured by stopping muons in a target. Therefore, the muon decays at rest into a positron and a photon. The two decay particles are emitted at the same time and move collinearly back-to-back with their momenta equal to half of the muon mass ( $m_\mu/2 = 52.8$  MeV). The searches are carried out by using positive muon, since a negative muon would be captured by a nucleus when it is stopped inside the target. There are two major backgrounds for the  $\mu^+ \rightarrow e^+\gamma$  decay process (see

Place/ Experiment	Year	$\Delta E_e$	$\Delta E_\gamma$	$\Delta t_{e\gamma}$	$\Delta\theta_{e\gamma}$	Upper limit	Ref.
TRIUMF	1977	10.0%	8.7%	6.7ns	-	$< 3.6 \cdot 10^{-9}$	[20]
SIN	1980	8.7%	9.3%	1.4ns	-	$< 1.0 \cdot 10^{-9}$	[21]
LANL	1982	8.8%	8.0%	1.9ns	37mrad	$< 1.7 \cdot 10^{-10}$	[22]
Crystal Box	1988	8.0%	8.0%	1.8ns	87mrad	$< 4.9 \cdot 10^{-11}$	[23] and [24]
MEGA	1999	1.2%	4.5%	1.6ns	15mrad	$< 1.2 \cdot 10^{-11}$	[25]
MEG	MC	0.8%	4.3%	0.14ns	17mrad	$< 1.6 \cdot 10^{-13}$	

Table 2.1: Historical Progress of search for  $\mu^+ \rightarrow e^+\gamma$  since the era of meson factories with 90% C.L. upper limits. The resolutions quoted are given as a full width at half maximum (FWHM). For comparison also the resolution of the MEG experiment is given. The values are obtained by a revised Monte Carlo simulation. This simulation does not take into account any of the outputs of this work.

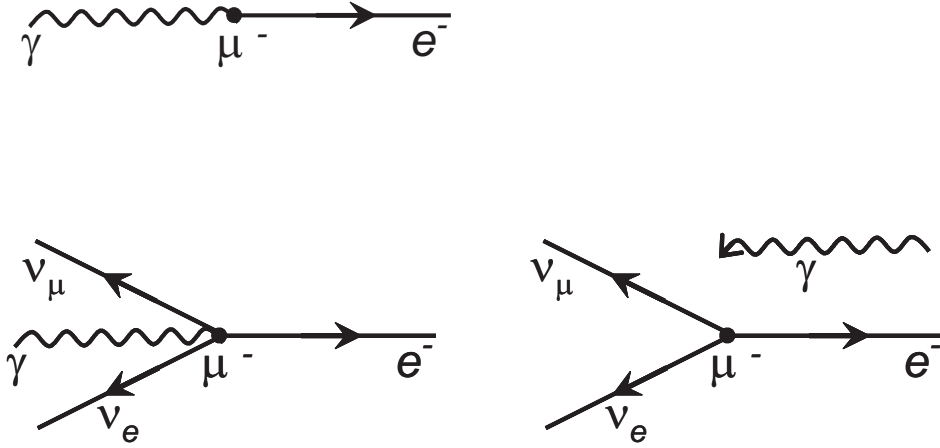


Figure 2.5: Feynman diagram of the  $\mu^+ \rightarrow e^+\gamma$  signal and background events. Upper left is the signal topology. Lower left shows a radiative decay and the lower right diagram illustrate a accidental background event.

figure 2.5). One is a physics background from radiative muon decay,  $\mu^+ \rightarrow e^+\nu_e\bar{\nu}_\mu\gamma$ . When the  $e^+$  and the photon are emitted nearly back-to-back with the two neutrinos carrying off only little energy this decay could look like a  $\mu^+ \rightarrow e^+\gamma$  decay in the detector. The other background is an accidental coincidence of an  $e^+$  in a normal muon decay,  $\mu^+ \rightarrow e^+\nu_e\bar{\nu}_\mu$ , together with a photon carrying the right energy and momentum to simulate a  $\mu^+ \rightarrow e^+\gamma$  decay. The sources of the latter might be either a radiative muon decay, annihilation-in-flight, or external bremsstrahlung of an  $e^+$  from a normal muon decay. These backgrounds are described in more detail in the following section.

## 2.4 Background rejection

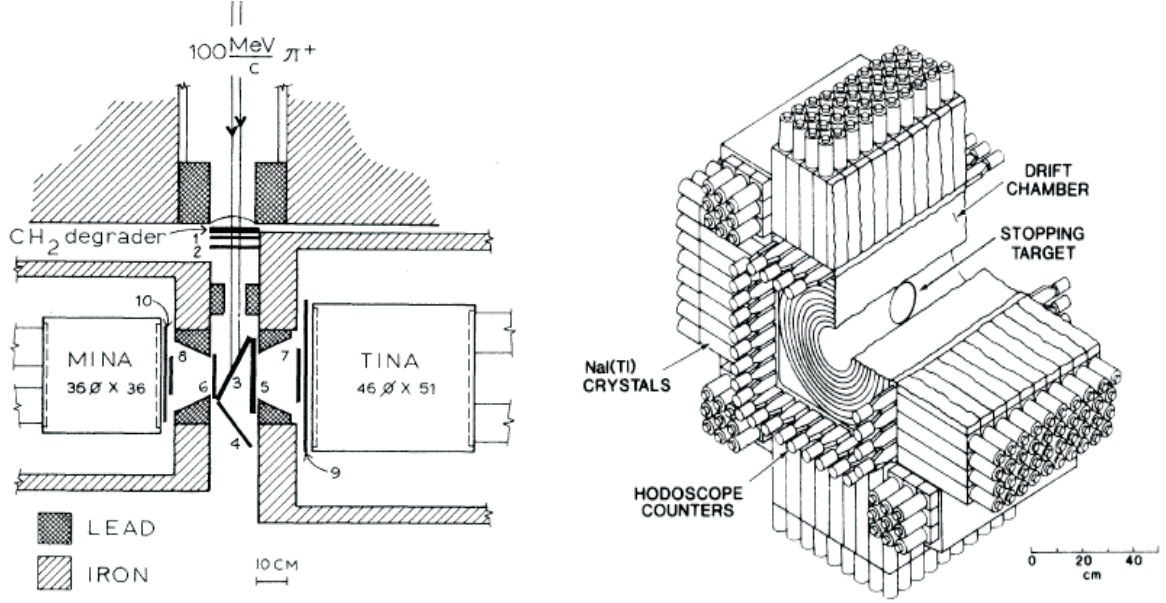


Figure 2.6: A schematic view of the TRIUMF experiment on the left side and a schematic cutaway diagram of the Crystal Box detector on the right side.

The background rejection capability of an experiment is directly linked to its experimental resolutions of the photon and positron four momenta measurement. In the first experiments spark chambers were used to detect both the positron and the photon [18]. Later on the configuration with two back-to-back large NaI crystals (see figure 2.6) became common [20], [21]. This setup allowed a better energy and timing determination. The technique was refined by the Crystal Box experiment where an almost  $4\pi$  segmented NaI calorimeter surrounded the target region [23]. The pion production cross section increases with the proton energy. Therefore, the number of produced pions can be increased by using a higher beam energy. This, however, implied also that a thick target had to be used to stop the primary particles. Since the target thickness contributes heavily to the positron energy loss, a good positron energy resolution could not be obtained. This situation changed when "surface" muon beams were introduced [26], originating from pions decaying on the surface of a pion production target. In this case low energy muon beams ( $p = 28 \text{ MeV}/c$ ) of high intensity can be stopped in thinner targets. In the MEGA experiment the positron was detected in cylindrical tracking chambers in a solenoid magnetic field, which lead to a far better energy resolutions as shown in table 2.1.



## 2.5 Future of LFV searches

To improve the current limit the resolution has to be improved. The MEG collaboration wants to achieve this with a high intensity muon beam together with a thin target. For the precise measurement of the positron momentum and good pileup rejection a nonuniform magnetic spectrometer together with drift chambers are used, while fast scintillators are used to provide extremely good timing for the positron. To obtain a good measurement of the photon momentum and direction the magnet is designed to have a very thin wall, not to degrade the photon energy. The timing information of the photon has to be improved significantly compared to the one given by a NaI calorimeter. Therefore, the MEG experiment proposes to use a novel liquid Xe calorimeter with far better timing capabilities. In the following we will describe the MEG experiment with particular emphasis on the studies related to the drift chambers and the DAQ system.



## Part II

### The MEG experiment



# Chapter 3

## Experiment Setup

### 3.1 Introduction

The MEG experiment is located at the Paul Scherrer Institute in Switzerland where it is operated by a collaboration with members from Italy, Japan, Russia, the USA and Switzerland. Its goal is to measure the  $\mu^+ \rightarrow e^+ \gamma$  decay with a sensitivity of  $1 \times 10^{-13}$ .

The MEG detector is optimized to detect a coincidence of a back-to-back positron and photon pair, each particle having an energy of 52.8 MeV. Muons from a high intensity, continuous beam are stopped in a thin target where they decay at rest. The positron energy is measured by a set of drift chambers placed in an inhomogeneous magnetic field while the timing is determined by a set of timing counters. The photon energy and timing are measured by a liquid Xe scintillating calorimeter.

To reach the goal of a sensitivity of  $1 \times 10^{-13}$  the individual detector components must reach the resolutions given in table 2.1.

The subsequent sections discuss all detector parts in detail.

## 3.2 Beam and Target

The beam is produced by a ring cyclotron which accelerates protons to an energy of up to 590 MeV. The beam current, which is presently the highest available worldwide, reaches 2.0 mA. The proton beam is then transformed to a meson beam by shooting it to two carbon targets, the so called M-target and the E-target. The two targets are rotating truncated cones made of isotropic graphite. The target is slanted so that the beam hits the target uniformly and allows a cooling of the target by thermal radiation. The M-target is 7 mm thick while the E-target can be either 40 mm or 60 mm thick, measured in the direction of the proton beam. The meson beam produced by the target consists mainly of charged pions which themselves decay in flight to muons and electrons of both charges. The beam extracted in the  $\pi E5$  area is coming from the thick E-target and consists of low energy pions and muons (see figure 3.1). The main characteristics of the beam are listed in table 3.1.

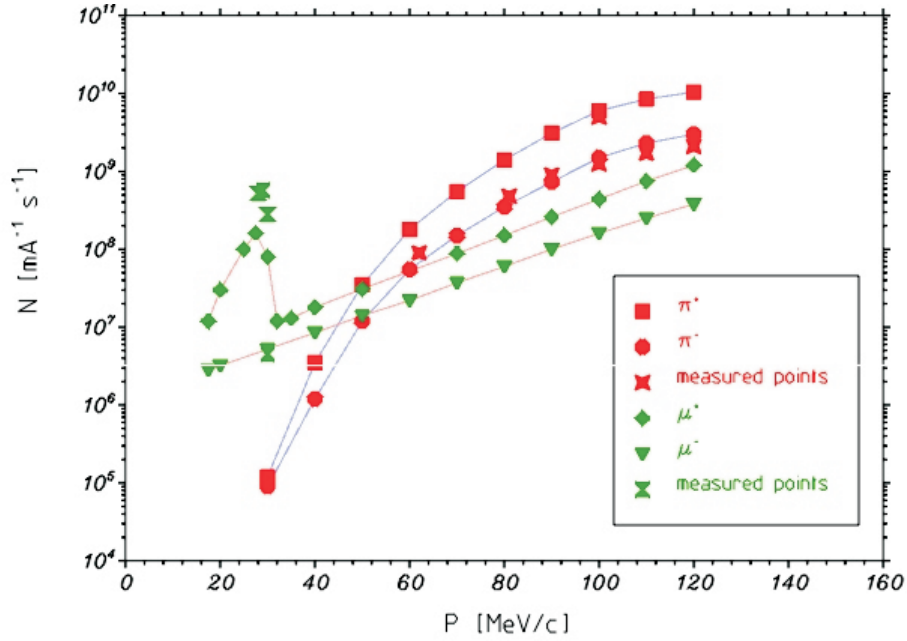


Figure 3.1: Pion and muon flux in the  $\pi E5$  area. The deviations between the measured and the expected fluxes is due to uncertainties in the beam transmission from the production target to the area.

### 3.2.1 MEG specific beam line components

The MEG experiment is located in the  $\pi E5$  area. Inside the area the beam must be manipulated to reduce the fraction of the positron content and reduce the muon

solid angle acceptance	150 msr
momentum range	20 – 120 MeV/c
length	10.4 m
momentum band (FWHM)	10%
momentum resolution (FWHM)	2%
horizontal emittance	15.3 cm·rad
vertical emittance	3.6 cm·rad
spot size	4×4 cm <sup>2</sup>

Table 3.1: Main properties of the  $\pi$ E5 beam line.

momentum in order to stop them in a 175  $\mu$ m target. This is accomplished by placing several beam separating and focussing elements in the beam line (see figure 3.2).

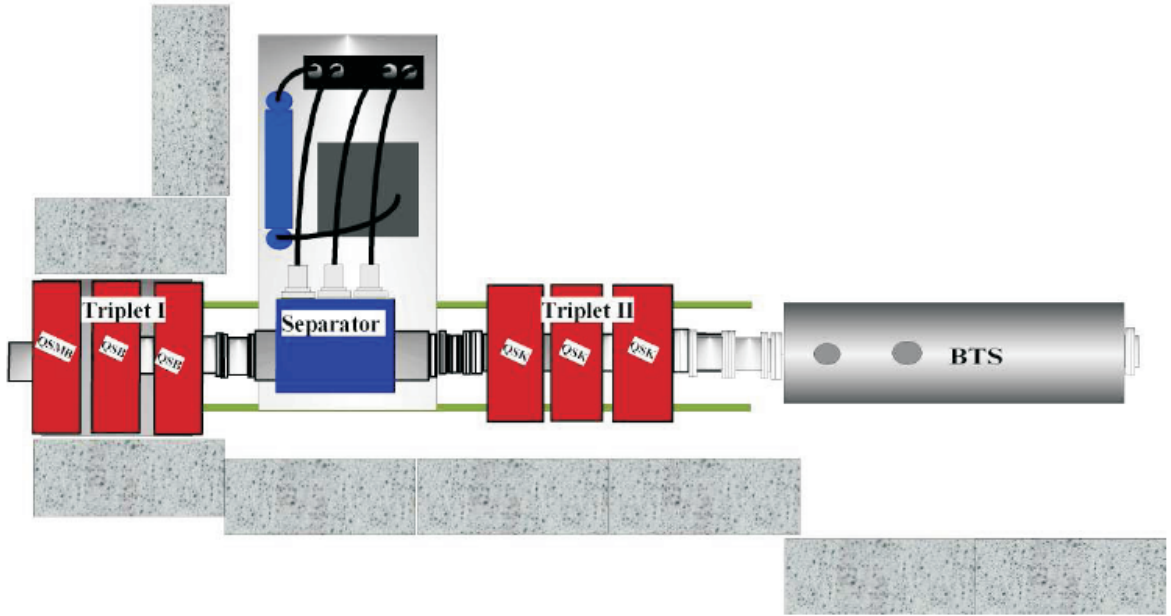


Figure 3.2: MEG specific beam line components. The BTS couples the beam to the cobra magnet shown in figure 3.3.

- A quadrupole triplet used to focus the beam (Triplet I).
- An electrostatic separator (Wien filter) with a 19 mm gap is used to separate muons and positrons.
- A second quadrupole triplet refocuses the muon beam after the muon-positron separation (Triplet II).

- A beam transport solenoid BTS couples the beam to the MEG solenoid. A momentum degrader is placed in the solenoid intermediate focus, in order to reduce the muon momentum.

### 3.2.2 Target

The target is placed in the center of the magnet at a slant angle of  $12.3^\circ$ , corresponding to a slant ratio of 1 : 2.5 in a helium atmosphere. For the target material Mylar, Polyethylene, and Kapton, have been investigated from the point of view of multiple scattering and radiation length. The result is summarized in table 3.2.

Material	Density	Radiation Length	Mean Range (28 MeV/c muon)	Target	Degrader
Mylar ( $C_5H_4O_2$ ) <sub>n</sub>	1.39 g/cm <sup>3</sup>	28.7 cm	$\sim 870 \mu\text{m}$	100 $\mu\text{m}$	600 $\mu\text{m}$
Polyethylene ( $CH_2$ ) <sub>n</sub>	0.95 g/cm <sup>3</sup>	47.9 cm	$\sim 1100 \mu\text{m}$	150 $\mu\text{m}$	700 $\mu\text{m}$
Kapton ( $C_2H_4N_2O_5$ ) <sub>n</sub>	1.42 g/cm <sup>3</sup>	28.6 cm	$\sim 1100 \mu\text{m}$	150 $\mu\text{m}$	700 $\mu\text{m}$

Table 3.2: A comparison of the properties of different target types.

A longer radiation length leads to less background in the detector, while a smaller density ensures less multiple scattering in the target. It seems that Polyethylene is the best material from both point of view.



### 3.3 Positron Detector

The positron tracks are measured by drift chambers sitting in an inhomogeneous magnetic field while their timing is determined by timing counters consisting of scintillation bars and fibers.

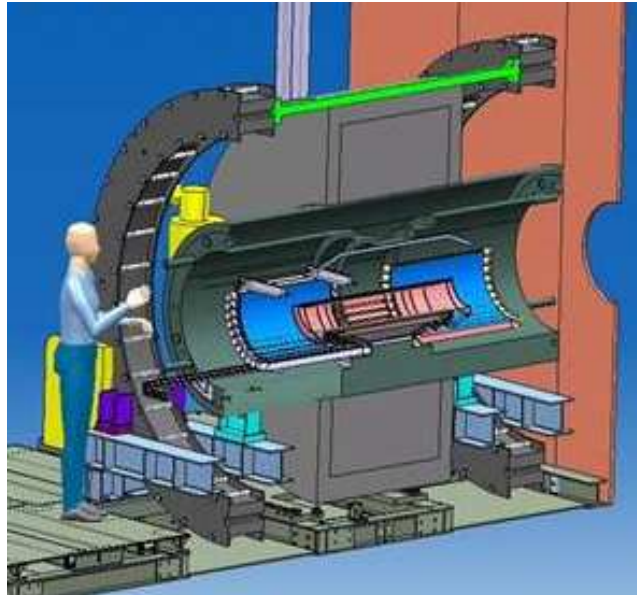
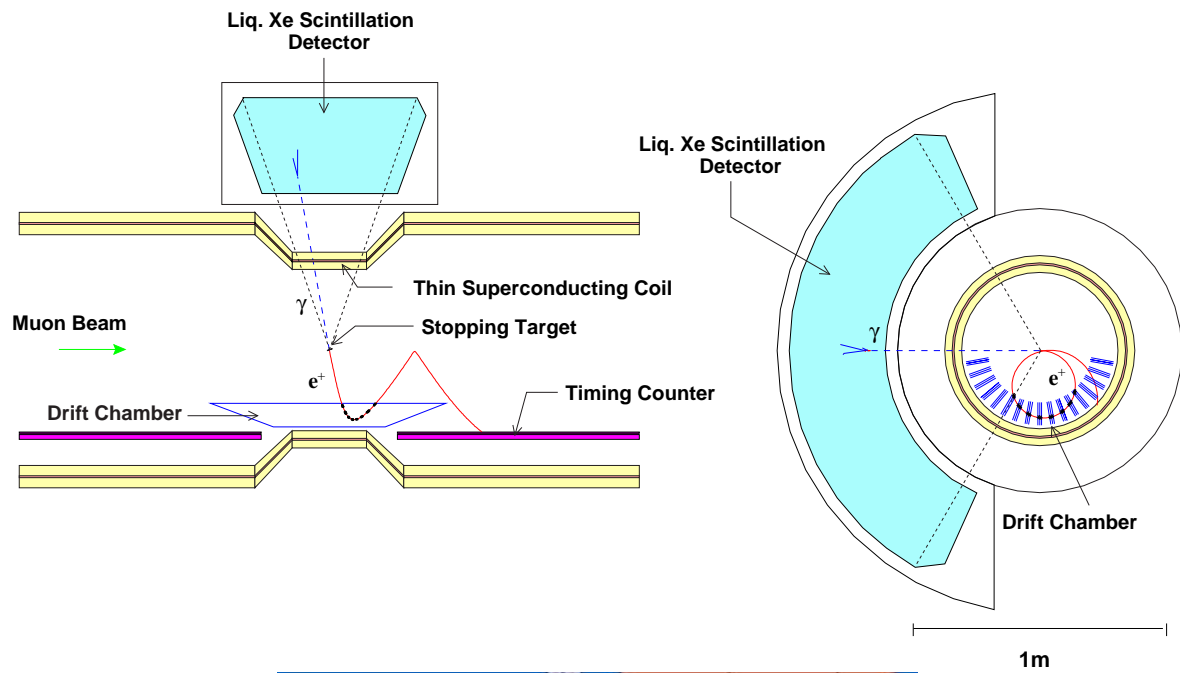


Figure 3.3: The MEG Detector.

As shown in figure 3.3, the target is located at the center of the magnet. The decay positrons spiral out of the magnet hitting the drift chambers which are fixed at the center of the inner wall of the magnet. After crossing the drift chambers the positrons hit one of the two timing counter modules located at both sides of the drift chambers.

### 3.3.1 Magnet

The COBRA (COnstant Bending RAdius) magnet provides a inhomogeneous magnetic field with a peak amplitude of 1.28 T at the center. The advantage of having a inhomogeneous magnetic field is two fold:

- (i) In a homogeneous magnetic field the particles emitted close to  $90^\circ$  with respect to the beam axis will make a lot of turns inside the chambers. This is due to the fact that the component of the momentum parallel to the beam is constant. An inhomogeneous field, however, can be designed such that even particles emitted almost at  $90^\circ$  rapidly sweep out of the detector (see figure 3.4).
- (ii) In a homogeneous magnetic field the bending radius of the particles is proportional to the transverse momentum  $p_t$  of the particle. An inhomogeneous magnetic field can, however, be constructed such that the bending radius depends only on the absolute value of the momentum  $p$  of the particle over a wide angular range. Therefore, the magnet can be designed to force particles with a certain momentum (52.8 MeV/c) to cross the most sensitive region of the drift chambers (see figure 3.5).

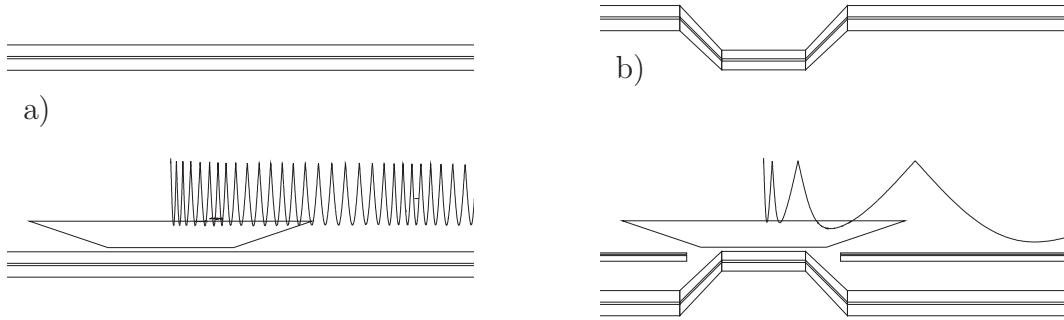


Figure 3.4: r-z views of a) a homogeneous spectrometer and b) the COBRA spectrometer b) are shown with the trajectory of a particle emitted at  $88^\circ$ . The particle is swept away much more quickly in the inhomogeneous field.

To form such an inhomogeneous magnetic field the COBRA magnet is composed of five coils of three different radii: a central coil, two gradient coils and two end coils.

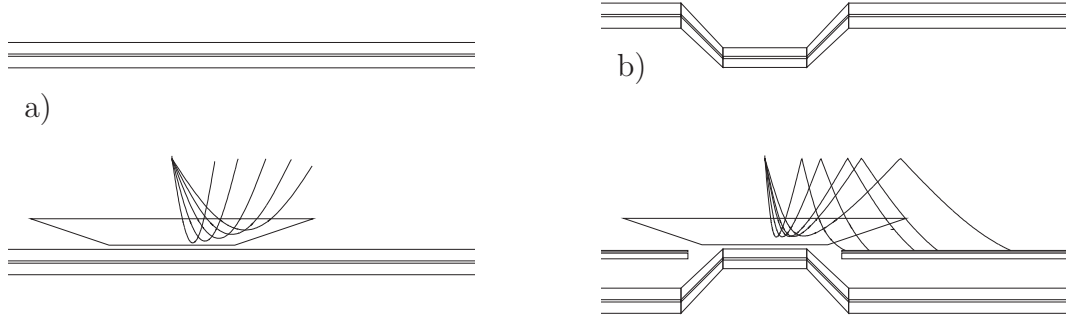


Figure 3.5: r-z views of a) a homogeneous spectrometer and b) the COBRA spectrometer are shown with trajectories of monochromatic particles emitted at various angles. In the COBRA field the bending radius is almost independent of the emission angle.

To reduce the stray field in the calorimeter zone to a level tolerable by the calorimeter photomultipliers, two resistive (i.e. non super-conducting) compensation coils are used. They reduce the field in the calorimeter zone to less than 50 Gauss. The parameters of the super-conducting cable and of the coils are summarized in table 3.3.

Coil	Central	Gradient	Inner end	Outer end	Compensation
Conductivity	Super	Super	Super	Super	Resistive
Inner dia. (mm)	700	810	920	920	2210
Outer dia. (mm)	712.4	820.6	929.5	929.5	2590
Length (mm)	240.3	110.4	189.9	749.2	265
Layers	4	4	3	3	14
Winding	edge-wise	edge-wise (1st) flat-wise (2nd-4th)	flat-wise	flat-wise	double pancake
Inductance(H)	1.64	0.62	0.35	2.29	0.54
$I_{op}$ (A)	360	360	360	360	360
Energy E (kJ)	106	40	23	148	35
Weight M (kg)	9	4	7	28	1620
E/M (kJ/kg)	11.8	10.0	3.3	5.3	0.02

Table 3.3: Parameters of the COBRA magnet

The walls of the magnet are designed to be as transparent as possible to 52.8 MeV photons directing towards the photon detector. The total equivalent thickness of the central part of the magnet is 3.83 g/cm<sup>2</sup> which corresponds to 0.197 radiation lengths. Therefore the conversion probability on the magnet for a 52.8 MeV photon is 18%.

### 3.3.2 Drift Chambers

The positron tracks are measured by a set of 16 trapezoidal drift chambers. The chambers are aligned radially at  $10.5^\circ$  intervals beginning at  $191.25^\circ$  in azimuthal angle and are located in the middle of COBRA (see figure 3.3). The sensitive area of the chambers cover the range from 19.5 cm to 29.5 cm in radial direction from the beam center while in beam direction the range between  $\pm 50$  cm for the innermost wire and  $\pm 22$  cm for the outermost wire is covered (see figure 3.6). Each chamber consist of two planes, 7 mm thick, containing nine drift cells. The wire pitch between the anode wires is 0.9 cm. In between every two anode wires a potential wire is placed (see figure 3.7). One plane is shifted with respect to the other by 0.45 cm in radial direction to solve the left-right ambiguity. The wires are mounted on a carbon fiber frame.

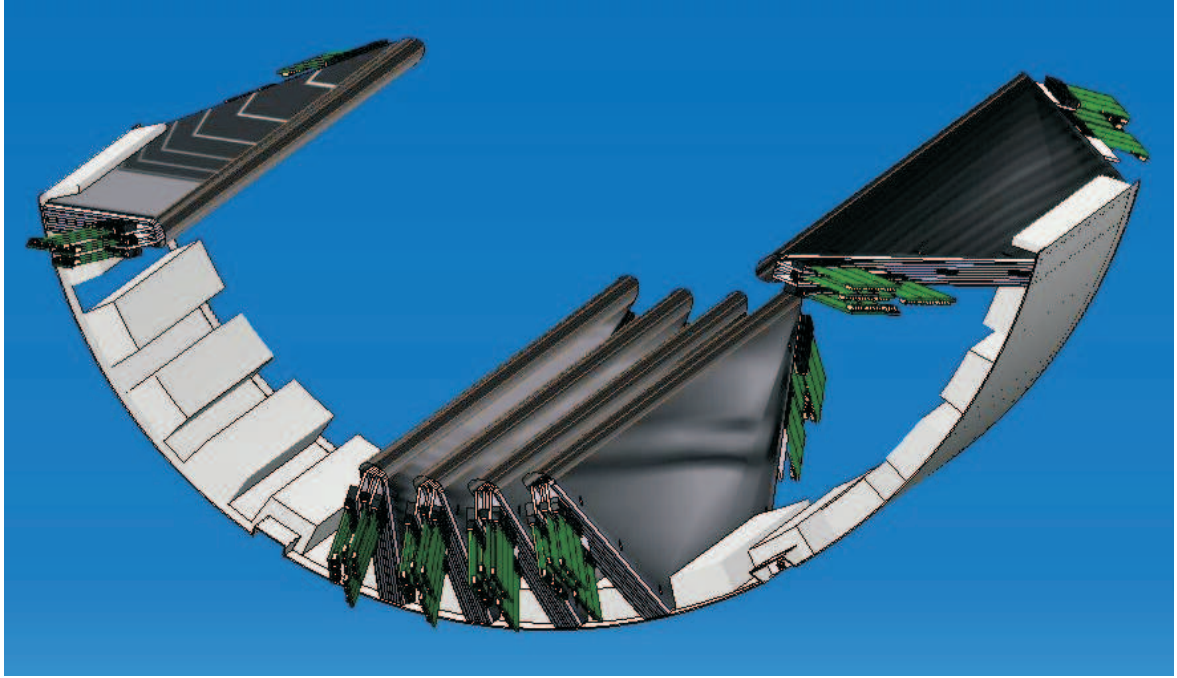


Figure 3.6: An overview of the drift chamber system. Only 6 out of 16 chambers are shown.

The two planes of a chamber are identical and are made out of an extremely thin plastic foil,  $12.5 \mu\text{m}$  thick polyamide, coated with 400 nm aluminium used as a cathode. The plane frame is open towards the detector center allowing to reduce the material in the fiducial tracking volume (see figure 3.8). Therefore, on the inner side, the plane is closed only by the cathode foil. Due to the large reduction of material in crucial tracking volume the overall material amounts to  $0.002 X_0$  on average for the signal positron (52.8 MeV) tracks. The aluminum deposit is shaped on the plane foil to

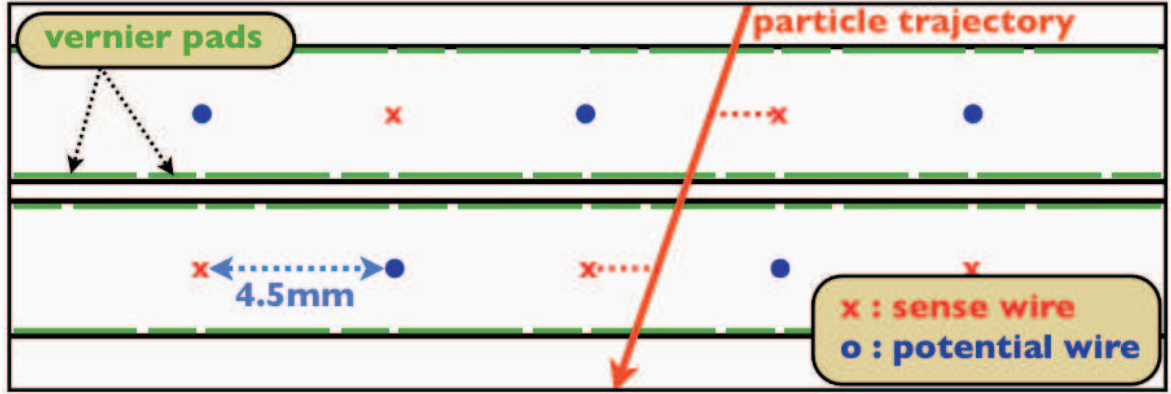


Figure 3.7: The cell configuration of the drift chambers.

form a so-called "Vernier pad" (see figure 3.9). This allows a precise  $z$ -coordinate measurement (see chapter 7.1.5). The pads are read out at one side, while the anode wires are read out at both sides. Out of the charge ratio at both sides of the wire a  $z$  position of the hit can be obtained with an accuracy of about 1 cm. By measuring the charges read out of the cathode strips of both planes, the  $z$  measurement can be improved to  $300\ \mu\text{m}$  resolution [27].



Figure 3.8: The drift chamber frame.

Due to the offset between the two planes of a chamber one obtains a staggered cell configuration. This allows the measurement of the absolute time of a track, by taking the mean time of the two adjacent cells  $(t_1 + t_2)/2$ , with an accuracy of 5 ns. The difference between the measured time of the two adjacent cells  $t_1 - t_2$  gives the radial coordinate of the track with  $200\ \mu\text{m}$  (sigma) accuracy.

The chambers are filled with a helium based gas mixture (50% helium and 50% ethane at 1 atm). The gaps between the chambers are filled with pure helium gas. Ethane is needed to stabilize the chamber behavior and to ensure a sufficient ionization loss in the gas, while helium minimizes the multiple scattering inside the chambers.

Several drift chamber prototypes have been tested at PSI [27] and [28]. Further-

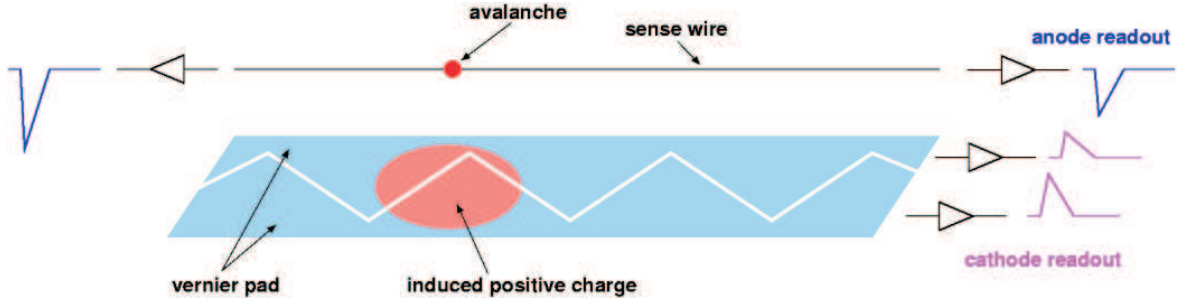


Figure 3.9: A schematical view of the readout signals of a drift chamber cell.

more, the expected resolutions have been studied using a detector Monte Carlo simulation. The expected momentum resolution was determined to be  $\Delta E/E = 0.8\%$  (FWHM), while the expected angular resolution turned out to be  $10.5\text{ mrad}$  (FWHM). The decay vertex on the target is expected to have a  $2.1\text{ mm}$  (FWHM) resolution.

### 3.3.3 Timing Counters

The timing of the decay positron is measured with two timing detectors at both sides of the drift chambers. These detectors are designed to provide the timing of the positrons with a  $100\text{ ps}$  resolution FWHM, at the end of their path through the drift chambers. Furthermore, it provides a fast determination of the positron direction for triggering purposes. The detector is composed out of two layers (see figure 3.10). The outer layer is made of scintillator bars aligned in  $z$  direction measuring the positron timing and  $\phi$  position. The bars are  $5\text{ cm}$  wide,  $2\text{ cm}$  thick and approximately  $90\text{ cm}$  long. They are read out at both sides by photo-multiplier tubes. The inner layer is made of scintillating fibers read out by avalanche photo-diodes (APDs). They are used to measure the  $z$  coordinate. The  $5 \times 5\text{ mm}^2$  fibers are curved and cover the scintillator bars. The two detectors are placed symmetrically at  $25\text{ cm} < |z| < 95\text{ cm}$  and a radius of  $29.5\text{ cm}$ , covering an azimuthal angle of  $145^\circ$ .



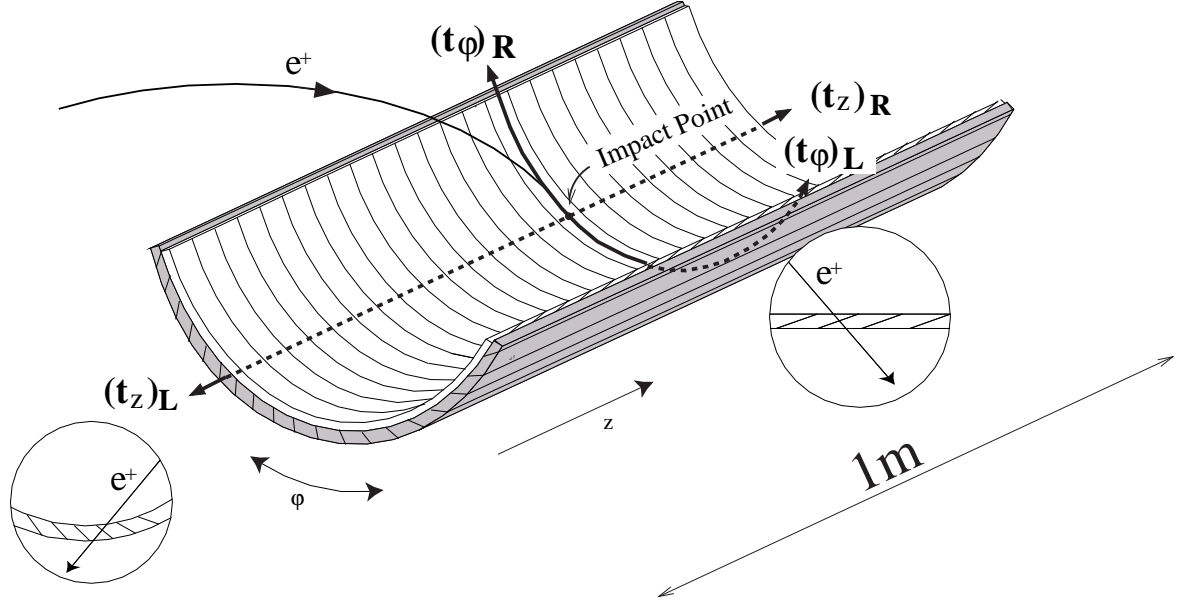


Figure 3.10: The timing counter configuration.

### 3.4 Photon Detector

The photon detector built for the MEG experiment is a  $\sim 0.8 \text{ m}^3$ , C-shaped homogeneous scintillating liquid Xe calorimeter (see figure 3.11). Xe is a rare gas with a large atomic number,  $Z = 54$ , hence short radiation length  $X_0 = \sim 2.7 \text{ cm}$ , which is liquid at 165 K. The MEG calorimeter cryostat is placed just outside the COBRA magnet (see figure 3.3). The detector is read by more than 800 VUV-sensitive PMTs, which one uses to measure energy, direction and timing of the photon. The photon energy and the photon timing is provided by the scintillation light collected by all PMTs, while the photon direction is extracted from the light distribution on the calorimeter front face.

The design goal of the LXe detector is the following:

- Time resolution:  $\Delta t = 100 \text{ psec}$  (FWHM).
- Position resolution:  $\Delta x = \Delta y = 2 \text{ mm}$ ,  $\Delta r = 7 \text{ mm}$  (FWHM).
- Energy resolution:  $\Delta E = 4.5\%$  (FWHM).

It is currently the largest LXe scintillation detector which has ever been built.

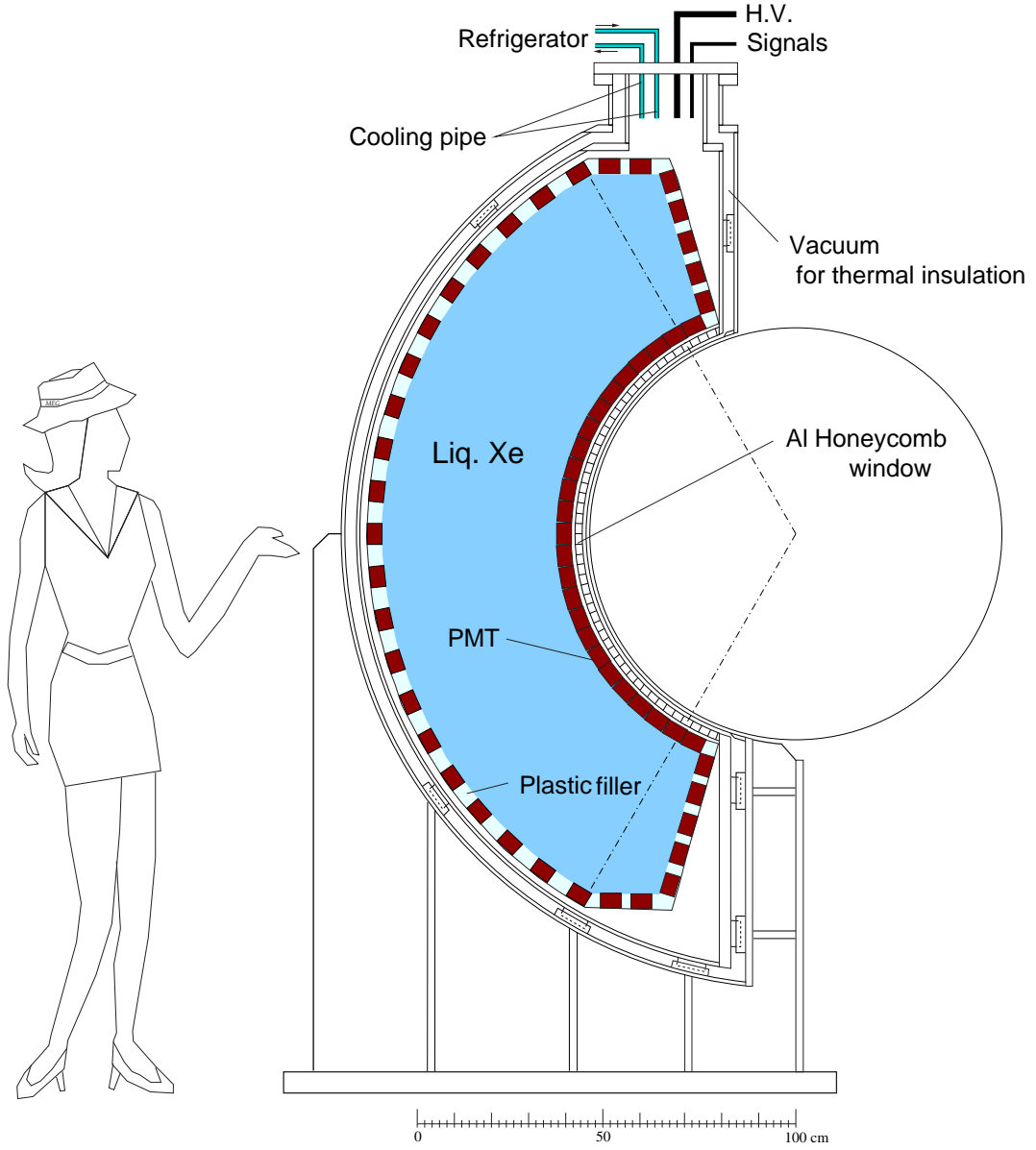


Figure 3.11: The liquid xenon detector.

## 3.5 Trigger and DAQ

### 3.5.1 Trigger

The trigger must be sensitive to a back-to-back photon-positron pairs coincident in time, each having an energy of half of the muon mass. The trigger uses information coming from the liquid Xe detector and the timing counter. The information from



the drift chambers is too slow due to the relatively long electron drift time inside the chambers. The trigger system is capable to digitize the input with 100 MHz sampling rate. This is needed to perform an on-line subtraction of the pedestal and rejection of the common noise. The waveforms are then used to perform a basic event reconstruction to improve the quality of the trigger decision. The hardware is hosted on VME boards and equipped with Field Programmable Gate Arrays (FPGAs).

### 3.5.2 DAQ

The signals from all three detectors, liquid Xe calorimeter, drift chambers and timing counters, are digitized by a custom chip, called Domino Ring Sampling Chip (see chapter 4). The DRS chip performs a signal sampling of 1024 samples with a rate between 0.5 to 5 GHz. The sampled signal is stored inside the domino cells and read out with 30 MHz. This method constitutes a sort of analog pipeline which eliminates the use of delay cables. The waveform digitizing allows for an advanced pile-up and noise suppression. On the other hand the amount of data is large ( $\sim 9$  Mb per event), which requires an online data reduction.

The VME crates hosting the trigger and the DRS boards are read out by 9 online computers running the MIDAS system [29]. This system performs the read out and the data reduction of the event as well as combining the event fragments coming from the different online computers and the logging of the data. The online analysis of the data and the online event display are based on the ROME system, which will be discussed in chapter 5.



# Chapter 4

## The Domino Ring Sampling Chip

### 4.1 Introduction

The Domino Ring Sampler (DRS) is a high resolution analog signal sampling chip. The first version of this chip was developed by Stefan Ritt in 2001 at PSI. The used technology was refined in a second version of that chip (DRS2) [30]. This chapter describes the performance measurements of that second version of the chip. The insights obtained by this work lead to a third version of this chip. The DRS3 chip did already proof to solve some issues of the DRS2.

The DRS2 chip contains 1024 capacitive sampling cells fabricated in a  $0.25\ \mu\text{m}$  CMOS process. The sampling frequency is generated on the chip itself and ranges from 0.5 to 4 GHz. The cells are read out at 30 MHz with an external 12 bit flash analog-to-digital converter (ADC). The chip contains 8 input channels with a voltage limit of 2 Volts.

The sampler consists of two sections, an analog one for the signal sampling and a digital for control and multiplexing. The analog signal is stored in a switched capacitor array (SCA) with 1024 cells that is organized as a ring buffer, in which the single capacitors are sequentially enabled by an inverter chain (see figure 4.1), producing a so called Domino wave. The speed of the domino wave is controlled by an external voltage such that the domino inverters can be seen as a Voltage Controlled Oscillator (VCO). Every turn a pulse is produced for synchronization and monitoring. The phase and speed of the domino wave are synchronized to an external common reference clock by an on-board Phase-locked loop (PLL), designed around the domino VCO. The chip is housed in a Plastic Leaded Chip Carrier (PLCC) package and mounted on a mezzanine card, also called CRAB (Capacitor Ring Analog Board). Once the external trigger has been received, the sampled signal is frozen in the SCA and read out in a shift register followed by a multiplexer and digitized at high resolution (12 bits) at lower frequency (30 MHz) with an external ADC. The transfer curve of the output stage is typical of

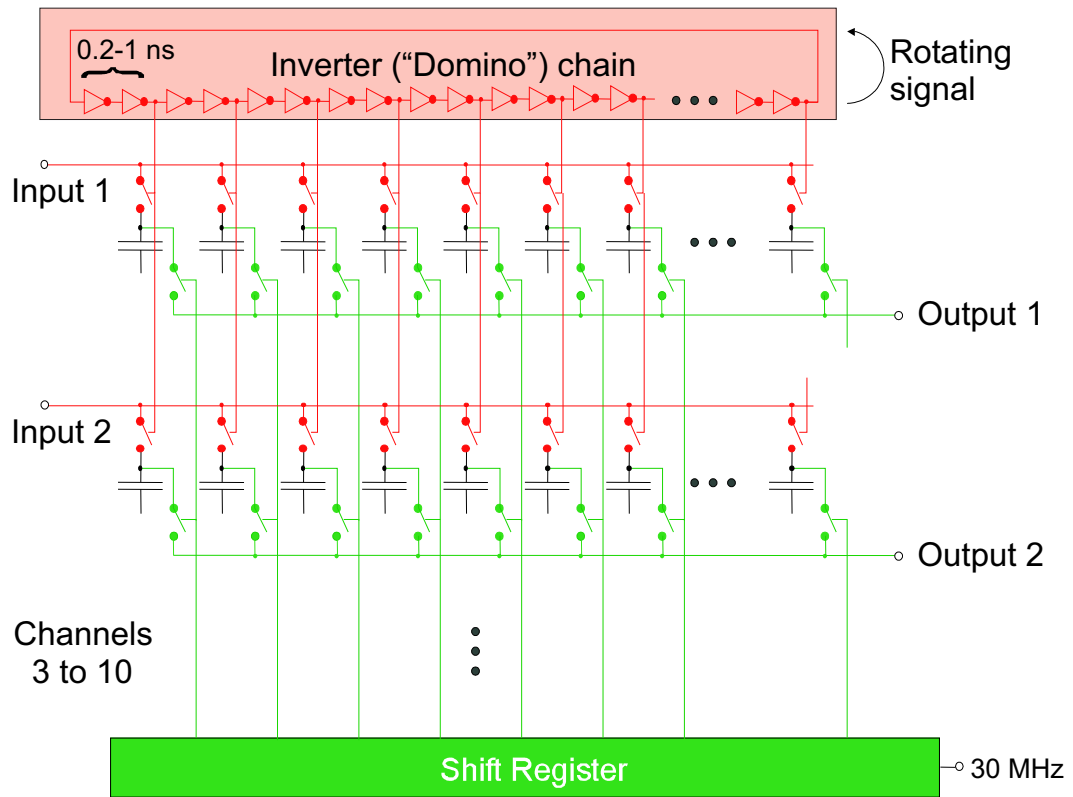


Figure 4.1: Schematic picture of the Domino sampler. Shown on top is the inverters sequence that originates the Domino wave. The shift register on the bottom enables serially the single capacitors connecting them to the output stage.

a Metall-Oxid-Semiconductor (MOS) transistor, with an active region quite linear up to 500 mV, that tends to saturate for larger signals.

## 4.2 Temperature Dependence

When the DRS2 is heated up the response function changes as shown in figure 4.2. This is due to the fact that the current passing through the individual transistors in the domino cells is temperature dependent

$$I = c_1 V_{in} + c_2 V_{in} kT. \quad (4.1)$$

This issue can be solved by replacing the transistor (see figure 4.3) by a differential pair of transistors (see figure 4.4) which was implemented in DRS3.

The problem not only arises when the chip is heated externally, it also appears when the chip is triggered with a different trigger frequency as the one used to calibrate the chip. This is due to the fact that the DRS2 cells warm up during the read out. The change of the voltage level is rather uniform among the DRS2 cells, except for the last 64 cells. These cells show a much larger dependence on the trigger frequency as the others. This results in fake square pulses on the waveform (see figure 4.5), which may happen to lie under a signal peak and fake the charge measurement.

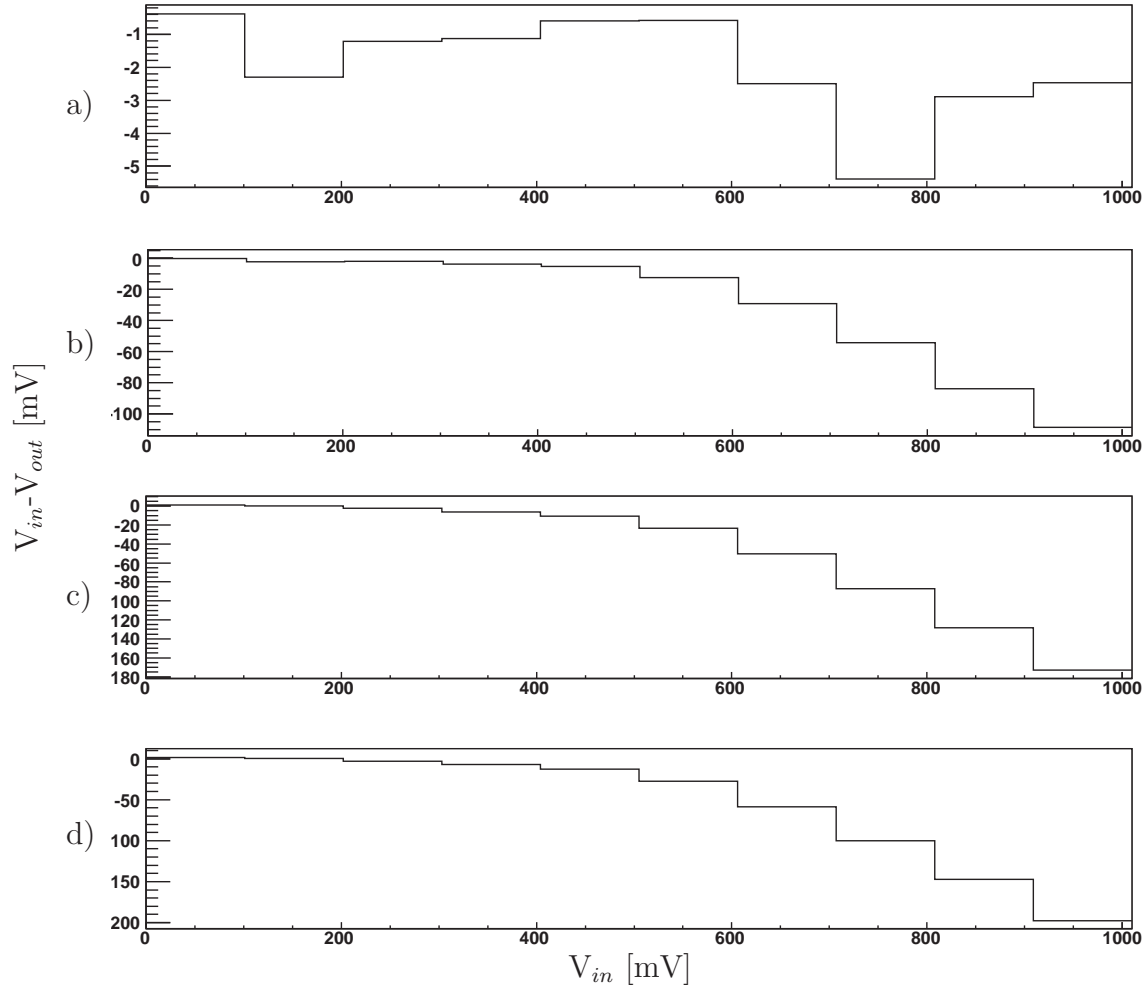


Figure 4.2: The input voltage minus the output voltage as a function of the input voltage is shown for a) 27° b) 32° c) 38° d) 42° Celsius. The chip was heated up with a heat gun and the temperature was measured with a portable sensor on the surface of the chip. The temperature at the domino chain inside the chip differs probably slightly from the measured values.

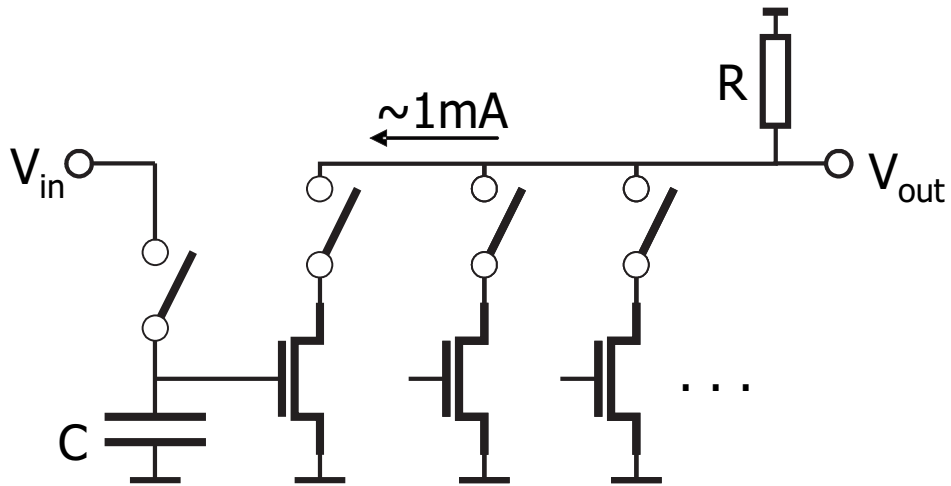


Figure 4.3: Schematic view of the DRS2 domino cell.

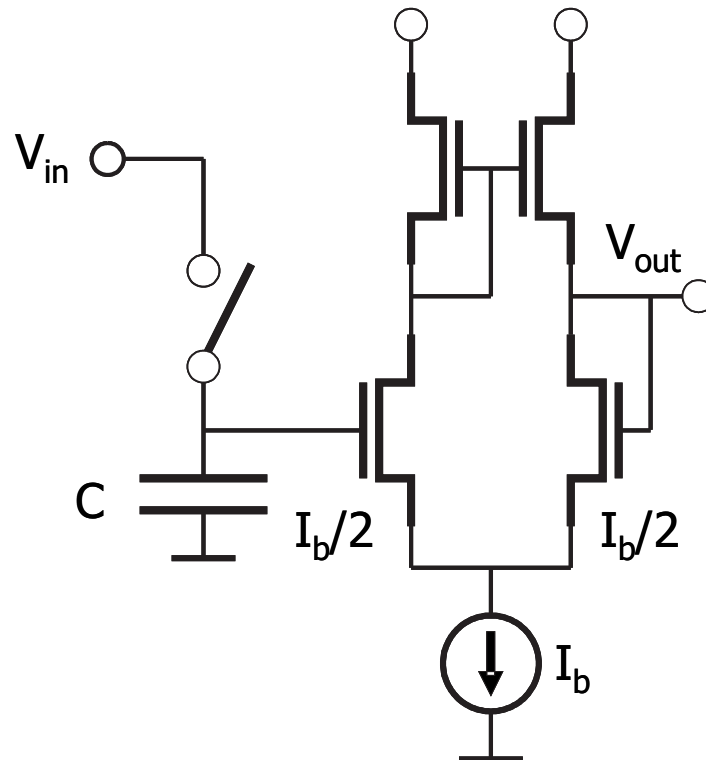


Figure 4.4: Schematic view of the DRS3 domino cell.

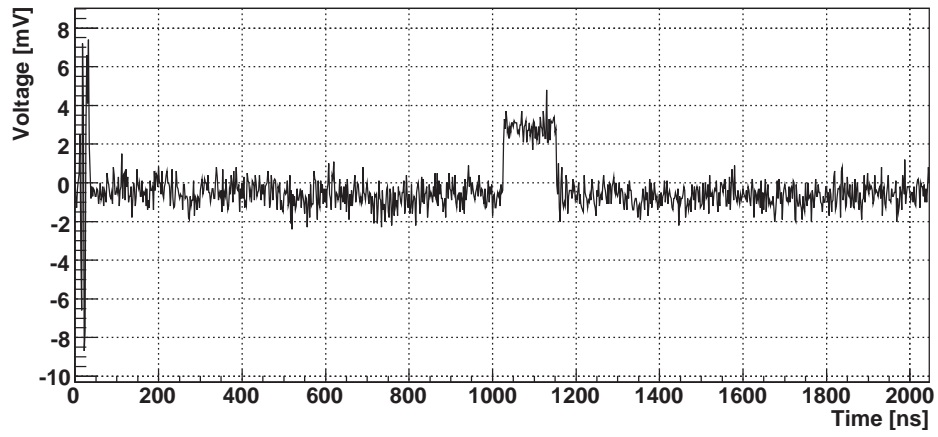


Figure 4.5: A fake pulse created by the last 64 cells of the DRS2 chip. Note that this waveform has been rotated and that the sampling frequency is 0.5 GHz.



## 4.3 DRS2 Calibrations

The DRS2 needs three types of calibrations.

- *The response calibration*

The response function of the DRS2, which is the output voltage as a function of the input voltage, is nonlinear. The nonlinearity is different in all sampling cells of all channels.

- *The offset calibration*

The output of the domino chip depends on the readout frequency (see 4.2). For this reason, the faster readout speed during the response calibration compared to the nominal experiment trigger frequency has to be compensated. This is done in the offset calibration.

- *The time calibration*

The speed of the domino wave is not constant in one cycle. The reason is that the speed depends on the exact size of the transistors used in the domino chain. Apparently these transistors differ slightly. This effect leads to a deviation of the sampling frequency of up to 16%.

### 4.3.1 Response Calibration

The output of the DRS2 is measured in ADC counts. The ADC counts as a function of the input voltage, are linear up to 0.5 V and go then into saturation. This function, shown in figure 4.6, is called the response curve. This behaviour is typical for a MOS transistor used inside the domino cell.

To determine the input voltage of the DRS2 chip from the ADC counts, the response of the DRS2 must be calibrated. To create the calibration parameters a constant input voltage is applied to the input channels. The voltage is then increased stepwise to record 36 calibration points from 0 V up to 0.8 V. These points are then fitted by a fourth order B-spline function of degree 19. The grid points of the B-spline are then written to a calibration file. The B-spline has equally spaced grid points in the x direction, so that the spline can be used as a function of x to get the y value. This way the total amount of values to store is about 250'000 per chip leading to about 0.5 Gigabyte of data. Table 4.1 shows the maximal error of the calibration in all bins of all channels of a chip for different input voltages. Due to the exponential rise of the response curve the uncertainty of the calibration points becomes worse above 500 mV.

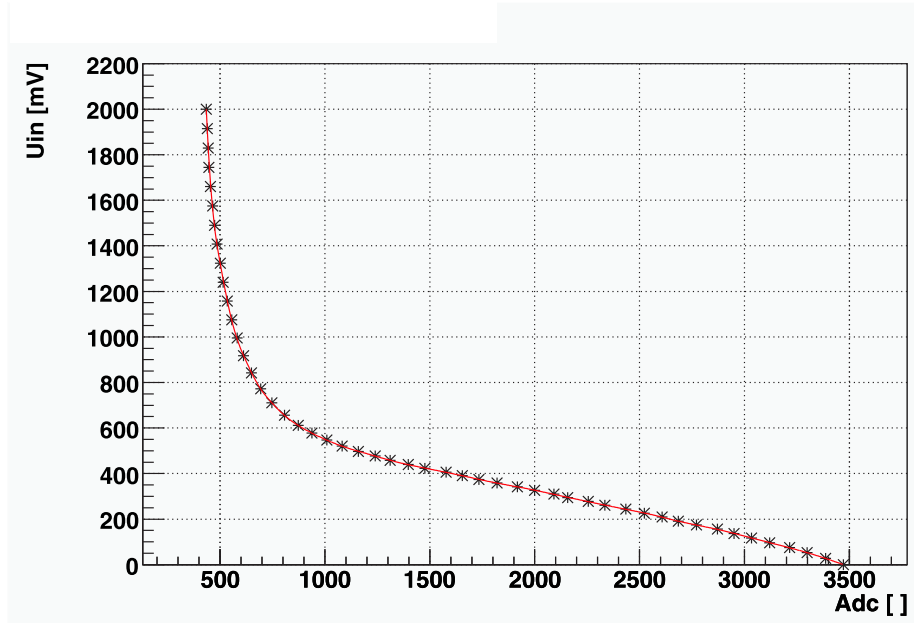


Figure 4.6: The input voltage as a function of the ADC counts.

Input Voltage [V]	Calibration Error [mV]
0.05	< 0.03
0.15	< 0.01
0.24	< 0.04
0.33	< 0.04
0.41	< 0.02
0.50	< 0.05
0.67	< 0.15

Table 4.1: The error of the response calibration for different input voltages.

### 4.3.2 Offset Calibration

The response calibration is done with the fastest readout speed possible. Therefore, it is only applicable if the chip is readout at the same speed, since the output of the domino chip is dependent on the readout frequency (see 4.2). To calibrate the chip for a slower readout frequency an offset calibration is performed. The chip output is sampled with no input signal applied. The difference of the output waveform to the base is then stored as an offset calibration. In this procedure we neglect the voltage dependence of this effect. But since the temperature dependence of the trigger frequency is relatively small it gives reasonable results.

### 4.3.3 Time Calibration

The domino wave travels through the 1024 domino cells with an internally generated sampling frequency. This is achieved by transistors used as tunable resistors in each cell. However, due to inhomogeneities in the manufacturing process the size of the transistor vary from cell to cell. Therefore, the speed of the domino wave depends on the position of the transistor on the chip. The domino wave travels for example slower in the first half of the domino chain and faster in the second half of the domino chain compared to the nominal value (see figure 4.7). There is also a cell to cell variation of 80 ps RMS at 2 GHz sampling frequency (see figure 4.8). Since this effect is constant it can be compensated for by a time calibration.

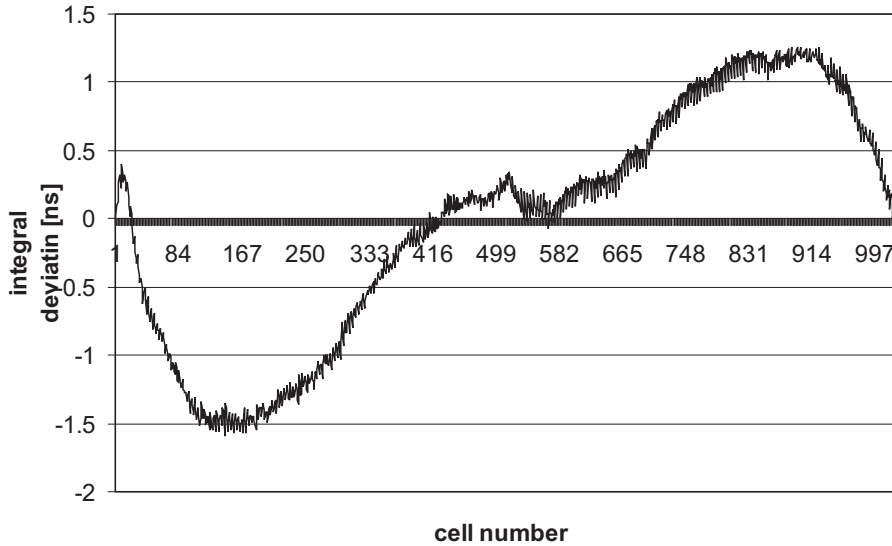


Figure 4.7: The integral deviation of the domino speed for one turn.

For the calibration of the domino speed a sine wave from a function generator is used. The function generator is triggered simultaneously with the chip. The Domino wave will then run for one cycle and then stop. With this configuration the phase of the sinus wave inside the DRS2 window is fixed. The first period of the recorded signal is then fitted with a sinus function. Subsequently, the time difference of all recorded points to the fitted sine wave  $\Delta t_i$  are calculated (see figure 4.9). Finally, the time corrections of each cell  $\Delta t_i^c = \Delta t_{i-1} - \Delta t_i$  are calculated and stored in a calibration table.

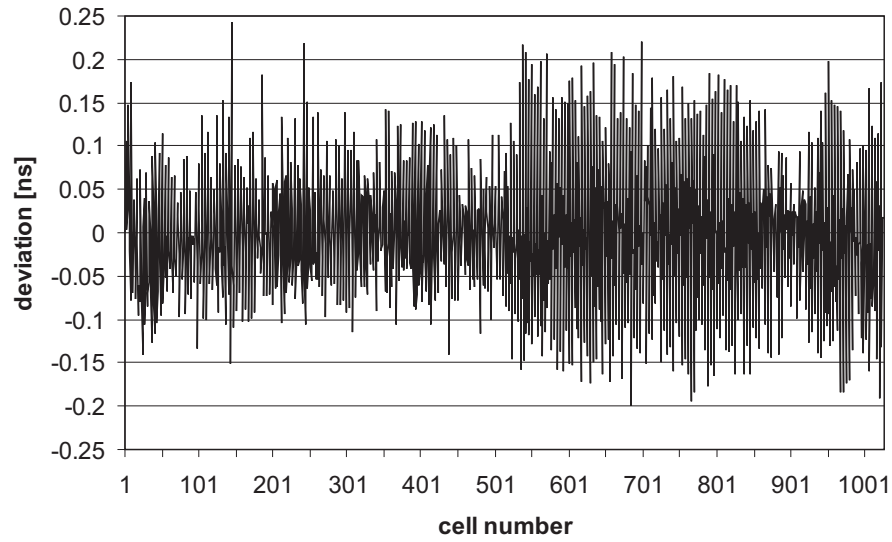


Figure 4.8: The cell to cell deviation of the domino speed.

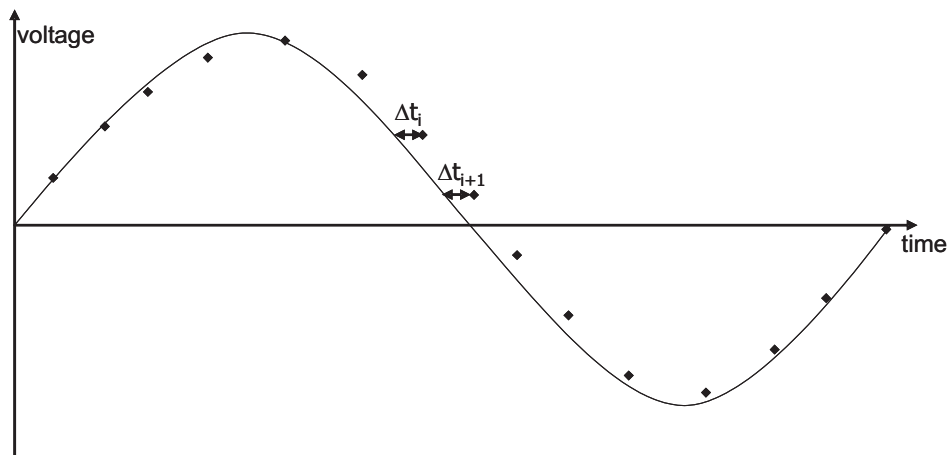


Figure 4.9: Illustration of the time calibration. The diamonds point are the recorded sine wave. The solid line the nominal (fitted) sine curve.

## 4.4 Synchronization of chips

While the time calibration corrects for variations of the Domino speed inside the chip, different chips can run at slightly different sampling speeds. To account for this effect a reference clock signal is sampled in a specially assigned additional input channel. The edges of the this reference clock signal can then be matched to determine the exact phase of the Domino wave at the trigger time. Figure 4.10 shows a sampled rectangular clock signal of 30 MHz. The signal is pretty distorted, which will be improved in the DRS3 by rearranging the signal line of the clock signal on the chip and improving the signal coupling.

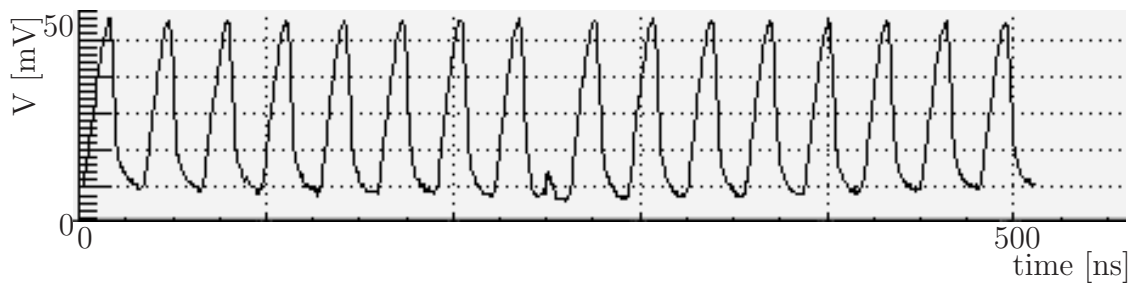


Figure 4.10: The clock signal sampled with 2 GHz.

## 4.5 DRS2 Measurements

### 4.5.1 Cluster Points in the voltage response

The first mezzanine board hosting the DRS2 chip had the wire configuration shown in figure 4.11. The wire of the domino tap signal crosses the input channel wires. The domino tap signal is a rectangular signal and introduces therefore two cluster points on the input signal. The consequence of which is that if the ADC output of the DRS2 for a given input voltage is sampled, the histogram shows two peaks as shown in figure 4.12. This behavior could be successfully eliminated by a redesign of the mezzanine board.

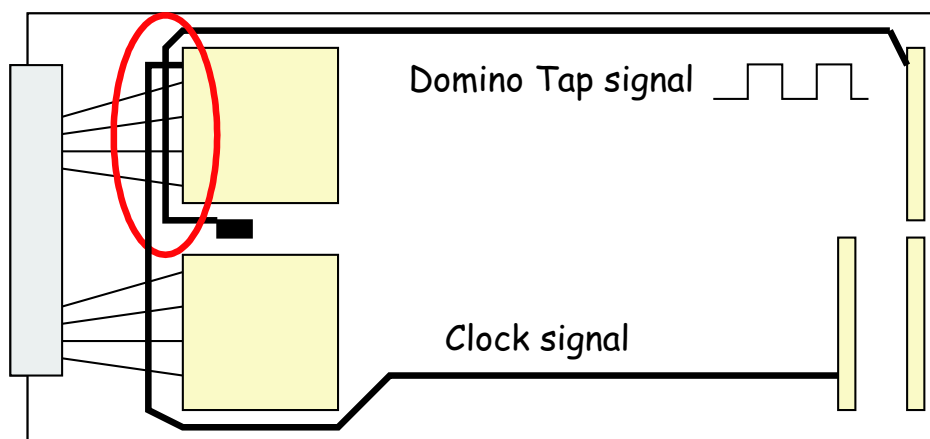


Figure 4.11: The domino tap signal wire crosses the input channel wires on the mezzanine board. The crosstalk leads to two cluster points for the signal.

### 4.5.2 Cross Talk

The cross talk of an input channel on the other input channels was measured. The input signal is shown in figure 4.13. It has a rise time of 2 ns and a height of 0.1 V. The signal of the first neighbor channel is shown in figure 4.14. Table 4.2 summarizes the obtained values.

This measurement includes cross talk which may be picked up inside the chip itself, but also cross talk picked up on the mezzanine board or the connectors. Improving the layout of the mezzanine board and replacing the connector by a connector with better characteristics regarding cross talk may help to improve the situation.

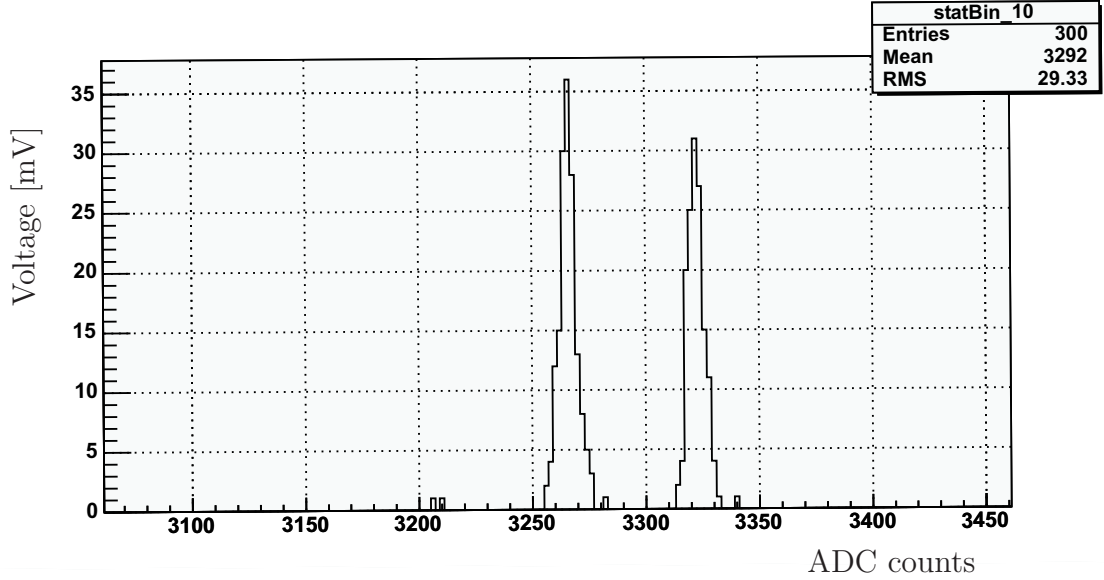


Figure 4.12: Cluster Points in the voltage response.

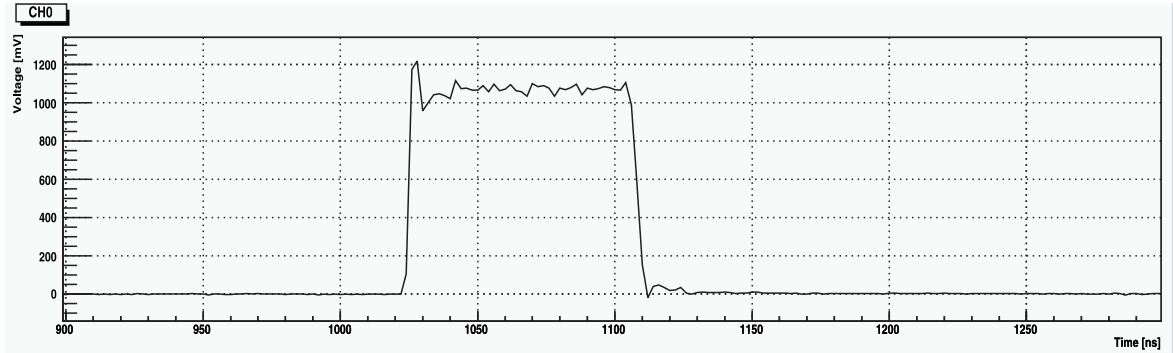


Figure 4.13: Signal used for the cross talk measurement.

### 4.5.3 Ghost Pulses

Before sampling a new waveform the capacitors of the domino chain have to be discharged. This process has a typical exponential behavior and is very fast. The problem is that in the DRS2 the charge of all cells flow out through the input channel lines. This has the effect that when the second cell starts to discharge, the first cell still contains a rest charge. Due to the resistivity of the input line, the charge can not flow out of the cells as fast as needed to discharge the capacitors completely. Therefore, a rest charge always stays in the domino cells, resulting in a so called ghost pulse in the next sampling turn. This behavior is shown in figure 4.15.

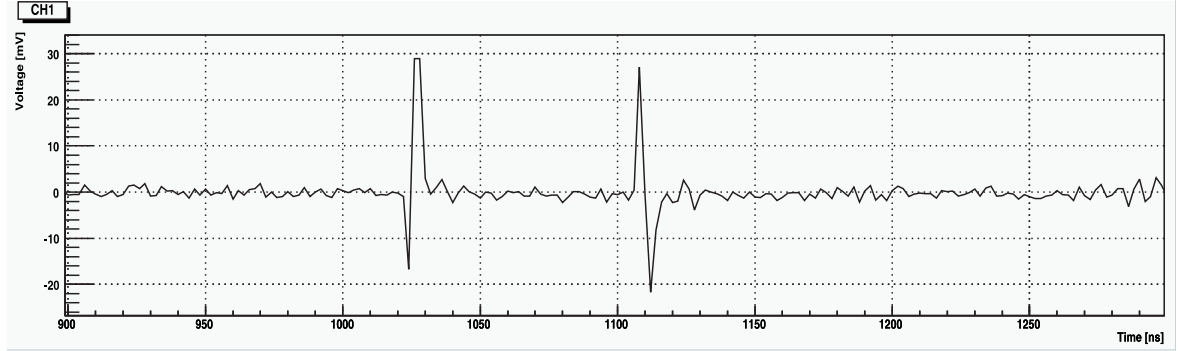


Figure 4.14: First neighbor signal obtained in the cross talk measurement.

Channel	Cross-Talk
$0 \rightarrow 1$	2.9%
$0 \rightarrow 2$	1.7%
$0 \rightarrow 3$	1.6%
$0 \rightarrow 4$	1.2%
$0 \rightarrow 5$	1.0%

Table 4.2: Cross talk measurements on the DRS2 boards. The Cross-Talk of channel 0 on the neighbor channels is quoted.

This problem will be solved in the next generation of the chip by discharging the capacitors directly to ground before each sampling.

#### 4.5.4 Band width

The bandwidth of the DRS2 was measured by applying sine waves with varying frequencies to the chip. The result is shown in figure 4.16. The bandwidth turned out to be 150 MHz (-3db point). The measurement was performed by applying the signal to the standard connector of the DRS mezzanine board, therefore the limiting component could be on the board and not in the chip itself.

#### 4.5.5 Time- and Charge Resolution

The time- and the charge resolution of the DRS2 were measured and compared to the resolutions of a digital oscilloscope and to the resolutions of ADC and time to digital converter (TDC) devices.



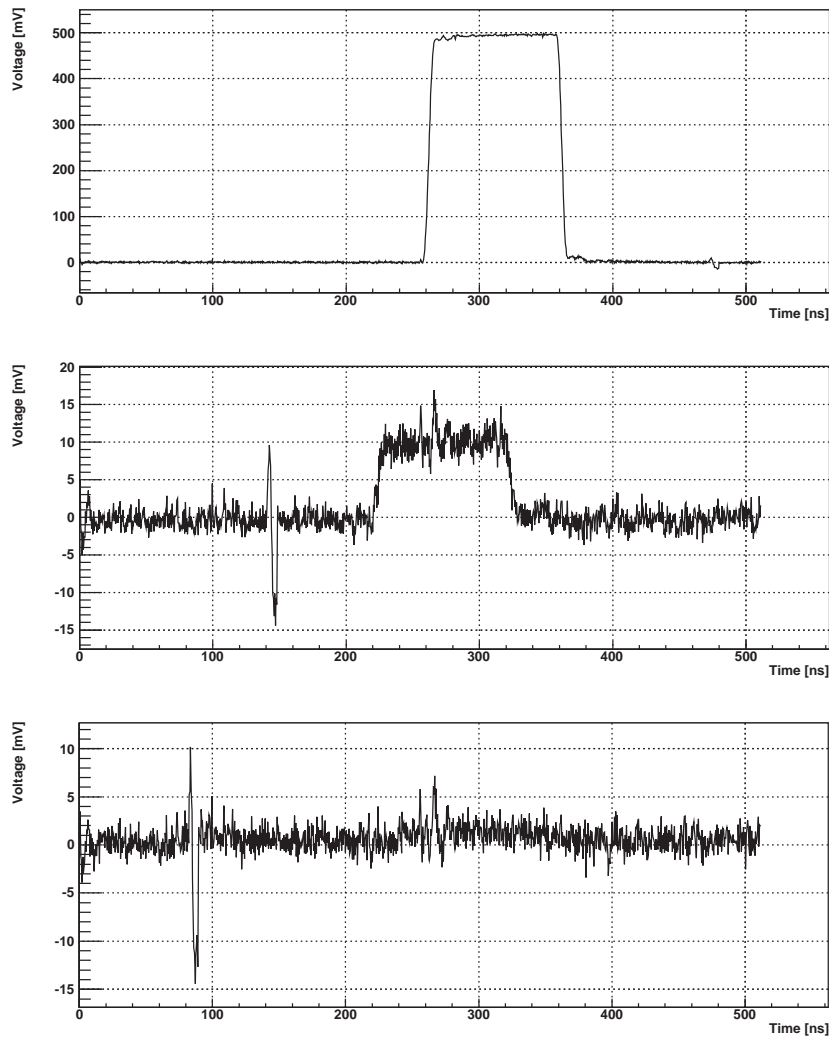


Figure 4.15: The first picture shows a square pulse sampled by the DRS2 chip. The second picture shows the sampled waveform one domino cycle after the square pulse. There is still a rest charge on the capacitors resulting in a "ghost" pulse in the order of 2 % of the height of the original pulse. The third picture shows the sampled waveform two domino cycle after the square pulse.

### Signal Fitting

The start time of a signal can be calculated by fitting the rising edge of the signal with a first order polygon or fitting the signal or part of the signal with a template of the signal. The second method leads to far better results. Especially if the rise time is fast compared to the sampling frequency (only few points on the slope). Of course

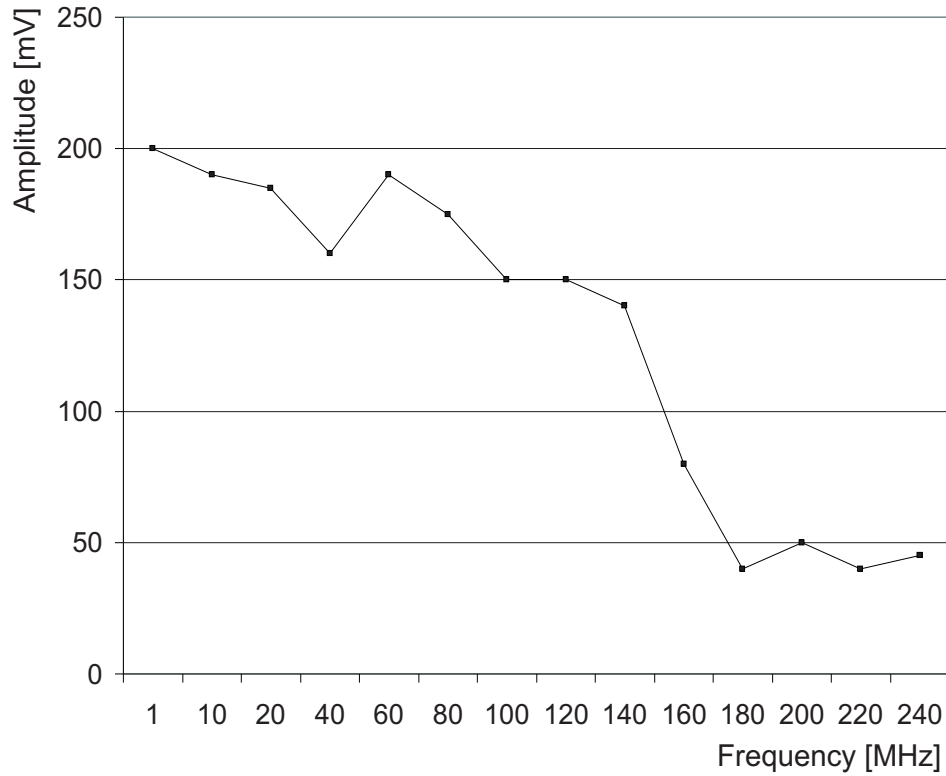


Figure 4.16: Bandwidth of the DRS2 chip.

the template fit can only be applied when the shape of the signal is constant enough to record a template of the signal. The values in table 4.3 have been obtained with a distorted rectangular signal with a rise time of 8 ns (see figure 4.17).

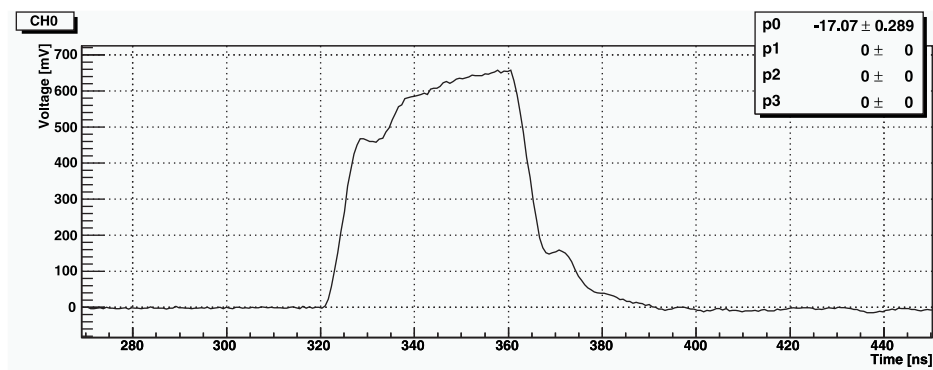


Figure 4.17: Distorted pulse generator signal.

The linear fit calculates a first order polygon through points on the slop of the signal starting with the first point above a certain threshold and ending with the point

where the gradient is less then three-fourths of the maximum gradient of the previous points.

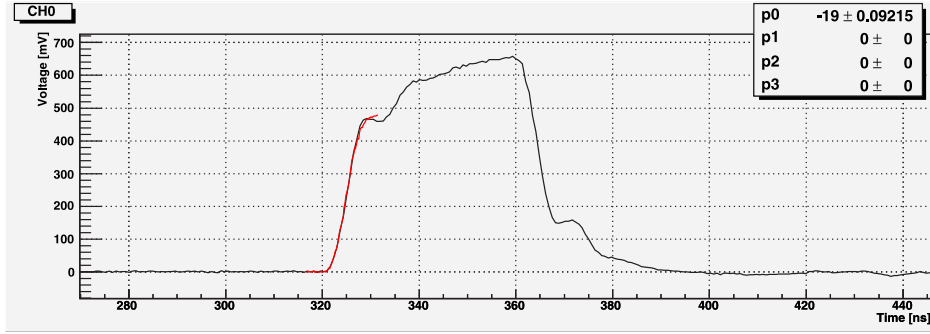


Figure 4.18: Distorted pulse generator signal fitted with a template.

The template consists of 70 points with a time resolution of 0.2 ns. A fitted template is shown in figure 4.18. Since a time calibrated signal doesn't have constant time steps anymore, the time resolution of the template can be much higher then the one of the signal itself (see section 8.3).

Freq.	template fit [ns]	linear fit [ns]
0.5 GHz	$0.110 \pm 0.011$	$0.314 \pm 0.057$
1.0 GHz	$0.051 \pm 0.008$	$0.185 \pm 0.021$
1.5 GHz	$0.028 \pm 0.003$	$0.087 \pm 0.011$
2.0 GHz	$0.027 \pm 0.002$	$0.076 \pm 0.009$
2.5 GHz	$0.023 \pm 0.001$	$0.066 \pm 0.006$

Table 4.3: The time resolution of the domino chip is given for two different methods of determining the start time of the signal, a linear fit and template fit.

## Setup

The signal coming from a pulse generator is split eight times. Two of the split signals go into the DRS2, two into the oscilloscope, two into the ADC and two into the TDC. One of each of the two signals is delayed by a delay cable (see figure 4.19).

## Results

The time resolution was measured by sampling the time difference of two signals. One of them was delayed by 16 ns. A sample of a signal coming from a pulse generator and distorted by the electronics is shown in figure 4.17. The signal has a rise time of 5 ns and an area of 24 Vns. The sampling rate of the DRS2 was varied from 0.5 to

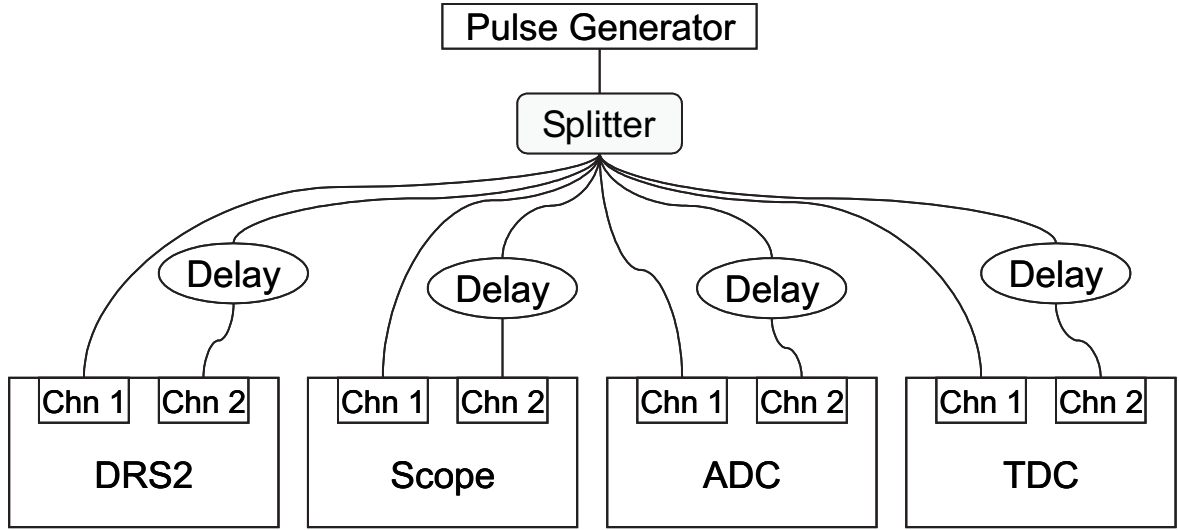


Figure 4.19: Setup for the time and charge resolution measurements.

2.5 GHz. The maximal sampling frequency of the scope is 1 GHz. However, it can run with a higher resolution in the so called Random Interleaved Sampling (RIS) mode. Therefore, there is also an entry for 2.5 GHz in the table 4.4 and 4.5. The minimal sampling time step of the TDC is 50 ps. The resolution of the ADC is 0.025 Vns.

**Time Resolution** Table 4.4 shows the results off the timing measurements of the different devices. The values obtained by the three detectors agree with each other. From the TDC measurement one can see the the time jitter of the two signals is smaller then 50 ps. The best time resolution provides the DRS2 when running with a high sampling rate. However, the results of the DRS2 are worse than the ones form the scope and from the TDC for a low sampling frequency.

Freq.	$\Delta t$ [ns]		
	DRS	Scope	TDC
0.5 GHz	$0.287 \pm 0.043$	$0.112 \pm 0.012$	$< 0.050$
1.0 GHz	$0.073 \pm 0.009$	$0.074 \pm 0.004$	-
1.5 GHz	$0.053 \pm 0.007$	-	-
2.0 GHz	$0.033 \pm 0.003$	-	-
2.5 GHz	$0.032 \pm 0.004$	$0.058 \pm 0.004$	-

Table 4.4: The time resolution of two split signals measured with the DRS2, the scope and a TDC.

**Charge Resolution** The charge resolution of the three different devices is shown in table 4.5. The resolution of the domino chip is worse than the resolutions of the two other devices. The domino chip resolution is limited by the temperature dependence problem, which affects the voltage calibration and the offset calibration. The main part of the jitter in the charge comes from the fact that we neglect the voltage dependence during the offset calibration.

Freq.	$\Delta Q$ [Vns]		
	DRS	Scope	ADC
0.5 GHz	$0.442 \pm 0.075$	$0.127 \pm 0.009$	$0.046 \pm 0.013$
1.0 GHz	$0.232 \pm 0.036$	$0.108 \pm 0.008$	-
1.5 GHz	$0.213 \pm 0.035$	-	-
2.0 GHz	$0.237 \pm 0.046$	-	-
2.5 GHz	$0.206 \pm 0.014$	$0.159 \pm 0.012$	-

Table 4.5: The charge resolution of two split signals measured with the DRS2 the scope and an ADC.



# Chapter 5

## Analysis Framework

In this chapter we will present the analysis framework, which is used to analyze the data, read out by the MEG detector. The framework is used both for the on-line and the off-line analysis.

### 5.1 Introduction

Analysis frameworks<sup>1</sup> for particle physics experiments are typically custom built. This is due to the fact that the experiments can differ significantly from each other. Obviously building special frameworks for each experiment requires significant man power. In the section 5.2 we describe a way of generalizing analysis frameworks, based on the idea of not writing the framework code by hand but, by letting it be generated by a translation tool that transforms an experiment description into code. The translation tool can be written completely experiment independent and hence can be used for every event based data analysis. This approach saves a lot of man power since the translation tool has only to be written once and can be used for any experiment. Moreover, it also leads to optimized analysis frameworks since all experiments using the translation tool can contribute improving it.

In the section 5.3 we present such a translation tool which comes under the acronym ROME and stands for **R**oot based **O**bject oriented **M**idas **E**xtension. It was developed at PSI, Switzerland and is currently used by the MEG experiment at PSI, the DANCE experiment at the Los Alamos Laboratory and is under test by other experiments. We explain the implementation of the generation process in ROME, which is a translation of an experiment description specified in XML files to C++ classes.

---

<sup>1</sup>It is important to distinguish between the term analysis framework and the term analysis software. In this thesis we mean with analysis software a final software for analyzing experimental data. Analysis framework means a framework for writing an analysis software, that means it refers to all code except the analysis code.

Furthermore, features such as connection to DAQ systems, database access, socket connection, Graphical User Interface (GUI) extension and modularity are also discussed.



## 5.2 Generating Analysis Frameworks

An analysis software can be divided into two parts. The framework code and the analysis code. The framework code includes the whole structure of the analysis, e.g. the program flow, I/O, the data structure, the task structure etc. The remainder of an analysis software is the analysis code itself, which is the calculation code performed on the data.

The framework code can further be divided into two parts, a part which can be implemented completely in an experiment independent way and a part which is experiment dependent. The former independent part includes mainly the event loop and basic functionality of a framework. The rest of the code is experiment dependent. This experiment dependent code, however, can be summarized in an experiment description, from which the program code can be generated by a translation tool. The analysis code, however, can in general not be simplified and has to be implemented as code by the experimenter.

Therefore, we divide the analysis software into three parts (experiment independent framework, experiment dependent framework and analysis). The amount of code needed for these parts strongly depends on the size of the final program. The experiment independent part is fixed and will vary up to 60% for a very simple analysis and will decrease to a small fraction for a complex one. The other two parts have more or less the same size and both grow with the size of the experiment. The important fact to notice is that they grow at more or less the same rate. Therefore, the generated part of the analysis software will always be of a similar size to that of the analysis code, regardless of the size of the final analysis software. This means that about half of each analysis software can in principle be generated.

### 5.2.1 Benefits of a generated framework

Generating an analysis framework has several advantages, which are discussed in this section.

#### **Saves Manpower**

As we pointed out before the generation of frameworks saves a lot of man power. The translation tool has to be written once and can then be used for every event based experiment. Therefore, new experiments simply have to write an experiment summary and use the translation tool to generate the whole framework code of their analyzing software.

**Leads to better analysis frameworks**

If many experiments use the same translation tool, they all can help to improve it, which will also help to improve the functionality and the quality of the generated frameworks. Especially small experiments will benefit from the experience and the manpower of larger ones.

**Leads to better analysis software**

The framework includes all code which is difficult to write from a software technical view point. Since this part is generated, the experimenter can focus on the analysis code. This is usually difficult from a physics view point but not from a software technical view point. Therefore, the experimenter can place more effort into the analysis of the experiment which finally leads to a better physics result.

**Ease of use**

The programming inside a generated framework is easy. All classes are generated by the translation tool. Therefore, they have a consistent naming scheme and a consistent class architecture. Furthermore, if no special user code is added the experimenter does not require object orientated programming knowledge, since the class files can be fully generated. This ensures that, especially for smaller analysis tools, non experienced programmers can contribute significantly to the analysis software. However, the class files can also be fully edited, ensuring that experienced programmers are not limited by the framework and thus can exhaust the full power of c++.

## 5.3 ROME

We implemented the idea of generating frameworks and called the software ROME. In ROME the experiment independent part is implemented as ROME classes which are mainly base classes for the generated classes. The ROME classes are part of the ROME distribution. The translation tool is called the ROMEBuilder. It translates the experiment description given in a XML file into C++ classes.

### 5.3.1 The ROMEBuilder

The ROMEBuilder translates the experiment description specified in an XML file into C++ code. We have chosen XML for the description because it is probably the most used standard ASCII format and it fits perfectly for this purpose. The choice of C++ for the programming language is mainly given by the fact that the generated software depends on the ROOT libraries which are written in C++. The output of the ROMEBuilder are framework classes and task classes. Task classes are based on ROOT tasks [31] which are calculation modules. The ROMEBuilder also compiles and links the classes to an executable and writes html documentation (see figure 5.1). Therefore, when running the ROMEBuilder for the first time it will generate a running executable, however the executable will not include any analysis code. This has to be added by the experimenter to the predefined event methods of the task classes. The ROMEBuilder can then be run again to produce an executable which includes the analysis code. This process can be repeated until the final version of the program is reached. The ROMEBuilder will, of course, not overwrite any user code.

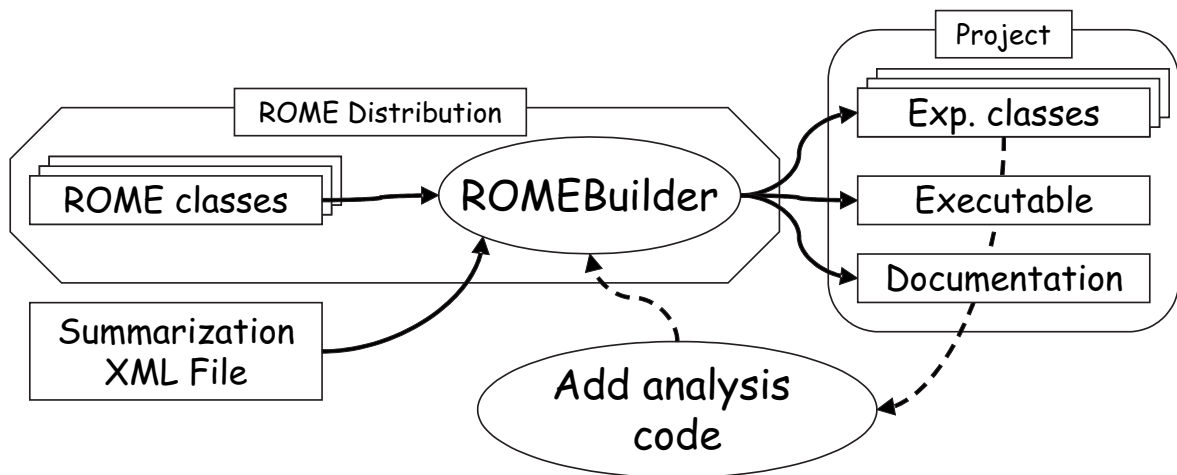


Figure 5.1: The translation program generates all codes of the framework from an experiment description. The framework is also linked and documented.

### 5.3.2 Programming inside ROME

The generated framework is written in C++ and is completely object oriented. However, since all code except for the calculations is generated, the experimenter has only to add code to predefined functions. Therefore, he does not need to write classes himself and hence does not need to know the concept of object orientation. However, if an experienced programmer wishes to extend the framework beyond the capability of ROME he will benefit from the object orientated structure. Accordingly, ROME is designed to be very easy to use for less experienced programmers as well as easy to extend for experienced users. The framework is based on the ROOT libraries and hence the whole functionality of ROOT is available.

### 5.3.3 Features

#### Connection to DAQ Systems

ROME can be used in every event-based experiment for on-line and off-line analysis. So far, only a connection to the MIDAS [29] data acquisition (DAQ) system has been implemented but it can be easily extended to other systems using a plug-in mechanism. Having a framework, which is capable of performing on-line and off-line analysis brings consistency, saves manpower and instruction time.

#### Database Access

The generated program can also be connected to a database. The access to the database is completely covered by the framework, i.e. no database calls have to be implemented by the experimenter. So far, the access to a MySQL database as well as, for small amounts of data, to a XML database, has been implemented. Implementing access to any other database system is also very straight forward and can be done using a plug-in mechanism and without changing the translation program.

#### Socket Connection

ROME analyzers can share objects over socket connections to third party software. This makes it possible for example to access and display, in real time, histograms of an online analyzer in any office around the world.

#### GUI Extension

The ROME distribution also includes a GUI extension called ARGUS. The ARGUS display is generated the same way as the ROME analyzer is generated. Therefore, it can be defined in the same XML definition file as the analyzer. The final program has then three possible running modes. Firstly, it can run as a pure analyzer without

any graphics extension. Secondly, it can run as an analyzer with a GUI displaying the objects of the analyzer. The third possibility is to run it as a pure display. The first mode will usually be used for an online analyzer, since it should run in a reliable way and therefore be as simple as possible. To display the online histograms in a control room or in the various experimenters offices a pure display will be used. These displays get the objects over socket connections described in the previous paragraph. For off-line analysis one would typically run the analyzer together with a display.

### **Modularity**

ROME generated analysis software packages are highly modular. The calculation code is split up into tasks, which contain one or several calculation steps. Tasks can be exchanged arbitrarily as long as they access the same data. In this way two different types of analysis can be performed with the same program, by rearranging the tasks. This can be done simply by configuring the program over an XML configuration file before startup and without relinking of the program.

### **Distribution**

The software runs under Windows, Linux and Macintosh and can be downloaded from a subversion repository. Instructions for downloading and using the software can be found on the ROME home page <http://midas.psi.ch/rome>.



## Part III

# The Drift Chamber Analysis





# Chapter 6

## The First Engineering Run

In December 2006, the collaboration was able to perform the first engineering run with drift chambers, timing counters and the full DAQ system available. In the drift chamber system there were 8 out of 16 chambers mounted. This section discusses the data that was taken during this period.

### 6.1 Hardware problems

In the first engineering run we had problems to apply high voltage to several drift chamber modules. The drift chambers are designed to run at a voltage of around 1800 V. However, outer high voltage connections and decoupling capacitors were for protection embedded in glue to avoid conflict with the pure helium chamber environment. Due to holes in the gluing, imperfections in the design of the prints on which the wires were soldered and broken wires in the first chamber the high voltage of the individual chambers could only be applied to the values given in table 6.1.

Chamber	Plane	High Voltage [V]	problem
DC 4	A	1750	
	B	1550	
DC 5	A	1000	probably a leak
	B	1000	probably a leak
DC 6	A	1650	
	B	1700	
DC 7	A	1500	
	B	0	broken wire
DC 8	A	0	broken wire
	B	1650	
DC 9	A	1000	leak
	B	1000	leak
DC 10	A	1000	leak
	B	1000	leak
DC 11	A	1750	
	B	1650	

Table 6.1: High Voltage applied to the drift chambers in the first engineering run.

## 6.2 Data Analysis

### 6.2.1 Noise

On the waveforms, there are two main components of noise present. One is a fast oscillation with a frequency of about 30 MHz, the other is a slower oscillation with a frequency of about 500 kHz (see figure 6.1 and 6.2). After investigations, we found that the noise was coming from the low voltage DC-DC converter of the high voltage supply. A part of the slow oscillation was also coming from a signal on the DRS boards which was used to control the sampling frequency. Both sources of noise could be eliminated by changing a component of the low voltage supply and by removing the frequency control.

### 6.2.2 Number of Hits per Wire

Even though the signals showed the above mentioned noise, one could measure the number of hits per wire as a function of the beam intensity shown in figure 6.3. This was an important measurement because it indicated how much pile up we will have on the waveforms in the final setup. To do this we had to add a veto logic to the algorithm presented in section 7.1.2 so that we would not count the fast oscillation noise as hits.

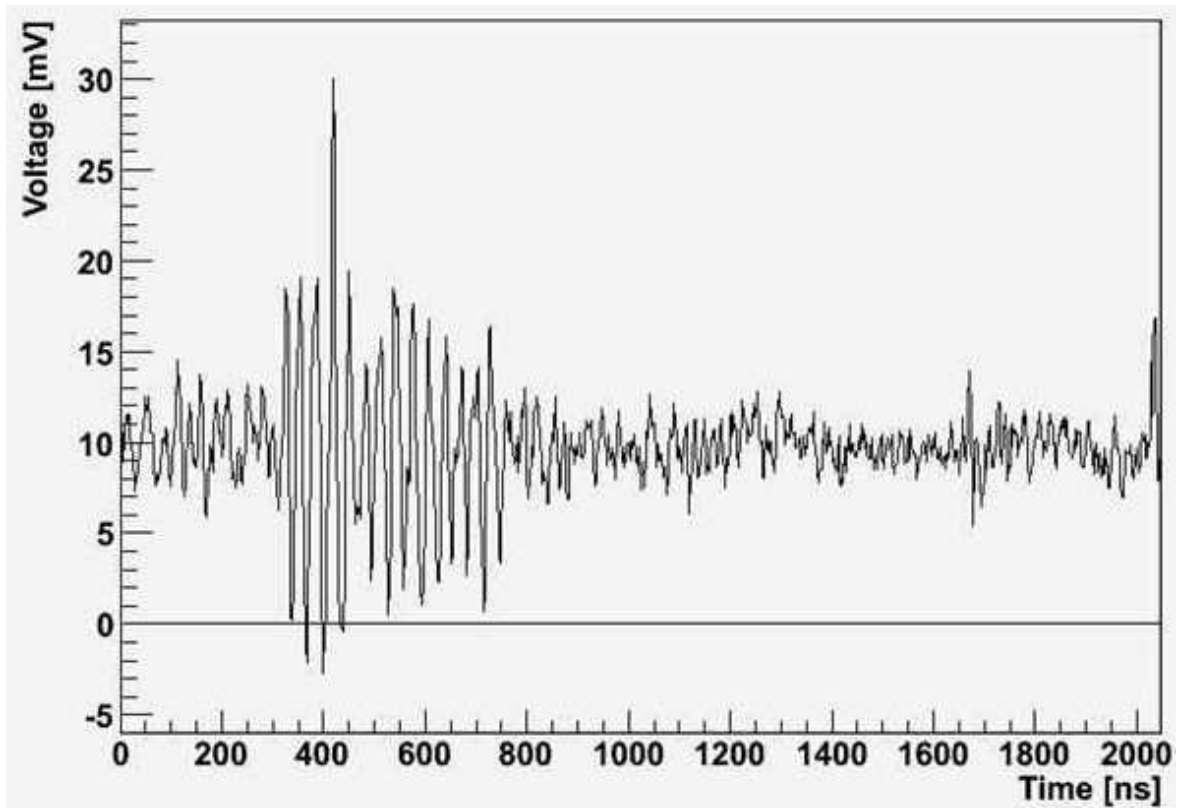


Figure 6.1: Fast oscillation baseline variation in first engineering run data.

## 6.3 Conclusion

In the first engineering run in December 2006, we could successfully test the drift chambers. Several hardware problems occurred which after investigation could either be solved or be used to redesign components, like the anode prints. However the large noise on the signal waveforms and the high voltage problem prevented a deeper analysis of the data.

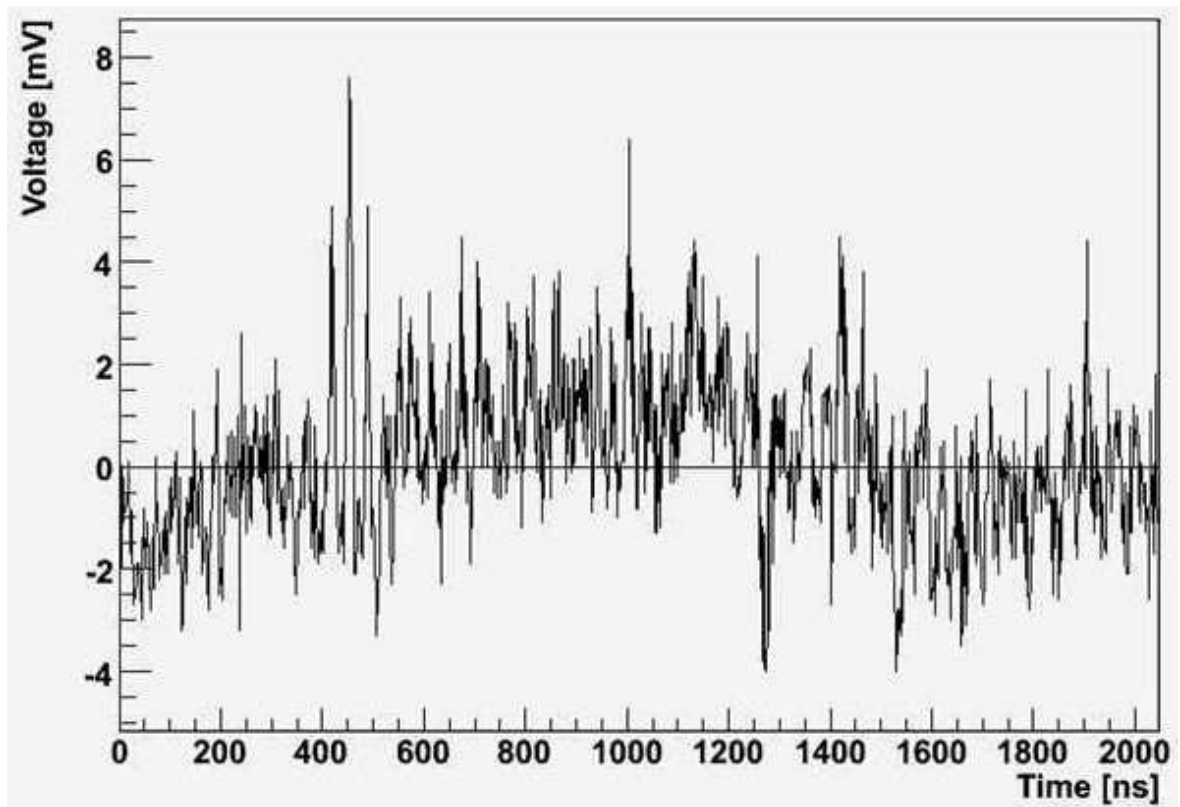


Figure 6.2: Slow oscillation baseline variation in first engineering run data.

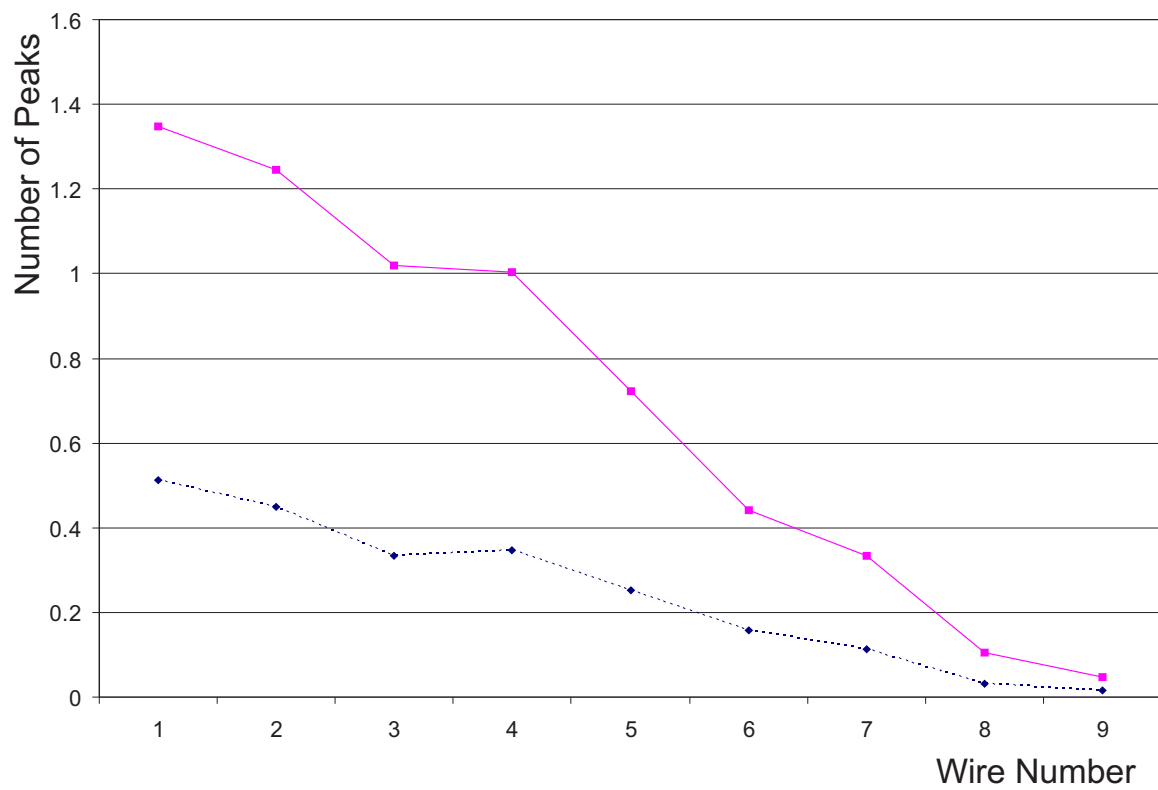


Figure 6.3: This chart shows the number of hits per wire for two different beam intensities. The solid line belongs to full beam intensity, while the dashed one belongs to 25% of the full beam intensity.



# Chapter 7

## Event Reconstruction

In this chapter the main algorithms used to analyze the data taken with the drift chambers are presented. To reconstruct the events, the hits in the drift chamber cells (wires and cathodes) have to be found. The method for the hit reconstruction is described in section 7.1. The hits found in the chamber have to be assigned to tracks from crossing particles. The track finding and the track fitting algorithms are described in section 7.2 and 7.3. Finally, the detector resolutions analyzing Monte Carlo (MC) generated data are given in section 7.4.

### 7.1 Hit Reconstruction

As discussed in section 3.3.2 we read out the drift chamber wires at both ends and the four cathode strips per cell at one end. Therefore, we measure six waveforms per cell (see figure 7.1 for an example). The goal of the hit reconstruction is to obtain a hit defined by a hit time  $t$  (time when the drift electron reaches the wire) and a  $z$  coordinate. The algorithm is presented in the following sections.

#### 7.1.1 Noise Subtraction on Wire Signals

The carbon fiber frames are not ideal conductors. Due to that, an oscillation on the waveforms readout at the two ends of the wire is observed. Additional grounding between the two prints of both wire ends largely reduced but not completely eliminated the oscillation. This sine like noise has a  $180^\circ$  phase difference between the two ends of the wires. Hence, the disturbing oscillation can be subtracted by applying the following steps:

- Sum the waveforms of both ends of the wire and search for peaks (see section 7.1.2).

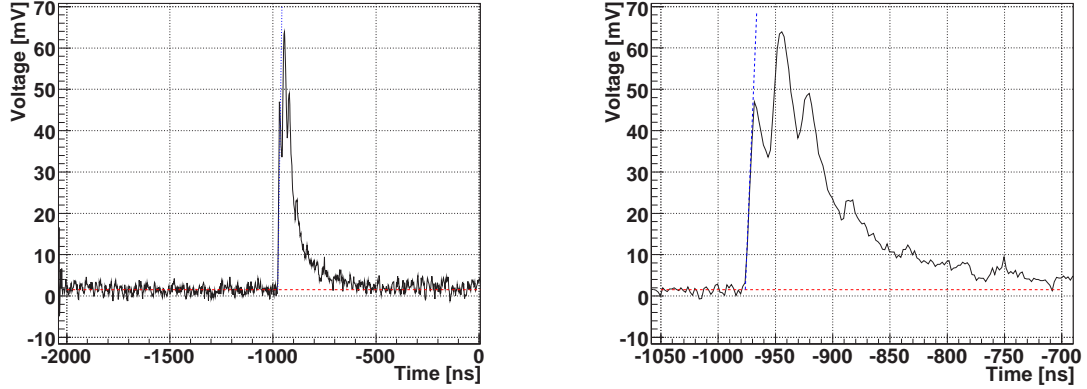


Figure 7.1: An example of a waveform recorded with the drift chambers. The dashed red line indicates the baseline fit. The dotted blue line indicates the rising edge fit of the signal peak. The plot on the right side is a magnification of the plot on the left side.

- Subtract the waveform of one end of the wire from the waveform of the other end. Fit a third order polynomial function to the differential waveform excluding the peak region.
- Use the fitted polynomial function to subtract the noise on the original wire waveforms.

As shown in figure 7.2 the sine like noise on the two ends of the anode (up-stream/downstream) is clearly anti-correlated. The amplitude of the noise is varying between 0-2 mV.

### 7.1.2 Baseline Determination and Peak Finding

First a rough baseline estimation is performed. For this purpose, the waveform amplitudes are filled in a histogram. The amplitude with the maximal number of entries of the distribution will be taken as a first baseline estimate. We take the maximum rather than the mean of the distribution because this value is less sensitive to the tails coming from small signal peaks on the waveform.

To find the signal peaks on the waveform the method of moving averages is used. The start and the end of a peak is defined as the time when the moving average crosses a threshold. A pile up will be recognized by the change of the derivative from negative to positive inside a peak region.

After the peak finding process the baseline calculation can be improved by using only the part of the waveform out of the peak regions for the baseline evaluation.



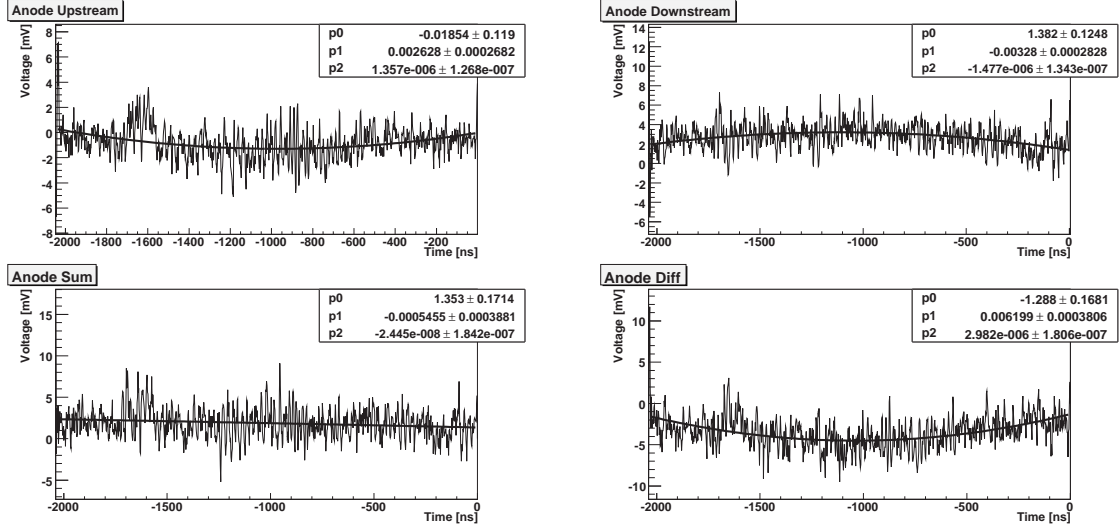


Figure 7.2: The upper left plot shows the anode signal on the upstream readout, while the upper right plot shows the anode signal on the downstream readout. The lower left (right) plot shows the sum (difference) of these two signals. For these plots a second order polynomial function was fitted to the waveforms.

### 7.1.3 Leading Edge Fit

We define the hit time as time of the first arrival of a drift electron on the wire. To obtain this time the leading edge of the signal is fitted. In a first step the point on the rising edge, where the gradient reaches its maximum needs to be determined. Secondly, the rising edge is fitted with a second order polynomial function. To optimize the time measurement, several fits are performed including different sets of points around the point with the maximal gradient. Out of the various fits the one with the smallest ratio of  $\chi^2$  over the number of degree of freedom is used. The peak time is then defined as the time of the intersection point between the fitted leading edge and the fitted baseline. To get the hit time the peak times of the two wire ends are averaged.

### 7.1.4 Charge Integration

The signal propagation on a wire depends on the frequency spectrum of the signal. Since different integration lengths select different frequencies out of the total frequency spectrum of the pulse, the charge division will be different, if the length of the charge integration interval is changed. Therefore, the integration length must be fixed for all signals of the chamber and for all calibration procedures involving integration. In this work we used an integration length of 75 ns. The start point of the integration for the individual waveforms is taken from the leading edge fit. If there is no time available

from the fit (e.g. for small cathode signals) the hit time (average of the two wire ends) is taken.

### **7.1.5 Z Coordinate Evaluation**

To get the  $z$  coordinate of the hit, anode and cathode asymmetries are calculated. A rough estimate of the  $z$  coordinate can be obtained by applying the charge division method to the anode signals. This coordinate will select the cathode strip period. Using the cathode asymmetry the phase inside the concerning cathode strip period can be determined leading to the final  $z$  coordinate measurement. Please see section 3.3.2 for a description of the cathode geometry.

## 7.2 Track Finding

Even though the Kalman filter presented in section 7.3 is capable of finding tracks, we wrote a separated track finding code which is much faster in recognizing tracks than the Kalman filter. In a first step the algorithm clusters hits together, which, in a second step can be used to find track seeds. From the seeds the drift time can be determined in an iterative approach. Finally, the tracks are extrapolated to other chambers.

### 7.2.1 Clustering Hits

Two hits which are close enough in  $z$  are combined to a hit cluster. The requirements for building a cluster are:

- Two hits in the same chamber plane
  - ◊  $\Delta z < 0.2 \text{ cm} + z_1 \cdot 0.02 \text{ cm}$ ,
  - ◊  $\text{cell}_1 - \text{cell}_2 = \pm 1$ ,
- Two hits in different chamber planes
  - ◊  $\Delta z < 0.6 \text{ cm} + z_1 \cdot 0.046 \text{ cm}$ ,
  - ◊  $\text{cell}_1 - \text{cell}_2 = \pm 2$ ,

There is no grouping of more than two hits because at this stage there is no information available to distinguish hits belonging to two different tracks which overlap in  $z$ .

### 7.2.2 Finding a Track Seed

In the next step we search for all possible combinations of three clusters in consecutive chambers. The clusters must fulfill

$$z_{\text{projection}} - z_{\text{newcluster}} < 0.6 \text{ cm} + z_{\text{projection}} \cdot 0.05 \text{ cm}. \quad (7.1)$$

Please see appendix A for a definition of  $z_{\text{projection}}$ . The found cluster combinations are then called a track seed.

### 7.2.3 Calculating the Drift Time of the Hits

In the hit reconstruction the time when the drift electrons reach the wire, is determined. This time is then called the hit time. However, the time when the particle passed, hence the time when the drift avalanche started, is unknown. Therefore, the drift time is a priori unknown. On the other hand, the flight time of the particle between the chambers

is very small compared to the drift time. Hence, from the hit time measurements the differences of the drift time among the hits belonging to the same track are known. Thus, the only unknown parameter is the smallest drift time of the hits of the same track. This fact can be used to calculate the drift times of the hits in a track seed in an iterative approach performing the following steps.

- Calculate a circle through the three cluster positions of a track seed. A cluster position is defined as the central point between the wire positions of the two hits of the cluster.
- Extract the track angle  $\alpha_i$  at each hit position. The track angle is the angle between the flight direction of the particle and the normal vector of the chamber.
- Find the smallest hit time of all hits in the track seed and define this time as  $t_0$ .
- Iteratively, perform the following steps by reducing  $t_0$  after each cycle until a minimum of the deviation between hit point and track is found.
  - ◊ Calculate the two possible hit points  $p_i$  by applying the so called t-xy function. This function defines the relation between the drift time, the track angle, the magnetic field, the voltage potential on the wire and the drift distance. The function is used with the current estimate of the drift time  $t_{hit_i} - t_0$ , the track angle  $\alpha_i$  and the magnetic field strength at the current chamber cell.
  - ◊ Loop over all possible combinations of hit points and make the following calculations:
    - \* Recalculate the track by using the calculated hit points instead of the wire positions.
    - \* Calculate the deviation of the hit points from the track.
  - ◊ Choose the combination with the minimal deviation of the hit points from the track.

Figure 7.3 illustrates this process. The dashed circles represent the starting situation before  $t_0$  optimization and the red circles show the drift circles after optimization.

### 7.2.4 Extrapolating Tracks

After having found a track seed with the corresponding drift times of the hits, further hits are added to the track. The drift time of the new hits will now be calculated using the information from the track seed. The newly added hit or cluster of hits must also fulfill equation 7.1. If there are more than one cluster or hits which could be added to

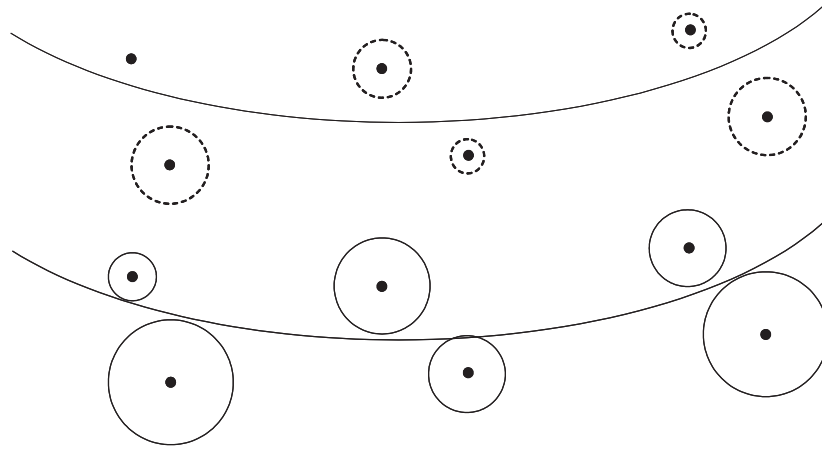


Figure 7.3: Schematic illustration how the drift time is calculated by using the hit information of six hits. The circles in the upper figure represents the minimal drift circles obtained by subtracting the hit time of the earliest hit  $t_{first}$  from the hit time of the other hits  $t_i$ . The lower figure shows the drift circles after the optimization process.

the track, the best solution is chosen by means of minimizing the deviation of the hit points from the track. In the extrapolation, not only clusters but also single hits will be included. Furthermore, the extrapolation is not terminated when one chamber is missing between two chambers containing hits belonging to the track, but continued with the next chamber.

### 7.2.5 Solve Left-Right Ambiguity

A priori it is not known on which side of the wire the track passed. When a track was found this left-right ambiguity will be solved by checking if the track passed the wire at a larger or a smaller radius. If the track passed too close to the wire the decision will be postponed and will be solved during the track fitting, since the track path will be better known in that step.

## 7.3 Track Fitting

The fitting of the tracks is performed by a Kalman Filter [32]. This algorithm calculates the propagation of the state vector in time by performing recursive prediction and decision steps. The decisions are made by minimizing the sum squared residuals normalized to the error. The algorithm includes also multiple scattering and energy loss on the track path through the detector.

## 7.4 MC Resolution and Efficiency

The resolution and efficiency of the track reconstruction was measured with MC data. The MC sample was produced by setting one signal ( $\mu^+ \rightarrow e^+\gamma$ ) event at time equal 0 to simulate the triggered event. To simulate the background from Michel decays, randomly placed events from normal muon decays have been added, corresponding to muon decay rate of  $3 \cdot 10^7$  decays per second. Please see figure 7.4 for an example of a fully reconstructed event. The analysis was performed by analyzing 1000 events.

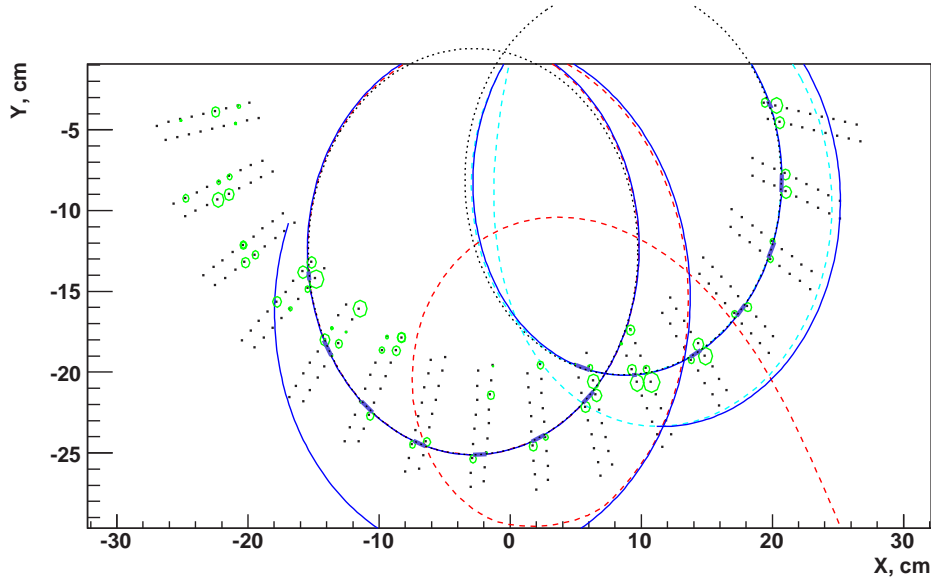


Figure 7.4: An example of a reconstructed event. The dashed red line represents a positron from a MC signal track, while the dashed cyan line represents a positron from a MC background track. The dotted black circles are track candidates from the track finding stage, while the solid blue lines are the fitted reconstructed tracks. The drift circles of the hits are drawn in green. The black dots represent the wire positions.

The momentum resolution of the signal tracks is shown in figure 7.5. The resolution determined by a single gaussian fit is (all resolutions in this sections are given in  $\sigma$  units)

$$\sigma_E = 0.27 \text{ MeV}. \quad (7.2)$$

Since a single gaussian function does not fit the distribution very well, the histogram was also fitted with three overlaying gaussian functions. The result is  $\sigma_1 = 0.05$  MeV,  $\sigma_2 = 0.25$  MeV and  $\sigma_3 = 2.18$  MeV, where the areas of the gaussian functions are at a ratio of 1:8.6:1.9. Our goal is a resolution of 0.18 MeV, which was estimated with a previous version of the MC. The main contribution to the worse resolution comes from multiple scattering. The previous version of the MC did not contain all material inside

the detector. Especially, contributions from cables were largely underestimated. The worse energy resolution has an impact on the  $\mu^+ \rightarrow e^+ \gamma$  decay sensitivity of 4%.

The angular resolution on the target in  $\Theta$  is

$$\sigma_{\Theta} = 5.5 \text{ mrad}, \quad (7.3)$$

whereas the resolution in  $\phi$  is

$$\sigma_{\phi} = 8.4 \text{ mrad}, \quad (7.4)$$

shown in figure 7.6. The  $\mu$  decay vertex on the target is reconstructed to a precision of

$$\sigma_R = 1.2 \text{ mm} \quad (7.5)$$

in the R-direction and

$$\sigma_Z = 1.1 \text{ mm} \quad (7.6)$$

in Z-direction (figure 7.7). This leads to a vertex reconstruction resolution of 1.6 mm, which is almost two times worse than the aimed value of 0.9 mm. The worse energy resolution has an impact on the  $\mu^+ \rightarrow e^+ \gamma$  decay sensitivity of 15%.

The reconstruction algorithm succeeds to find 99% of all tracks. Although, in 45% of the reconstructed tracks one or more hits are missing (see figure 7.8).

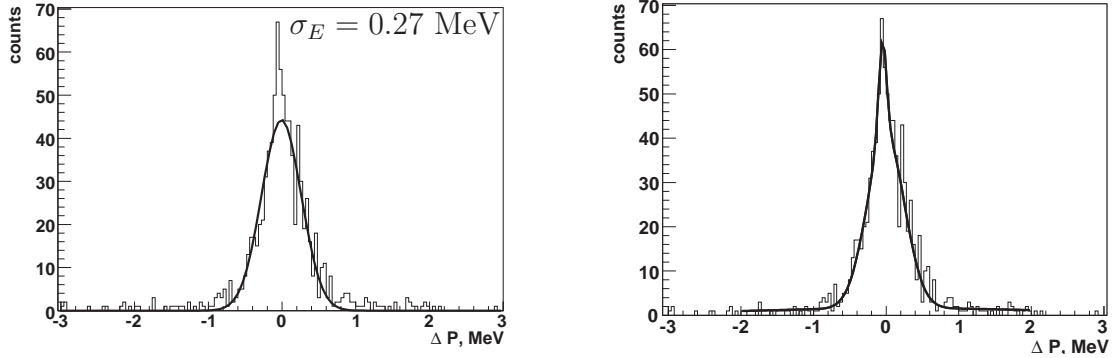


Figure 7.5: Momentum resolution of reconstructed MC signal tracks. The histogram on the left side is fitted with a single gaussian function, while the same histogram is fitted with three overlaying gaussian functions on the right side.

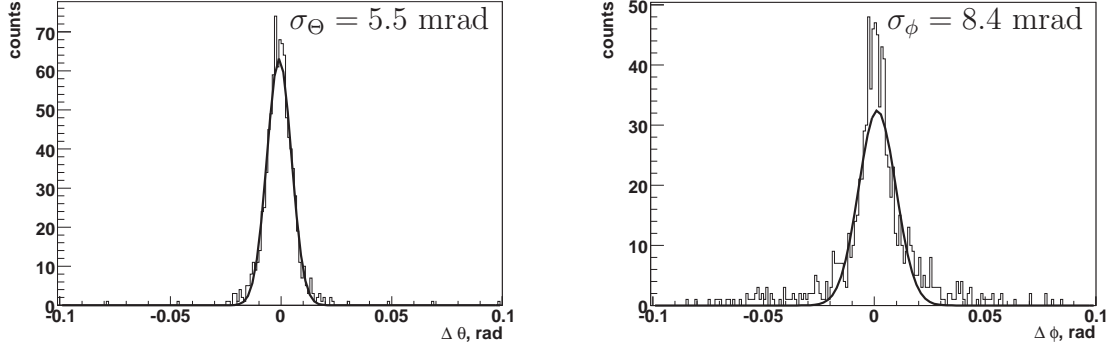


Figure 7.6: The left (right) side plot shows the  $\Theta$  ( $\phi$ ) resolution of reconstructed MC signal tracks.

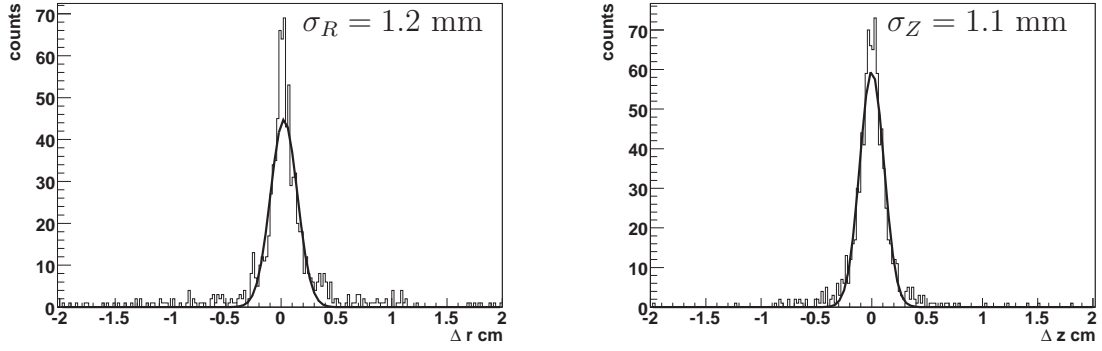


Figure 7.7: The left (right) side plot shows the resolution in the R-direction (Z-direction) of the reconstructed  $\mu$  decay vertex on the target for MC signal tracks.

## 7.5 Conclusion

The measured resolutions are all worse than the predicted resolutions. The main contribution to the worse resolutions comes from the additional material, which was added into the newest version of the detector simulation. Older simulations had only a rough or no information about cables and support structures. This results may be improved by further improvements in the track reconstruction algorithms. However, the current results imply a reduction of the  $\mu^+ \rightarrow e^+ \gamma$  decay sensitivity in the order of 20% compared to the published value.



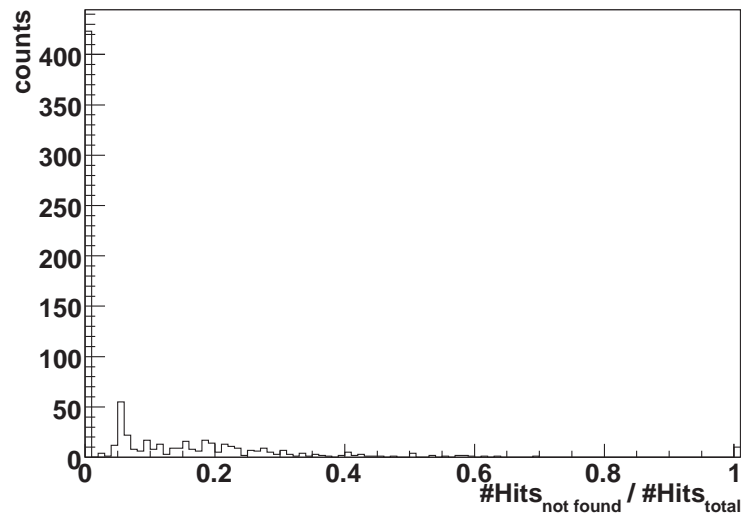


Figure 7.8: The fraction of the number of hits of a track that where missed during the track finding stage over the total number of hit in the track is shown.



# Chapter 8

## Calibrations

Various properties of the drift chamber hardware have to be measured and calibrated. In the measurement of the  $z$  coordinate the charge gains on both the anode and the cathode and the signal propagation on the wire have to be calibrated. This is discussed in section 8.2.1 and 8.2.2. The transition time of the signals from the detector to the sampling chip as well as the transition time of the trigger signals have to be measured (section 8.3). In section 8.4 the wire alignment is presented, while section 8.5 presents a way of cross checking the relation between the drift time and the drift distance.

### 8.1 Data Set

All Calibrations were made with data taken at the end of 2007. In this run period all detector components were working. The drift chambers were equipped with all 16 chambers. Due to low statistics in the cosmic ray data, for some chambers (see also section 8.3), all calibrations discussed in this chapter were made by analyzing positrons from Michel events. The beam intensity for all runs was  $5 \cdot 10^6$  muons per second. The voltage applied to the drift chamber wires is listed in table 8.1. The preferred voltage is 1850 V, however due to isolation problems outside of the chambers, several chamber planes could only be run at 1800 V. Due to bad connections of signal or low voltage cables, several channels were not working. In total 73 out of 288 cells were excluded for this analysis. This was due to a non optimized closing procedure of the magnet. In the Michel runs the trigger was fired when four hits in consecutive chambers are over a threshold and in a certain time interval.

To reduce the amount of badly measured hits several cuts have been applied to the data used for the calibrations (table 8.2). The hit amplitudes are required to exceed a threshold, while for the hit charges a minimal charge is required. Another restriction is the request on the cathode sum radius  $r$ , which is a good indicator for exceptional noise. It is defined as

Run numbers	5822-6088
Planes on 1850V	1B,7AB,12AB,15AB
Planes on 1800V	all others

Table 8.1: A summary of the high voltage values applied to the different drift chamber planes

$$r = \sqrt{\left(0.5 - \frac{Q_{uh} + Q_{dh}}{Q_u + Q_d}\right)^2 + \left(0.5 - \frac{Q_{uc} + Q_{dc}}{Q_u + Q_d}\right)^2} \quad (8.1)$$

$Q_u$  and  $Q_d$  denote the charges on the anode on both sides of the wire, whereas  $Q_{uh}$ ,  $Q_{dh}$ ,  $Q_{uc}$  and  $Q_{dc}$  are the four charges measured on the foils for both hood and cathode.

threshold	4 mV
min. charge	2000 mV·ns
max. cathode sum radius (see eq. 8.1)	0.15

Table 8.2: Cuts applied to the data used for the calibrations.

## 8.2 Z Calibration

The measurement of the z coordinate depends on several components of the drift chambers. The relative charge gains on both the anodes and the cathodes are a combination of the gas amplification inside the chamber, common for all signals, and the preamplifier gain. Furthermore, the wire properties like length, resistance, capacity etc. define the normalization of the anode z measurement to the cathode z measurement.

### 8.2.1 Anode Gain Calibration and Anode-Cathode Normalization

Since the charge of a signal travelling on a wire decreases, the hit position along the wire can be deduced by comparing the charges measured at both ends of the wire. We define the anode asymmetry  $asymA$ , which is proportional to the z coordinate as

$$asymA = \frac{Q_d - Q_u}{Q_d + Q_u}, \quad (8.2)$$

where  $Q_u$  and  $Q_d$  are defined in section 8.1.

The z coordinate can also be measured by comparing the charges measured on the four cathode strips. The relative charge differences on the cathode define the phase

$\alpha$  inside a cathode strip period. Please see section 3.3.2 for a description of the drift chamber hardware. The phase  $\alpha$  is defined as

$$\alpha = \arctan \left( \frac{cathAsym0}{cathAsym1} \right) \quad (8.3)$$

where

$$cathAsym0 = \frac{Q_{uh}-Q_{dh}}{Q_{uh}+Q_{dh}} \quad \text{and} \quad cathAsym1 = \frac{Q_{uc}-Q_{dc}}{Q_{uc}+Q_{dc}} \quad \text{for plane A} \quad (8.4)$$

or

$$cathAsym0 = \frac{Q_{dc}-Q_{uc}}{Q_{dc}+Q_{uc}} \quad \text{and} \quad cathAsym1 = \frac{Q_{dh}-Q_{uh}}{Q_{dh}+Q_{uh}} \quad \text{for plane B.}$$

$Q_{uh}$ ,  $Q_{dh}$ ,  $Q_{uc}$  and  $Q_{dc}$  are defined in section 8.1.

The anode measurement will be used to determine the correct cathode strip period. The precise z coordinate measurement will then be obtained by the measurement on the cathode.

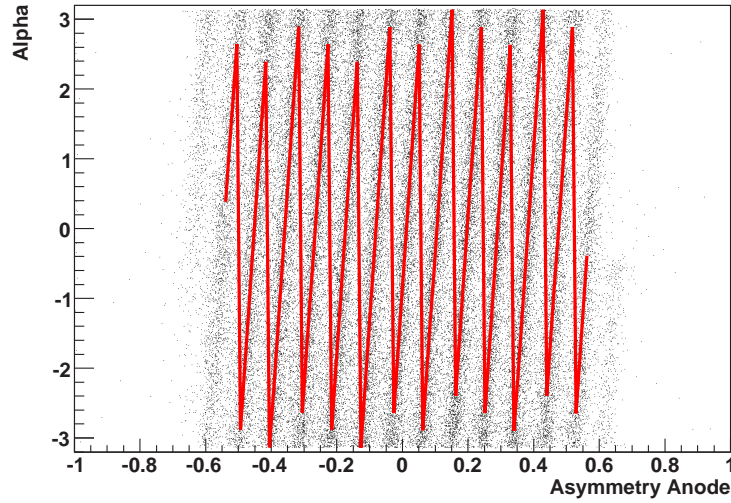


Figure 8.1: Alpha vs. the Anode Asymmetry.

The relative anode gain and the anode-cathode normalization factor can be deduced by comparing  $\alpha$  and  $asymA$ . The histogram in figure 8.1 shows  $\alpha$  as a function of the anode asymmetry  $asymA$ . The histogram is fitted with a first order polynomial function with a period of  $2\pi$  in  $\alpha$ . The slope of the function gives the normalization factor of the anode in respect to the cathode and the value of  $asymA$  at  $\alpha = -\pi/4$  is

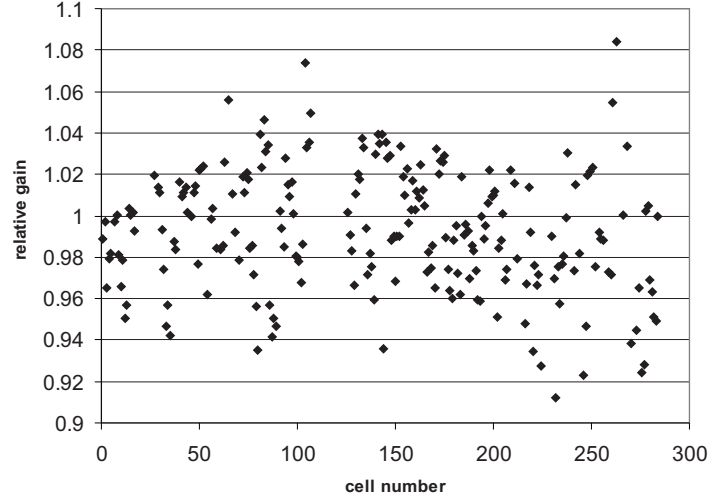


Figure 8.2: Anode Gain Spread.

equivalent to the anode gain. This fit has to be carried out for all cells of all chambers. The measured relative gains are shown in figure 8.2. The variation of the gain mainly due to preamplifier gain variation is 3%.

### 8.2.2 Cathode Gain Calibration

The mean charge measured on the cathodes, averaged over many events, must be the same for each of the four cathode strips. Therefore, by averaging the measured charge in a cathode period the relative cathode gains can be deduced. The histogram in figure 8.3 shows the charge on one channel of the cathode normalized on the sum of the charges of the anode as a function of  $\alpha$ . The histogram is fitted with a sinus function  $\sin(x) = C + A \cdot \sin(x - \phi)$ . The constant term  $C$  is equivalent to the cathode gain. The gain is adjusted so that the charges on the four cathodes of a cell  $Q_{uh}$ ,  $Q_{dh}$ ,  $Q_{uc}$  and  $Q_{dc}$  are equal to 0.25 of the sum of charges on the anode. The measured relative gains are shown in figure 8.4. The variation of the cathode gain is 9%.

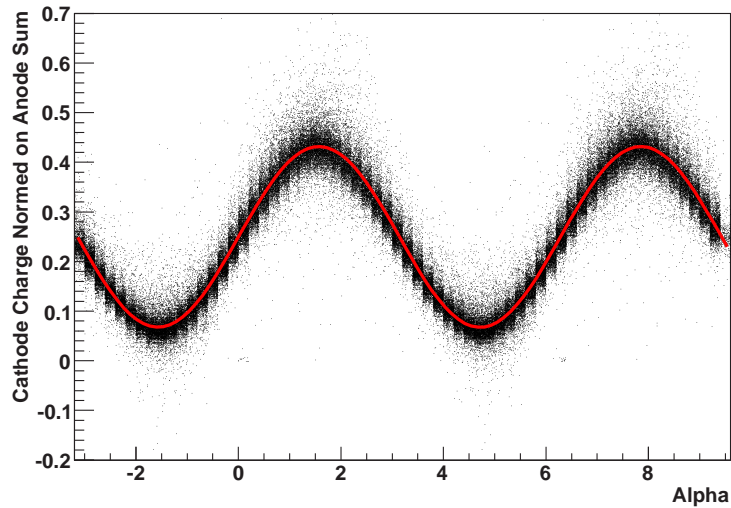


Figure 8.3: Cathode Charge vs. Alpha.

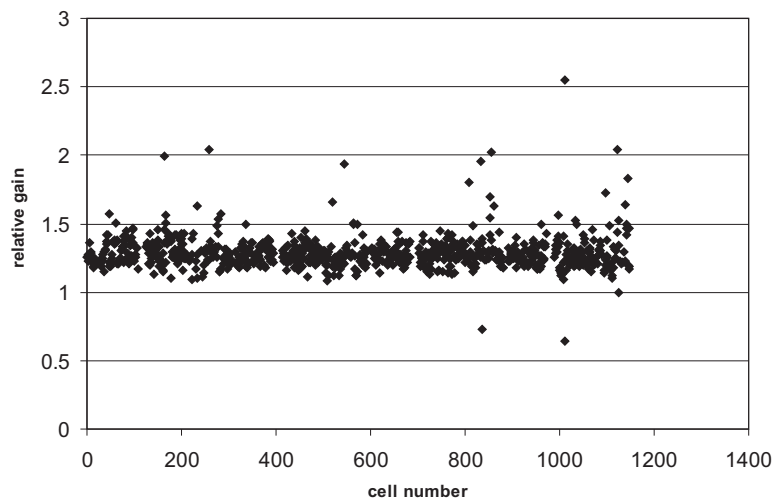


Figure 8.4: Cathode Gain Spread.

## 8.3 Time Calibration

The relative timing of the signals taken with the drift chambers has to be calibrated as well. There are several sources of difference in the propagation time among the channels of the drift chamber: differences in cable length of both the signal and the trigger cables and differences in transition time of electronic devices (Pre-Amplifier, DRS chip, ...).

In principal the transition time of each piece of hardware can be measured. Such measurements are, however, in some cases difficult to perform. It is more convenient to measure the relative timing with real data. For this purpose and also for the chamber alignment the MEG detector was temporarily equipped with cosmic ray scintillation counters (see figure 8.5). Cosmic rays measured in absence of a magnetic field would allow us to calibrate the detector in a very precise way. Unfortunately, it turned out that the chambers on the opposite side of the counters did not collect enough statistics for a proper calibration. The hit rate on the wires was the expected one, but due to many missing channels in these chambers we obtained a very low reconstructed track rate. Therefore, the detector was calibrated with data from Michel decays.

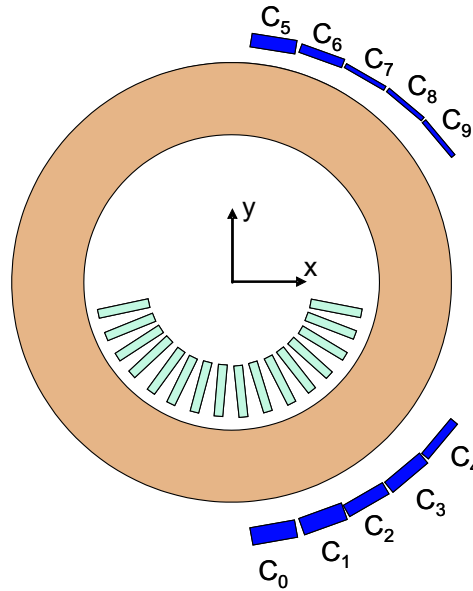


Figure 8.5: Layout of the cosmic ray counter installation. The blue bars illustrate the positions and the thickness of the cosmic ray counters, the green bars correspond to the drift chambers and the orange ring shows the COBRA magnet.

The Michel event trigger is fired when the last one of four required hits in consecutive chambers has been recorded. This hit will be placed at the nominal trigger time inside the waveform range. To measure a reference time, we fitted the leading edge of the signal peak of the peak time histograms in figure 8.6 with a gaussian function. By comparing the mean value of the gaussian with other channels we could calibrate out the relative time differences. However, this method has several disadvantages compared to a calibration with cosmic data. First of all, trigger decisions are only made every 5 ns. Therefore, this method will never be able to calibrate the relative propagation time to better than 5 ns. Secondly, since the trigger time is associated to one out of four hits, the rising edge of the signal peak time distribution is not as sharp as the one



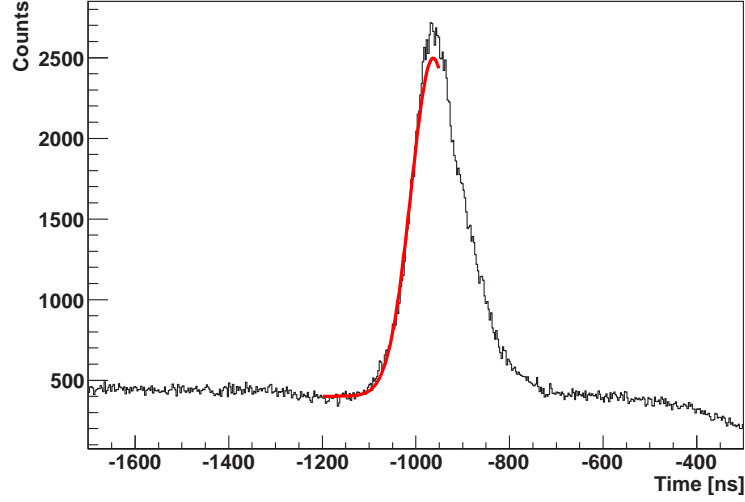


Figure 8.6: Peak time distribution on a single channel fitted with a gaussian. The gaussian function is shown as a red curve.

obtained in a cosmic ray measurement, where the chamber hit time is compared to the scintillator hit time. Furthermore, in this measurement only the difference between the propagation time from the detector to the DRS chip and the propagation time from the detector going to the trigger boards can be measured. Thus, we have to assume that the differences of the propagation time of different signals to the trigger is much smaller than the differences of propagation time to the DRS. For the current arrangement in the experimental area that is a good assumption.

## 8.4 Wire Alignment

The chamber positions and orientations inside COBRA were measured by the PSI survey group in an optical measurement. The relative wire displacements were measured with Michel data (see 8.3). Figure 8.7 shows the deviation from the expected hit point to the fitted track in radial direction for a given wire. The mean of this distribution is proportional to the wire displacement. Since this measurement depends on the wire displacements of all neighboring wires included in the track fit, this correction has to be applied in an iterative way. The same was done for the wire displacement in Z direction. Figure 8.8 shows the miss-alignment for all wires in R (left side) and Z (right side). It can be seen that there are still some chamber displacements left even after the correction of the survey group measurement. The deviations of both Z and R have been reduced to less than 0.1 mm after three iterations.

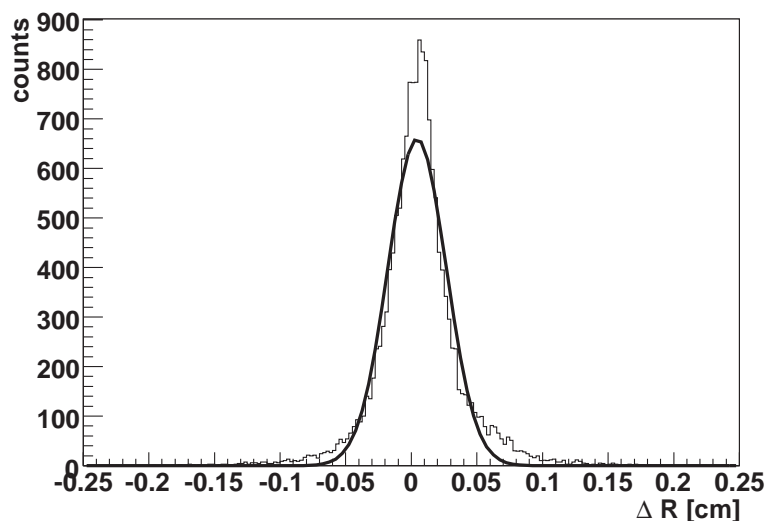


Figure 8.7: A sample histogram of a  $\Delta R$  distribution on a single wire fitted with a gaussian function. The mean of the gaussian is slightly offset from zero, which can be translated into a wire offset.

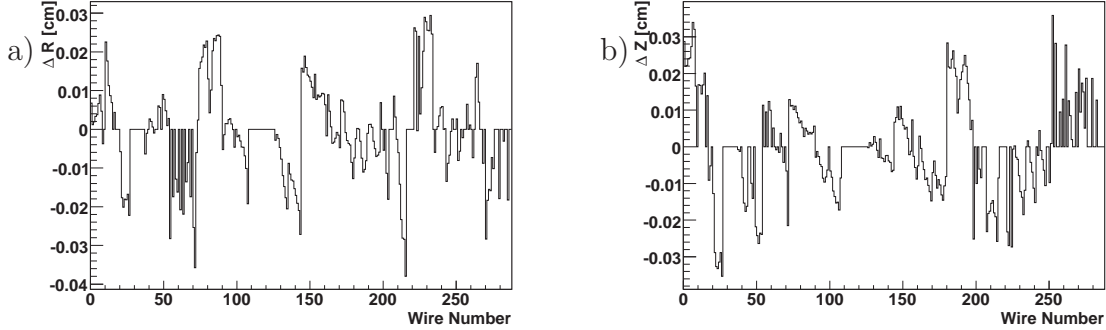


Figure 8.8: The left side plot shows the displacement in R direction of the wires before the alignment procedure. On the right side a similar plot is displayed, showing the displacement in Z. The entries at zero belong to dead channels.

## 8.5 X-T Function Calibration

The relation of the drift time to the drift distance has been calculated in the drift chamber simulation. To check this relation for each wire the deviations of the hits to the track  $\Delta R$  in respect to the track angle  $\alpha$  and the drift distance  $R$  were plotted. In the left side plot in figure 8.9,  $\Delta R$  is plotted against  $R$  while in the right side plot in figure 8.9,  $\Delta R$  is plotted against  $\alpha$ . In neither of these two plots a significant deviation can be observed.

The relation of the drift time to the drift distance is amongst others related to the lorentz angle which is the angle between the drift direction of the electrons and the electrical field. The lorentz angle is an important property of the drift chambers and was simulated with monte carlo simulation (figure 8.10). Since no deviation in the x-t relation could be observed, the current data also doesn't show a deviation from the simulated lorentz angle.

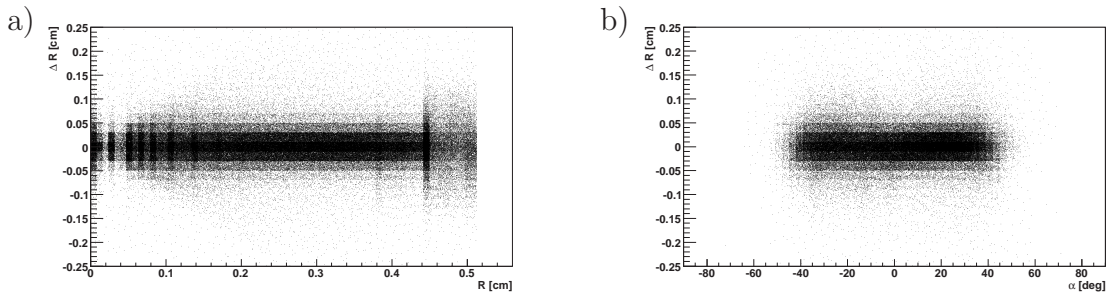


Figure 8.9: Histograms for checking the X-T relation. In figure a) the deviations of the hits to the track  $\Delta R$  is plotted versus  $R$ . In figure b) the deviations of the hits to the track  $\Delta R$  is plotted versus the track angle  $\alpha$ .

### Angle between $v$ and $E$ vs $E$

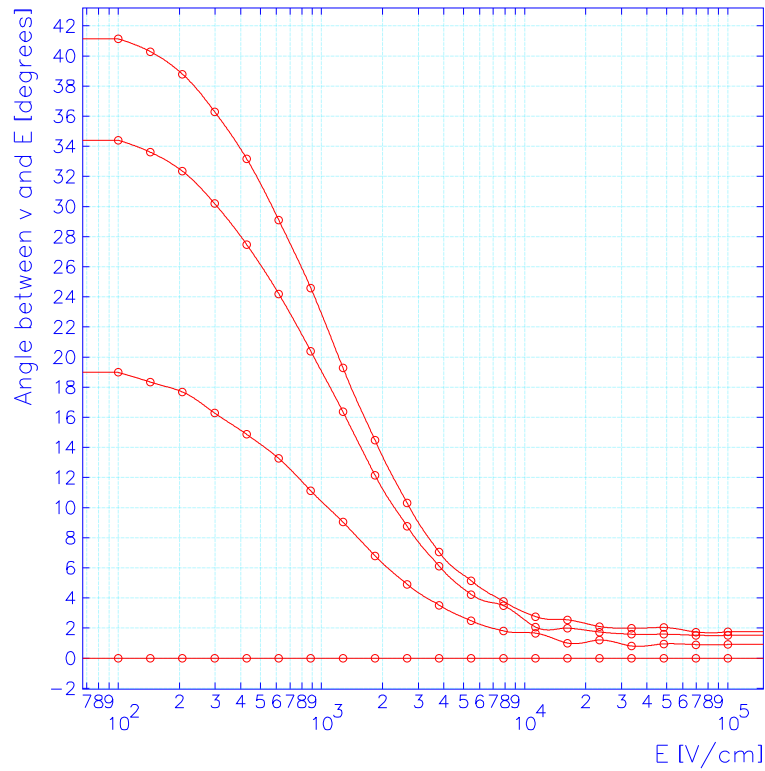


Figure 8.10: The computed lorentz angle for the MEG drift chambers as a function of the electric field. The four curves correspond to an angle between the E- and B-field of  $0^\circ$ ,  $30^\circ$ ,  $60^\circ$  and  $90^\circ$  (from bottom to top). For the MEG drift chambers the  $90^\circ$  curve is important.

## 8.6 Detector Resolution

This section presents the results on the Z and R resolution after applying all the above explained calibrations. The Z resolution on the anodes can be measured by comparing the Z measurement of the anode  $Z_{anode}$  to the one of the cathode  $Z_{cathode}$ , since the cathode measurement is 10 times more accurate than the anode measurement. The difference  $Z_{cathode} - Z_{anode}$  is shown in figure 8.11 for the innermost (leftside) and the outermost (rightside) wire of a chamber. The anode resolution is between 1.06 cm and 0.68 cm, which almost satisfies the designed resolution of less than 1 cm. The resolution is better for the outermost wire because the anode measurement worsens with the length of the wire. The histogram is cut at  $\pm 2.5$  cm, which is the cathode period length. Measurements with a larger error than 2.5 cm correspond to the wrong cathode period. With the current resolution only 1 % of the anode Z measurements will point to the wrong cathode period.

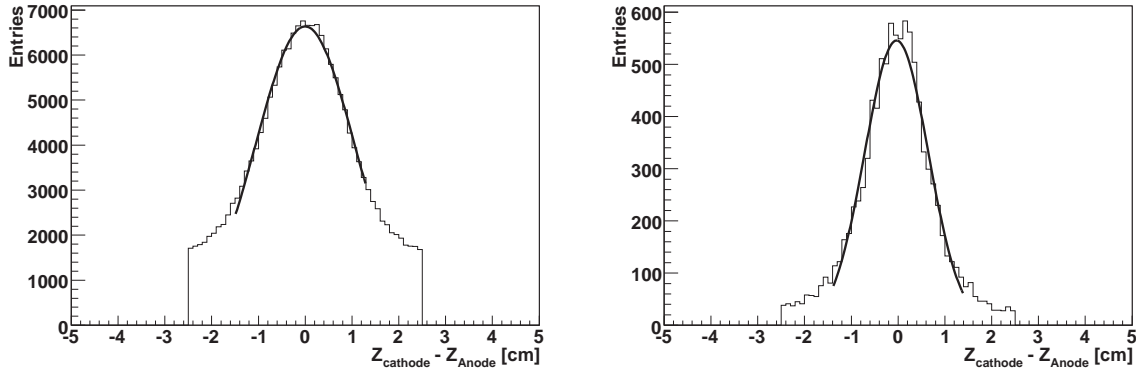


Figure 8.11: The anode Z resolution for the innermost (leftside) and the outermost (rightside) wire of a chamber.

The R resolution and the Z resolution of the chambers measured with the cathode strips are determined by looking at the deviations of the calculated hit positions from the fitted tracks. The results are shown in figure 8.12 for the Z resolution (leftside) and the R resolution (rightside). The R resolution is

$$\sigma_R = 230 \mu m, \quad (8.5)$$

which is already very close to the aimed value of  $200 \mu m$ , while the Z resolution is

$$\sigma_Z = 900 \mu m, \quad (8.6)$$

which is 3 times worse than our goal of  $300 \mu m$ . The Z resolution is mainly limited by the noise on the DRS2 chip, especially, by the fake pulses on the chip described in

section 4.2. The DRS2 chip will be replaced by a new version of the chip (DRS4) in summer 2008. Using the DRS4 chip the z resolution is expected to improve significantly.

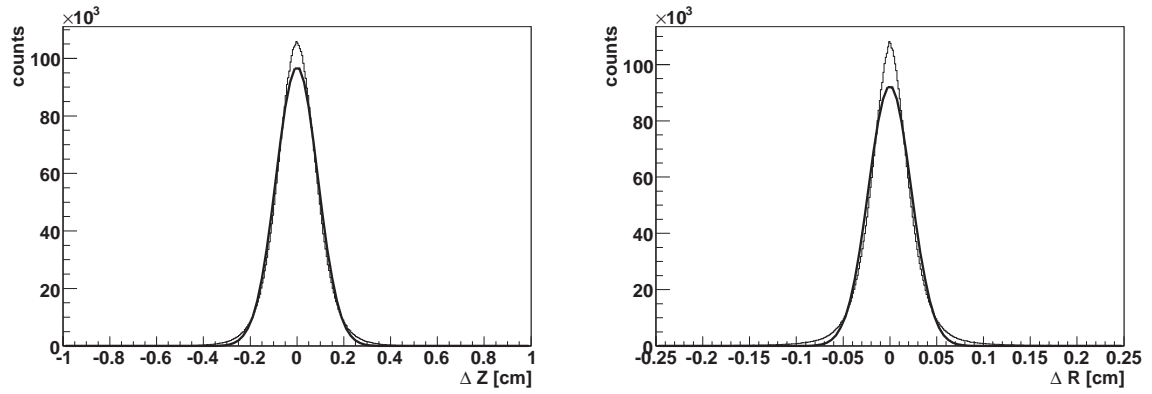


Figure 8.12: The Z resolution (leftside) and R resolution (rightside) in the chamber are shown. The histograms show the sum of all wires of all chambers.

# Chapter 9

## Data Analysis

In this chapter the results of the energy measurement with the drift chambers are presented. Section 9.1 is a theoretical introduction to the Michel decay. The data set used for this analysis will be presented in section 9.2. The measurement of the energy resolution of the drift chambers is discussed in section 9.3 followed by the presentation of the Michel parameter determination in section 9.4.

### 9.1 Electron Energy Spectrum in a Muon Decay

In 1949 Michel [33] was the first to describe the muon decay process in a general form. Out of a study of the coupling between four fermions he formulated the decay probability of unpolarized muons (see [33] and [34]),

$$\frac{dN}{dx}(x; \rho) = A \left[ 3(1-x) + 2\rho\left(\frac{4}{3}x - 1\right) + 3\eta \left(\frac{m_e}{m_\mu}\right) \frac{1-x}{x} \right] x^2. \quad (9.1)$$

$x = \frac{2E_e}{m_\mu}$  is called the reduced energy, while  $E_e$ ,  $m_\mu$  and  $m_e$  are the total energy of the decay electron, the muon mass and the electron mass, respectively.  $\rho$  and  $\eta$  are the so-called Michel parameters.  $A$  is a normalization factor. Including the first order radiative corrections of this process, the decay probability of unpolarized muons changes to (see [35] and [36])

$$\frac{dN}{dx}(x; \rho) = A \left[ 3(1-x) + 2\rho\left(\frac{4}{3}x - 1\right) + 3\eta \left(\frac{m_e}{m_\mu}\right) \frac{1-x}{x} + \frac{\alpha}{4\pi} f(x) \right] x^2, \quad (9.2)$$

where  $\alpha$  is the fine structure constant and  $f(x)$  is given by

$$\begin{aligned} f(x) &= (6 - 4x)R(x) + (6 - 6x)\ln x \\ &+ \frac{1-x}{3x^2} ((5 + 17x - 34x^2)(\omega + \ln x) - 22x + 34x^2), \end{aligned} \quad (9.3)$$

with  $\omega = \ln(m_\mu/m_e)$  and  $R(x)$  given by

$$\begin{aligned} R(x) &= 2L_2(x) - \frac{1}{3}\pi^2 - 2 + \omega \left[ \frac{3}{2} + 2\ln\left(\frac{1-x}{x}\right) \right] \\ &\quad - \ln x(2\ln x - 1) + \left( 3\ln x - 1 - \frac{1}{x} \right) \ln(1-x). \end{aligned} \quad (9.4)$$

$L_2(x)$  is the Euler's dilogarithm

$$L_2(x) = - \int_0^x \frac{\ln(1-t)}{t} dt = \sum_{\nu=1}^{\infty} \frac{x^\nu}{\nu^2}. \quad (9.5)$$



## 9.2 Data and Monte Carlo Samples

The data sample used for this analysis is the same as the one used to calibrate the detector (see section 8.1), i.e. data taken at the end of 2007, with one exception. In this analysis the cuts on the minimal charge and the maximal cathode sum radius were not applied (see table 8.2) because they reduce the hit reconstruction efficiency.

The Monte Carlo (MC) sample was produced by setting one Michel event at time equal 0 to simulate the triggered event. To simulate the background from other Michel decays, randomly placed Michel events have been added, corresponding to the beam intensity of  $5 \cdot 10^6$  muons per second. All known detector efficiencies have been included. Namely, inefficiencies due to the missing channels, hit reconstruction inefficiencies and inefficiencies due to differences between the real and the MC geometry. The missing channels could be incorporated exactly, whereas for the hit inefficiencies and the discrepancy in the geometry certain assumptions have been made (see also chapter 9.4.2). In the following we will present two kind of MC energy spectra. One is the so called "reconstructed" spectrum. This was produced by applying the full reconstruction chain to the MC data. Therefore, this should match the data spectrum. The other is the "raw" spectrum. This was produced by also applying the full reconstruction chain as in the "reconstructed" spectrum but then the reconstructed energy measurement was replaced by the simulated energy. Therefore, this spectrum will include all efficiencies, especially the track reconstruction efficiencies, but showing the precise simulated energy. Thus, having a sharp Michel edge.

### 9.3 Determination of the Energy Resolution

The energy resolution of the drift chambers is measured by fitting the energy spectrum of the data to the "raw" MC spectrum  $f_{MC}$  convoluted with a gaussian function.

$$f(x) = f_{MC}(x) * N \cdot e^{-\frac{(x-x_0)^2}{2\sigma^2}}. \quad (9.6)$$

The width of the gaussian function  $\sigma$  is equal to the energy resolution of the detector. The fit was applied in the region between 50 to 54 MeV and is shown as blue dashed line in the lower panel of figure 9.1. The energy resolution was determined to be

$$\sigma_E = 0.444 \pm 0.007 \pm 0.05 \text{ MeV}, \quad (9.7)$$

where the first quoted error is of statistic origin whereas the second error is caused by systematic uncertainties. The  $\chi^2/ndf$  is 11.73. For a discussion of the systematical error we refer to section 9.4.2.

In an alternative approach one can fit the data spectrum with a convolution of the full Michel spectrum (see figure 9.3) and a gaussian function. The fit is applied in the region of 50 to 54 MeV and shown in figure 9.2. This method leads to an energy resolution of

$$\sigma'_E = 0.548 \pm 0.006, \quad (9.8)$$

where the quoted error is of statistic origin. The  $\chi^2/ndf$  of the fit is 2.67. However, the drift chambers not only have a limited acceptance for low energy particles but also for high energy particles. This is due to the fact, that particles with energies above 50 MeV can leave the sensitive area of the drift chambers at the largest radius and either scatter in the chamber frame or be rejected by the reconstruction algorithm. Therefore, we don't expect a perfect agreement at the Michel edge between the data spectrum and the full Michel spectrum convoluted with a gaussian function.

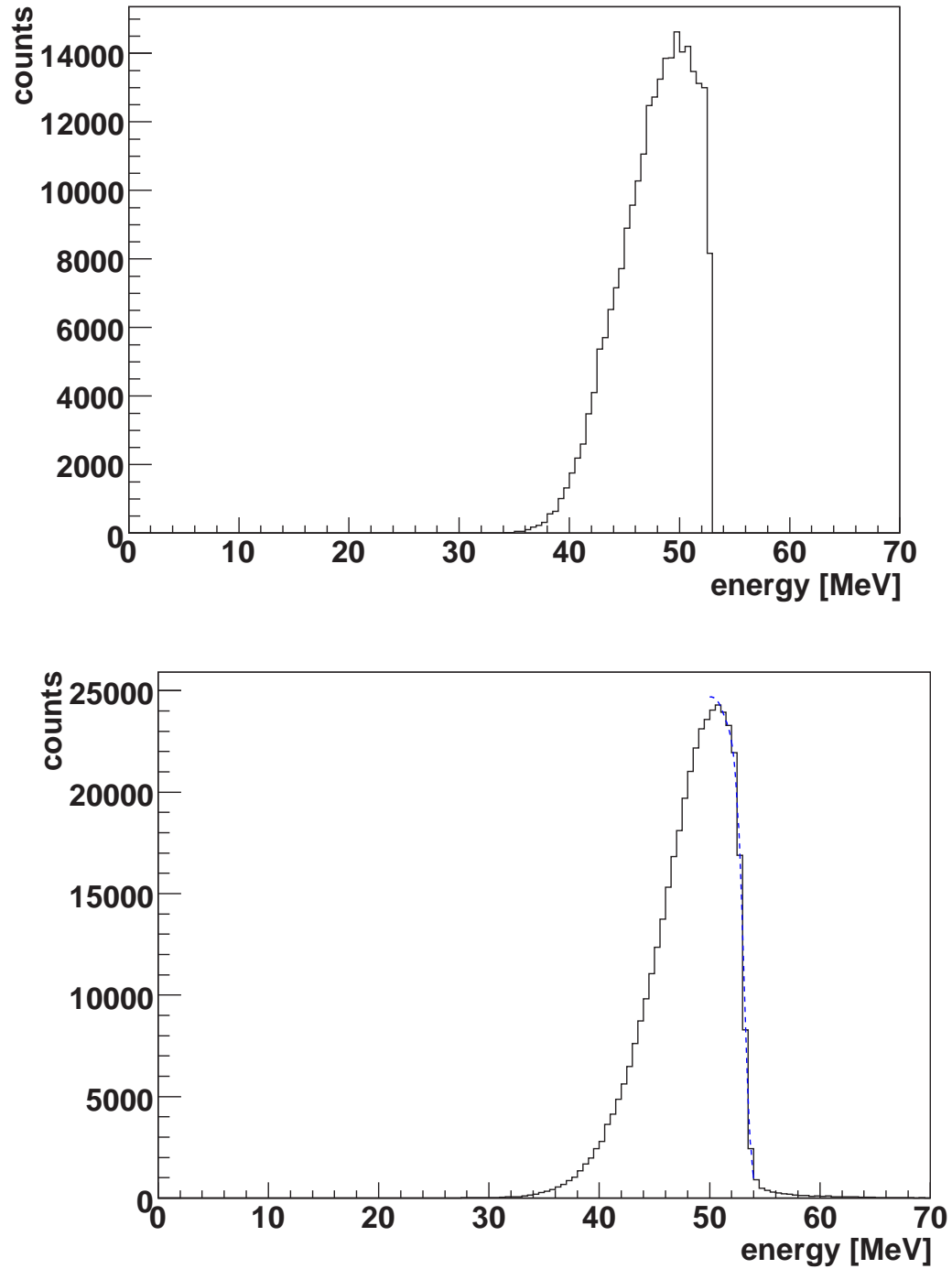


Figure 9.1: The upper plot shows the "raw" MC energy spectrum, while the lower plot shows the data energy spectrum as a histogram and the fitted MC spectrum as a dashed line.

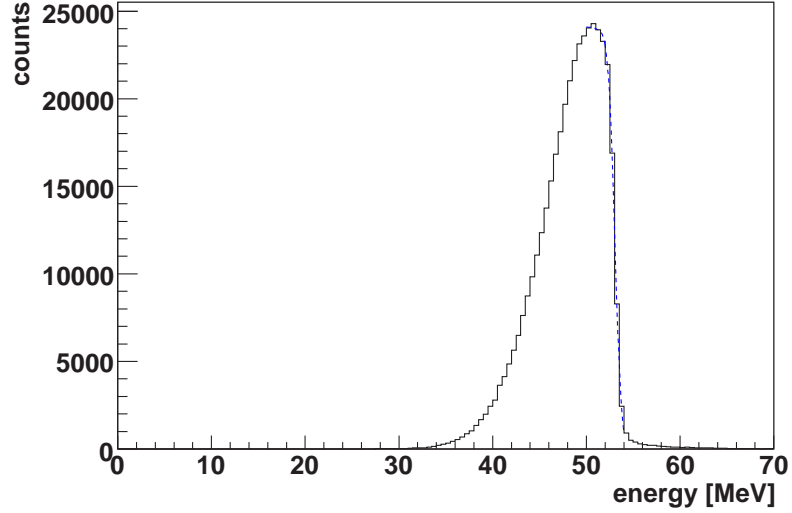


Figure 9.2: The data Michel spectrum (solid line) fitted with the full Michel spectrum (see figure 9.3) convoluted with a gaussian function (dashed line) in the range of 50-54 MeV.

## 9.4 Determination of the Michel Parameters

The Michel parameters  $\rho$  and  $\eta$  are bilinear combinations of the complex constants describing the couplings in the muon decay. In the Standard Model (SM), these parameters are well defined and take the values

$$\begin{aligned}\rho_{SM} &= 0.75 \\ \eta_{SM} &= 0.\end{aligned}\tag{9.9}$$

Therefore, by measuring the Michel parameters one can verify the SM. Figure 9.3 (left) shows the energy spectra of the muon decay for selected values of the Michel parameters. It can be seen from the picture that the energy spectrum depends much more on  $\rho$  than on  $\eta$ . In figure 9.3 the line for  $\rho=0.75, \eta=0$  and  $\rho=0.75, \eta=1$  are hardly distinguishable. The minor importance of  $\eta$  can be explained by the suppression factor  $m_e/m_\mu$  in equation 9.2. The radiative corrections influence the spectrum near the maximum energy (see figure 9.3 on the right side). There is a substantial effect on  $\rho$  coming from the radiative corrections, which have been shown to be of the order of 6% [36].

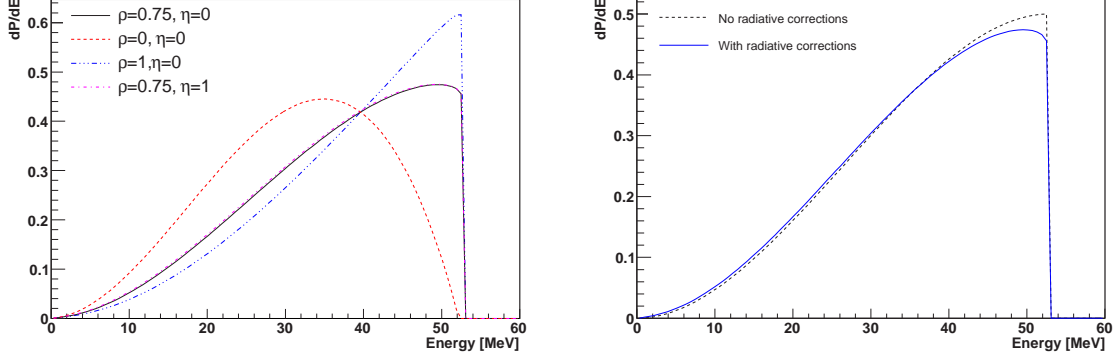


Figure 9.3: Left: Variation of energy spectra for various values of the Michel parameters. Right: Effect of the first order radiative corrections on the energy spectrum.

### 9.4.1 Results

To extract the Michel parameters we fit the weighted MC energy spectrum to the data spectrum. The weighting function accounts for the variation of the Michel parameters and is defined as

$$\omega = \frac{\frac{dN}{dx}(x_{MC}; \rho, \eta)}{\frac{dN}{dx}(x_{MC}; \rho_{SM}, \eta_{SM})}, \quad (9.10)$$

where  $dN/dx$  was defined in section 9.1 and  $x_{MC} = E_{MC}/E_{max}$ , and  $E_{MC}$  is the MC generated energy. Therefore, we correct the height of every energy bin in the MC energy histogram with the weighting function. The fit is performed by a  $\chi^2$  minimization and we obtain for the unconstrained fit

$$\begin{aligned} \rho &= 1.002 \pm 0.009 \\ \eta &= 108.2 \pm 2.8 \end{aligned} \quad (9.11)$$

where the quoted errors are of statistical origin. The accuracy in the determination of  $\eta$  is very low, since this parameter is weighted by  $m_e/E_{max}$  in the decay probability (see equation 9.2). Furthermore, in the high energy region of the Michel spectrum there is a strong correlation between  $\rho$  and  $\eta$ . Therefore, a large change in  $\eta$  can be compensated with a small variation of  $\rho$ . To obtain a more accurate measurement of the  $\rho$  parameter, we fix  $\eta$  to the Standard Model value. The single  $\rho$  parameter fit yields:

$$\rho = 0.731 \pm 0.004 \pm 0.120, \quad (9.12)$$

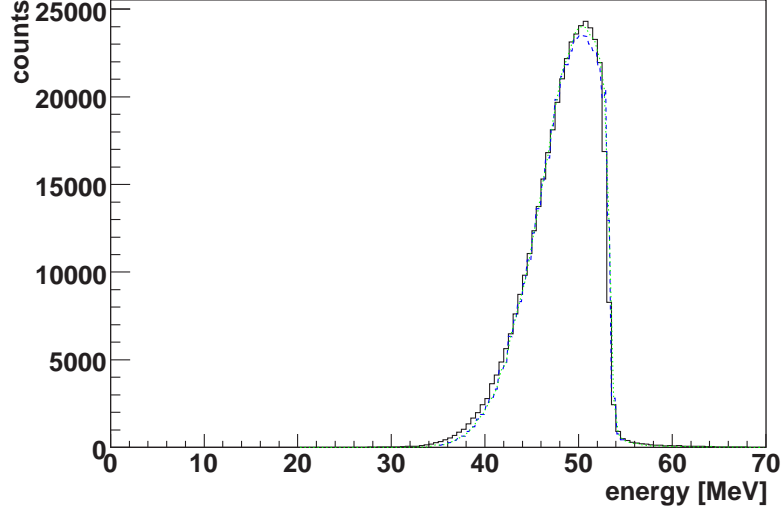


Figure 9.4: The solid black lines represent the data energy spectrum, while the dashed blue (dotted green) line represent the fitted (SM) MC spectrum.

where the first quoted error is of statistical origin (see figure 9.4) and the second quoted error is of systematic origin. Due to the large number of reconstructed events ( $\sim 1$  million), the statistical error is very small. The main source of error is of systematic origin, as discussed below.

### 9.4.2 Systematical Error

Several steps during the MC simulation and reconstruction are possible sources for systematical errors. The main uncertainties are located in the estimation of the inefficiencies in the hit reconstruction for data events on the innermost wire. During the 2007 run we recorded twice as much hits on the innermost wire of both planes of a chamber than we expected. The additional hits contain a very low amount of charge. This behavior is not yet understood but we realized that the simulation of the drift electrons on this cells in the MC is not correct. However, because of lack of manpower, the MC could not be changed for the analysis presented in this thesis. An other potential source for a systematical error lies in a mismatch between the detector geometry used in the simulation and the real detector geometry.

To estimate the systematical error for both the energy resolution and the measurement of the  $\rho$  parameter several MC data sets were created with changes in the drift chamber geometry in the order of 1 mm and different implementations of the hit efficiency. The hit efficiency on the innermost wire was changed by up to 50 % and the overall hit efficiency was changed in the order of 10 %. The energy resolution and the

$\rho$  parameter were determined with all of these MC data sets. Out of the variation of these measurements the systematical error was calculated.

The systematical error for the measurement of the energy resolution was found to be in the order of 40 % resulting in an error of

$$\sigma_{E_{syst}} = 0.05 \text{ MeV} \quad (9.13)$$

and 16 % for the measurement of the  $\rho$  parameter resulting in an error of

$$\sigma_{\rho_{syst}} = 0.12. \quad (9.14)$$

This errors will be decreased by further analysis of the detector, which will improve the understanding of the detector behavior. Furthermore, solving the problems related to the innermost wires will limit the inefficiencies in the hit reconstruction and will, therefore, simplify the analysis. However, with this detector only the very high energy part of the Michel spectrum can be measured. In this region the spectrum is not very sensitive to the  $\rho$  parameter. Therefore, large changes in  $\rho$  cause only small changes in the spectrum. This leads to the assumption that with these drift chambers a competitive measurement of the Michel parameters will be impossible.

### 9.4.3 Comparison with existing measurements

The  $\rho$  parameter has been measured in several experiments in the past (see table 9.1). A group of experiments [37], [38], [39] and [40] have measured the  $\rho$  parameter in a muon decay using magnetized spark chambers. They fitted the high energy part of the Michel spectrum. In this part of the spectrum  $\rho$  and  $\eta$  are highly correlated, therefore all these analysis were done with an assumption of a SM value for  $\eta$  ( $\eta = 0$ ). Other experiments [41] used a liquid hydrogen bubble chamber to measure the low energy part of the spectrum in a muon decay. They made a two-parameter fit, incorporating the results from the previously mentioned papers. This way they obtained the most accurate existing measurement with no assumptions on the value of  $\eta$ . The  $\rho$  parameter has also been measured by analyzing data from  $\tau$  decays in electron-positron colliders [42], [43], [44], [45], [46] and [47]. Recently, [48] has measured the  $\rho$  parameter in a muon decay using drift chambers. The results from all of the mentioned experiments are listed in table 9.1 and figure 9.5.

Author	$\rho$	Assumption	Year	Ref.
Peoples	$0.750 \pm 0.003$	$\eta \equiv 0$	1966	[37], [38]
Sherwood	$0.760 \pm 0.009$	$\eta \equiv 0$	1967	[39]
Fryberger	$0.762 \pm 0.008$	$\eta \equiv 0$	1968	[40]
Derenzo	$0.752 \pm 0.003$	$-0.13 < \eta < 0.07$	1969	[41]
SLD	$0.720 \pm 0.09 \pm 0.03$	lepton univers.	1997	[42]
CLEO	$0.747 \pm 0.01 \pm 0.006$	lepton univers.	1997	[43]
ARGUS	$0.731 \pm 0.031$	lepton univers.	1998	[44]
OPAL	$0.780 \pm 0.03 \pm 0.02$	lepton univers.	1999	[45]
DELPHI	$0.780 \pm 0.02 \pm 0.02$	lepton univers.	2000	[46]
ALEPH	$0.742 \pm 0.016$	lepton univers.	2001	[47]
TWIST	$0.750 \pm 0.001 \pm 0.001$	$\eta \equiv -0.007$	2004	[48]

Table 9.1: Results from the previous measurements of the Michel  $\rho$  parameter, including statistical and systematical errors. Single error bounds correspond to quadratically added statistical and systematical errors.

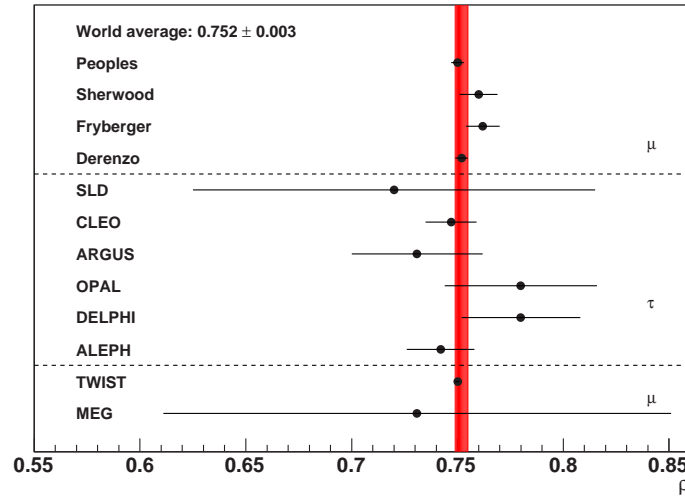


Figure 9.5: Comparison of the existing measurements of  $\rho$ . The measurements are grouped in  $\mu$  decay measurements,  $\tau$  decay measurements and the measurement presented in this work.

## 9.5 Outlook

This work presents the first analysis of the data taken with the drift chambers of the MEG experiment. The analysis will be continuously improved in the future. A significant improvement of the measured  $z$  and energy resolutions will be achieved with



the replacement of the DRS2 with the DRS4 chip, in the summer of 2008.

Studies of matching the tracks measured in the drift chambers with hits reconstructed in the timing counters are ongoing. Furthermore, studies of matching the positron tracks with gamma racks are also under way. During the runs in 2008 the first data with a  $\mu^+ \rightarrow e^+ \gamma$  trigger will be taken. The experiment is expected to run until 2010.



# Chapter 10

## Conclusions

In this thesis, performed in the framework of the MEG experiment, the calibration of the the DRS chip, the development of an analysis framework and the analysis of the drift chamber data are presented.

This DRS chip is a key part of the MEG experiment, since it is used to read out all detectors. The chip was used in the 2006 and the 2007 R&D runs of the experiment and thus used to collect all the data analyzed in this work. The calibration algorithms needed to obtain a good performance of the chip was described. The different deficiencies found during the testing phase of the version of the chip used during the engineering run, were pointed out. Furthermore, the performance of the chip was measured.

In the context of this work a new analysis framework generator, called ROME was developed. This software is the base of all the online and the offline analysis software of the experiment. A short introduction into the analysis framework generator was given. This software uses a new approach of making frameworks more universal. We pointed out all the benefits of such an approach.

The main part of this thesis is the analysis of the drift chambers. We presented the results of the first engineering run in 2006 and pointed out all the hardware problems we experienced at that time. A step by step documentation of the analysis algorithms including the hit reconstruction and the track reconstruction was given. The quality of these algorithms was tested with Monte Carlo data. The momentum resolution of signal tracks was found to be

$$\sigma_E = 0.27 \pm 0.01 \text{ (stat) MeV.} \quad (10.1)$$

In the 2007 run we could collect enough useful data to investigate the energy resolution of the drift chambers. The analysis of the energy spectrum is dominated by errors of systematic origin. The measurement yield a resolution of

$$\sigma_E = 0.444 \pm 0.007 \pm 0.05 \text{ MeV,} \quad (10.2)$$

which is almost two times worse than the MC momentum resolution given in equation 10.1. The data momentum resolution is expected to improve with upgrades of the hardware and improvements in the calibration and analysis algorithms.

In addition, the Michel parameters were measured. This measurement is even more dominated by systematical errors as the one of the energy resolution. The result obtained for the  $\rho$  parameter was

$$\rho = 0.731 \pm 0.004 \pm 0.120. \tag{10.3}$$

in good agreement with the best measured value of  $\rho = 0.750 \pm 0.001 \pm 0.001$  obtained by the TWIST experiment.

# Appendix A

## Calculation of the Z Projection during the Track Finding

When a track candidate consist of more than two clusters, the addition of another cluster can be constrained by calculating the projection in z to this new cluster. This helps to reduce the possible number of cluster candidates which have to be checked. The projection is done using three clusters and performing the following steps.

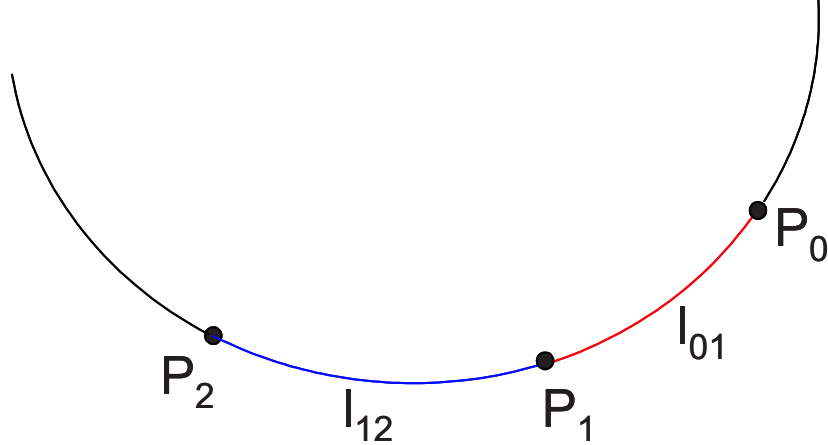


Figure A.1: Illustration of the variables used in the z projection calculation.

- Calculate a circle in the xy-plane through the three clusters ( $P_0$ ,  $P_1$  and  $P_2$  in figure A.1),
- Extract the arc length  $l_{01}$  of the circle and the z difference  $\Delta z_{01}$  between the first and the second point.

- Extract the arc length  $l_{12}$  of the circle and the  $z$  difference  $\Delta z_{12}$  between the second and the third point.
- Calculate the projected  $z$  value of the third cluster

$$z_{proj} = z_1 + \Delta z_{01} \cdot \frac{l_{12}}{l_{01}} \quad (\text{A.1})$$

# List of Figures

1.1	Feynman diagram for the $\mu^+ \rightarrow e^+\gamma$ decay with neutrino oscillation . .	14
1.2	Feynman diagram for the $\mu^+ \rightarrow e^+\gamma$ decay in SU(5) SUSY GUT . . . .	19
2.1	Feynman diagrams in SO(10) SUSY GUT . . . . .	21
2.2	Predictions of $\mu^+ \rightarrow e^+\gamma$ branching ratio in SU(5) SUSY models . . . .	22
2.3	MSW Solutions . . . . .	23
2.4	Improvement of the 90% CL upper limit on the $\mu^+ \rightarrow e^+\gamma$ decay branching fraction over the years . . . . .	24
2.5	Feynman diagram of the $\mu^+ \rightarrow e^+\gamma$ signal and background events . . .	25
2.6	A schematic view of the TRIUMF $\mu^+ \rightarrow e^+\gamma$ experiment and the Crystal Box detector . . . . .	26
3.1	Pion and muon flux in $\pi$ E5 . . . . .	32
3.2	MEG specific beam line components . . . . .	33
3.3	The MEG Detector . . . . .	35
3.4	Advantages of a gradient magnetic field: fast sweep out. . . . .	36
3.5	Advantages of a gradient magnetic field: bending radius is independent of the emission angle. . . . .	37
3.6	Drift Chambers and Frame . . . . .	38
3.7	Drift Chambers Cell Configuration . . . . .	39
3.8	Drift Chambers Anode Frame . . . . .	39
3.9	Drift Chamber Readout . . . . .	40
3.10	The timing counter configuration . . . . .	41
3.11	The liquid xenon detector . . . . .	42
4.1	Domino Ring Sampler Scheme . . . . .	46
4.2	Temperature Effect on the Response Function . . . . .	48
4.3	Schematic view of the DRS2 domino cell . . . . .	49
4.4	Schematic view of the DRS3 domino cell . . . . .	49
4.5	DRS fake pulse . . . . .	50
4.6	Schematic view of the DRS3 domino cell . . . . .	52

4.7	Integral deviation of the domino speed . . . . .	53
4.8	Cell to cell deviation of the domino speed . . . . .	54
4.9	Time calibration . . . . .	54
4.10	Clock Signal . . . . .	55
4.11	Crosstalk from the Domino Tap Signal . . . . .	56
4.12	Cluster Points in the voltage response . . . . .	57
4.13	Signal of X-Talk Measurement . . . . .	57
4.14	1. Neighbor Signal of X-Talk Measurement . . . . .	58
4.15	Ghost Pulses . . . . .	59
4.16	Bandwidth of the DRS2 chip . . . . .	60
4.17	Pulse Generator Signal . . . . .	60
4.18	Pulse Generator Signal with Template Fit . . . . .	61
4.19	Setup for time- and charge resolution measurements . . . . .	62
5.1	The translation process . . . . .	69
6.1	Fast oscillation baseline variation in first engineering run data . . . . .	77
6.2	Slow oscillation baseline variation in first engineering run data . . . . .	78
6.3	Number of Hits per Wire . . . . .	79
7.1	Sample Waveform . . . . .	82
7.2	Anode Noise Subtraction . . . . .	83
7.3	Calculation of the Drift Time . . . . .	87
7.4	Sample Event . . . . .	88
7.5	MC momentum resolution . . . . .	89
7.6	MC angular resolution. . . . .	90
7.7	MC production vertex resolution. . . . .	90
7.8	Percentage of MC hits not found . . . . .	91
8.1	Alpha vs. Anode Asymmetry . . . . .	95
8.2	Anode Gain Spread . . . . .	96
8.3	Cathode Charge vs. Alpha . . . . .	97
8.4	Cathode Gain Spread . . . . .	97
8.5	Layout of the Cosmic Ray Counter Installation . . . . .	98
8.6	Peak time distribution . . . . .	99
8.7	Sample histogram of a $\Delta R$ distribution . . . . .	100
8.8	Miss alignment in R and Z direction. . . . .	101
8.9	X-T relation checks. . . . .	101
8.10	Lorentz angle . . . . .	102
8.11	Anode Z resolution. . . . .	103
8.12	Z and R resolution. . . . .	104



---

9.1	The upper plot shows the "raw" MC energy spectrum, while the lower plot shows the data energy spectrum as a histogram and the fitted MC spectrum as a dashed line. . . . .	109
9.2	The data Michel spectrum (solid line) fitted with the full Michel spectrum (see figure 9.3) convoluted with a gaussian function (dashed line) in the range of 50-54 MeV. . . . .	110
9.3	Left: Variation of energy spectra for various values of the Michel parameters. Right: Effect of the first order radiative corrections on the energy spectrum. . . . .	111
9.4	The solid black lines represent the data energy spectrum, while the dashed blue (dotted green) line represent the fitted (SM) MC spectrum. . . . .	112
9.5	$\rho$ parameter measurements overview . . . . .	114
A.1	Z Projection in Track Finder . . . . .	119

# List of Tables

2.1	Historical Progress of search for $\mu^+ \rightarrow e^+ \gamma$ since the era of meson factories with 90% C.L. upper limits. . . . .	25
3.1	Main properties of the $\pi$ E5 beam line . . . . .	33
3.2	Target property comparison . . . . .	34
3.3	Parameters of the COBRA magnet. . . . .	37
4.1	Response Calibration Error . . . . .	52
4.2	X-Talk on the DRS2 boards . . . . .	58
4.3	Linear Fit vs. Template Fit . . . . .	61
4.4	Time resolution of the DRS2 . . . . .	62
4.5	Charge resolution of the DRS2 . . . . .	63
6.1	High Voltage applied to the DC in the first engineering run . . . . .	76
8.1	HV summary . . . . .	94
8.2	Cuts for calibration . . . . .	94
9.1	$\rho$ parameter measurements . . . . .	114

# Bibliography

- [1] R. N. Mohapatra, Berlin, Germany: Springer ( 1986) 309 P. ( Contemporary Physics).
- [2] T. Morii, C. S. Lim, and S. N. Mukherjee, River Edge, USA: World Scientific (2004) 298 p.
- [3] I. J. R. Aitchison, Prepared for European School on High-Energy Physics, Tsakhkadzor, Armenia, 24 Aug - 6 Sep 2003.
- [4] Y. Kuno and Y. Okada, Rev. Mod. Phys. **73**, 151 (2001), hep-ph/9909265.
- [5] UA1, G. Arnison *et al.*, Phys. Lett. **B126**, 398 (1983).
- [6] UA2, P. Bagnaia *et al.*, Phys. Lett. **B129**, 130 (1983).
- [7] CDF, P. Sinervo, Proceedings of the 14th International Symposium on Lepton and Photon Interaction, Stanford (1989).
- [8] L3, B. Adeva *et al.*, Phys. Lett. **B231**, 509 (1989).
- [9] ALEPH, D. Decamp *et al.*, Phys. Lett. **B231**, 519 (1989).
- [10] OPAL, M. Z. Akrawy *et al.*, Phys. Lett. **B231**, 530 (1989).
- [11] Delphi, P. A. Aarnio *et al.*, Phys. Lett. **B231**, 539 (1989).
- [12] G. S. Abrams *et al.*, Phys. Rev. Lett. **63**, 724 (1989).
- [13] SNO, Q. R. Ahmad *et al.*, Phys. Rev. Lett. **87**, 071301 (2001), nucl-ex/0106015.
- [14] SNO, Q. R. Ahmad *et al.*, Phys. Rev. Lett. **89**, 011301 (2002), nucl-ex/0204008.
- [15] SNO, Q. R. Ahmad *et al.*, Phys. Rev. Lett. **89**, 011302 (2002), nucl-ex/0204009.
- [16] LEP Higgs Working Group, (2001), hep-ex/0107030.
- [17] G. Signorelli, Ph.D. Thesis (2004).

- [18] E. P. Hincks and B. Pontecorvo, Can. J. Res. **28A**, 29 (1950).
- [19] P. Kunze, Z. Phys. **83**, 1 (1933).
- [20] P. Depommier *et al.*, Phys. Rev. Lett. **39**, 1113 (1977).
- [21] A. van der Schaaf *et al.*, Nucl. Phys. **A340**, 249 (1980).
- [22] W. W. Kinnison *et al.*, Phys. Rev. **D25**, 2846 (1982).
- [23] R. D. Bolton *et al.*, Phys. Rev. **D38**, 2077 (1988).
- [24] R. D. Bolton *et al.*, Phys. Rev. Lett. **56**, 2461 (1986).
- [25] MEGA, M. L. Brooks *et al.*, Phys. Rev. Lett. **83**, 1521 (1999), hep-ex/9905013.
- [26] H. W. Reist *et al.*, Nucl. Instrum. Meth. **153**, 61 (1978).
- [27] MEG Collaboration, A. B. et al., PSI Annual Report (2003).
- [28] MEG Collaboration, H. Nishiguchi and S. Mihara, MEG-TN013, <http://meg.web.psi.ch/docs/tnote/tn013/tn013.html> (2001).
- [29] S. Ritt, <http://midas.psi.ch>.
- [30] S. Ritt, Nucl.Instrum.Meth.A518:470-471 (2004).
- [31] R. Brun and F. Rademakers, Proceedings AIHENP'96 Workshop, Lausanne, Sep. 1996, Nucl. Inst. & Meth. in Phys. Res. A 389 (1997) 81-86. See also <http://root.cern.ch/>.
- [32] R. E. Kalman, Trans. ASME J. Basic Eng. **82**, 35 (1960).
- [33] L. Michel, Proc. Phys. Soc. **A63**, 514 (1950).
- [34] T. Kinoshita and A. Sirlin, Phys. Rev. **107**, 593 (1957).
- [35] C. Bouchiat and L. Michel, Phys. Rev. **106**, 170 (1957).
- [36] T. Kinoshita and A. Sirlin, Phys. Rev. **113**, 1652 (1959).
- [37] M. Bardon, P. Norton, J. Peoples, A. M. Sachs, and J. Lee-Franzini, Phys. Rev. Lett. **14**, 449 (1965).
- [38] J. Peoples, Columbia University Report No. NEVIS-147 (1966 (Unpublished)).
- [39] B. A. Sherwood, Phys. Rev. **156**, 1475 (1967).

- 
- [40] D. Fryberger, Phys. Rev. **166**, 1379 (1968).
  - [41] S. E. Derenzo, Phys. Rev. **181**, 1854 (1969).
  - [42] K. Abe *et al.*, Phys. Rev. Lett. **78**, 4691 (1997).
  - [43] J. P. Alexander *et al.*, Phys. Rev. D **56**, 5320 (1997).
  - [44] ARGUS, H. Albrecht *et al.*, Phys. Lett. **B431**, 179 (1998), hep-ex/9711022.
  - [45] OPAL, K. Ackerstaff *et al.*, Eur. Phys. J. **C8**, 3 (1999), hep-ex/9808016.
  - [46] DELPHI, P. Abreu *et al.*, Eur. Phys. J. **C16**, 229 (2000), hep-ex/0107076.
  - [47] ALEPH, A. Heister *et al.*, Eur. Phys. J. **C22**, 217 (2001).
  - [48] TWIST Collaboration, J. R. Musser *et al.*, Physical Review Letters **94**, 101805 (2005).



# Acknowledgements

My gratitude goes in first place to Professor R. Eichler who gave me the opportunity to work in this exciting project.

I would also like to thank Professor F. Pauss who was willing to be the co-examiner of this thesis.

I'm especially grateful for the support and the guidance of Dr. S. Ritt. His advises were fundamental for all aspects of the presented work.

Everything I know about drift chambers, I learned from Dr. J. Egger. I am thankful for all his advises and the discussions with him. I am also grateful for the help of H. Nishiguchi and Dr. M. Hildebrandt, who not only helped me analyzing the drift chamber data but also accompanied me during shifts. A. Hofer and D. Fahrni readily answered all my questions about the chamber hardware.

The software framework was developed together with R. Sawada and Dr. S. Yamada. Without them this project would not have reached its current quality.

I enjoyed being part of the MEG collaboration and I am thankful to all members of this collaboration.

I am endlessly thankful to my love Sabrina, who was supporting me during these years. Although, she was writing a PhD thesis herself she was raising our two loving kids Ambra and Nuria.





## CURRICULUM VITAE

### Matthias Schneeбели

Date and place of birth    9th of August 1976 in Zürich, ZH  
Nationality                      Swiss  
Address                         Schumacherweg 27, 8046 Zürich

### Education

1/2004 – 12/2007    PhD thesis in Particle Physics at the Institute for Particle Physics, ETH Zürich,  
under supervision of Prof. Dr. R. Eichler and Dr. S. Ritt about  
*The drift chambers of the MEG experiment and measurement of the  $\rho$ -parameter in the Michel spectrum of the muon decay*  
5/2003 – 9/2003    Dipl. Phys. ETH  
Diploma thesis at the Institute for Particle Physics, ETH Zürich  
under supervision of Prof. Dr. R. Eichler and Dr. C. Grab about  
*Studies of Vertex Tagging in Charm and Beauty Production*  
Specifications: Particle Physics, Quantum Field Theory,  
Physics beyond the Standard Model  
1/1996                 Schweizerische Eidgenössische Matura, Typus C  
(mathematical scientific field)  
8/1991 – 1/1996    Kantonsschule Limmattal, Urdorf

### Professional Experience

1/2004 – 12/2007    Scientific assistant at the Institute for Particle Physics,  
ETH Zürich  
1999      – 2007      Co-founder of the software and robot technology company  
SoftART Zürich AG